RADIATION MECHANISMS OF VHE γ - RAY SOURCES

A THESIS

SUBMITTED FOR THE DEGREE OF

DOCTOR OF PHILOSOPHY

DEPARTMENT OF PHYSICS,
SCHOOL OF PHYSICAL, CHEMICAL & APPLIED SCIENCES
PONDICHERRY UNIVERSITY,
PONDICHERRY - 605 014, INDIA

BY

AMIT SHUKLA

INDIAN INSTITUTE OF ASTROPHYSICS
2ND BLOCK, KORAMANGALA
BANGALORE - 560 034, INDIA

2013

TO

MY FAMILY AND FRIENDS ...

"It is a capital mistake to theorize before one has data."

– Sherlock Holmes

DECLARATION

I hereby declare that the material presented in this thesis is the result of investigations carried out by me, at Indian Institute of Astrophysics, Bangalore under the supervision of Prof. G. C. Anupama. The results reported in this thesis are new, and original, to the best of my knowledge, and have not been submitted in whole or part for a degree in any University. In keeping with the general practice of reporting scientific observations, due acknowledgement has been made whenever the work described is based on the findings of other investigators.

Place : Bangalore **(Amit Shukla)**
Date :

CERTIFICATE

This is to certify that the work embodied in this thesis entitled **"Radiation Mechanisms of VHE γ - Ray Sources"**, has been carried out by Mr. Amit Shukla, under my supervision and the same has not been submitted in whole or part for Degree, Diploma, Associateship Fellowship or other similar title to any University.

Place : Bangalore
Date :

(G. C. Anupama)
Professor
Indian Institute of Astrophysics,
Bangalore

ACKNOWLEDGEMENT

Completion of this doctoral dissertation was possible with the support of several people. I would like to express my sincere gratitude to all of them. First of all, I am extremely grateful to my research supervisors, Prof. G.C. Anupama and Prof. Tushar P. Prabhu, for their valuable guidance, scholarly inputs and consistent encouragement I received throughout the research work. This feat was possible only because of the unconditional support provided by them.

I am very thankful to Director, IIA for giving me an opportunity to work at IIA and providing me with infrastructure to work and taking keen interest in the project.

I owe my deepest gratitude to Dr. Varsha R. Chitnis, for her valuable guidance throughout this work. The thesis would not have come to a successful completion, without her support and encouragement.

My sincere thanks to Prof. P. R. Viswanath for teaching the basics of γ-ray astronomy and providing support and encouragement. I wish to thank Dr. Prasad Subramanian for his constant support and guidance regarding theoretical aspects of blazars.

My thanks are due to Prof. B. S. Acharya and Prof. P. Bhattacharjee for their valuable suggestions and comments on HAGAR analysis to improve the technique. I would also like to thank all the members of HAGAR collaboration.

I also take this opportunity to express a deep sense of gratitude to Prof. Karl Mannheim and Prof. Razmik Mirzoyan for providing support to visit their group at Germany to learn about γ-ray astronomy and Prof. Peter A. Becker for his valuable suggestions regarding blazar modeling.

I am obliged to staff members of Computer Center, library and administration of IIA. I am grateful for their support during the period of my thesis. This work might have not reached the end, without their help.

I wish to thank Prof. A. N. Ramprakash for introducing me to the field of astrophysics and providing support and encouragement since my M.Sc days.

I wish to take this occasion pay my sincere regards to all my teachers from whom I have borrowed the building blocks of my knowledge, especially to Mr. Rajesh Mishra and Mr. Servesh Bajpai, from whom I learnt the basics of Physics and Maths.

I sincerely acknowledge the Time Allocation Committee of HCT and HAGAR

telescopes for their generous time allocation.

I like to thank Prof G. Govindraj and Dr. A. Mangalam for their suggestions and comments as the members of my doctoral committee. I thank Prof. G. Chandrasekaran, Head of the Department of Physics, Pondicherry University and to Dr. Latha K. for her support and guidance in administrative procedures.

My very sincere thanks to Dipu da, Dr. Arun Mangalam, Prof. Bhanu Das, Dr. Annapurni Subramaniam, Dr. D. K. Shau, Dr. C. S. Stalin, Dr. G. Pandey, Dr. Pravabati for teaching physics and taking part in the discussions on several topics of physics and astrophysics.

I will always cherish the memories of long association with Kittu, Sam (BABA ji), Radio Jayashree, ACP (Ananta), Rinki, Girju, Chandu, Sajju, Arun, Amit Bhiya, Shivani Bhabhi, Neeharika and Tanmoy, thanks for being there to listen, cheer, drink, and console.

I have been blessed with a friendly and cheerful group of fellow students at IIA, I thank them all for making my stay memorable, especially : Arya, Avijeet, Avinash, Anantha, Bharat, Blesson, Honey, Indu, Malay, Manju, Nagu, Nataraj, Pradeep, Prashanth, Rathana, Ramya, Ramya P, Sindhuja, Shubham, Sreejith, Suresh, Susmitha, Tapan, Tarun, Vaidehi, Vereesh, and Vigeesh.

My thanks are due especially to Kittu, Prashanth and Jayashree for taking pain to read the proof of my thesis and providing valuable suggestions.

I will never forget love and support of my friends Amit, Sudeep, Shalabh, Ajai, Arun, Dhawal, Shefali, Shuchi, Anuj, Gaurav, Satya, Shisu and Suyash. Thanks a lot "Sona" for being with me.

I wish to express my gratitude to my loving family for their love and encouragement throughout my life.

One of the joys of completion is to look over the journey past and remember all the friends and family who have helped and supported me along this long but fulfilling road.

Publications

Publications in Refereed Journals

1. *Observations with the High Altitude GAmma-Ray (HAGAR) telescope array in the Indian Himalayas.* **(Conference Proceeding)**
   Britto, R. J.; Acharya, B. S.; ... **Shukla, A.**; Singh, B. B.;... Vishwanath, P. R.; Yadav, K. K., **2011ASTRA...7..501B**.

2. *Multiwavelength study of TeV Blazar Mrk 421 during giant flare.*
   A. Shukla, V. R. Chitnis, P. R. Vishwanath, B. S. Acharya, G. C. Anupama, P. Bhattacharjee, R. J. Britto, T. P. Prabhu, L. Saha, B. B. Singh. **2012 A&A...541A.140S**.

3. *TeV blazar variability: the firehose instability?*
   Prasad Subramanian, **Amit Shukla**, Peter A Becker, **2012 MNRAS.423.1707S**.

4. *Pointing of HAGAR Telescope Mirrors*
   Kiran Shrikant Gothe, T. P. Prabhu, P. R. Vishwanath, B. S. Acharya, R. Srinivasan, V. R. Chitnis, P. U. Kamath, G. Srinivasulu, F. Saleem, P. M. M. Kemkar, P. K. Mahesh,F. Gabriel, J. Manoharan, N. Dorji, T. Dorjai, D. Angchuk, A. I. D'souza, S. K. Duhan, B. K. Nagesh, S. K. Rao, S. K. Sharma, B. B. Singh, P. V. Sudersanan, M. Tashi, Thsering, S. S. Upadhya, G. C. Anupama, R. J. Britto, R. Cowsik, L. Saha & **A. Shukla**. **2012ExA...tmp...44G**.

5. *Monte Carlo simulation for High Altitude Gamma Ray Telescope System at Ladakh in India*
   L. Saha, V. R. Chitnis, P. R. Vishwanath, S. Kale, **A. Shukla**, B. S. Acharya, G. C. Anupama, R. J. Britto, P. Bhattacharjee, T. P. Prabhu, & B. B. Singh. **2013APh....42...33S**.

In preparation

6. *Multiwavelength study of Mrk 501 during 2009-2011*
   A. Shukla et al. 2013. (In preparation)

7. *Multiwavelength observation of Mrk 421 during 2009-2011*
   A. Shukla et al. 2013. (In preparation)

8. *Optical and VHE gamma-ray Observation of TeV Blazars with HCT and HAGAR*
   A. Shukla et al. 2013. (In preparation)

Conference Proceedings

1. *VHE gamma-ray astronomy in India: Status of HIGRO and participation in CTA.* Britto, R. J.; Acharya, B. S.; Ahire, J. M.; Anupama, G. C.; Bhatt, N.; Bhattacharjee, P.; Bhattacharyya, S.; Chitnis, V. R.; Cowsik, R.; Dorji, N.; Duhan, S. K.; Gothe, K. S.; Kamath, P. U.; Koul, R.; Mahesh, P. K.; Majumdar, P.; Manoharan, J.; Mitra, A.; Nagesh, B. K.; Parmar, N. K.; Prabhu, T. P.; Rannot, R. C.; Rao, S. K.; Saha, L.; Saleem, F.; Saxena, A. K.; Sharma, S. K.; **Shukla, A.**; Singh, B. B.; Srinivasan, R.; Srinivasulu, G.; Sudersanan, P. V.; Tickoo, A. K.; Tsewang, D.; Upadhya, S. S.; Vishwanath, P. R.; Yadav, K. K., **2012sf2a.conf..571B**

2. *Status of the Himalayan Gamma-Ray Observatory (HIGRO) and observaton with HAGAR at very high energies.* Britto, R. J.; Acharya, B. S.; Anupama, G. C.; Bhatt, N.; Bhattacharjee, P.; Bhattacharya, S.; Chitnis, V. R.; Cowsik, R.; Dorji, N.; Duhan, S. K.; Gothe, K. S.; Kamath, P. U.; Koul, R.; Mahesh, P. K.; Manoharan, J.; Mitra, A.; Nagesh, B. K.; Parmar, N. K.; Prabhu, T. P.; Rannot, R. C.; Rao, S. K.; Saha, L.; Saleem, F.; Saxena, A. K.; Sharma, S. K.; **Shukla, A.**; Singh, B. B.; Srinivasan, R.; Srinivasulu, G.; Sudersanan, P. V.; Tickoo, A. K.; Tsewang, D.; Upadhya, S. S.; Vishwanath, P. R.; Yadav, K. K., **2011sf2a.conf..539B**

3. *Data analysis method for the search of point sources of gamma rays with the HAGAR telescope array.* Britto, R. J.; Acharya, B. S.; Anupama, G. C.; Bhattacharjee, P.; Chitnis, V. R.; Cowsik, R.; Dorji, N.; Duhan, S. K.; Gothe, K. S.; Kamath, P. U.; Mahesh, P. K.; Manoharan, J.; Nagesh, B. K.; Parmar, N. K.; Prabhu, T. P.; Rao, S. K.; Saha, L.; Saleem, F.; Saxena, A. K.; Sharma, S. K.; **Shukla, A.**; Singh, B. B.; Srinivasan, R.; Srinivasulu, G.; Sudersanan, P. V.; Tsewang, D.; Upadhya, S. S.; Vishwanath, P. R., **2011sf2a.conf..535B**

4. *Observations of Blazars using HAGAR Telescope Array.*
   A. Shukla, V. R. Chitnis, P. R. Vishwanath, B. S. Acharya, G. C. Anupama, P. Bhattacharjee, R. J. Britto, T. P. Prabhu, L. Saha, B. B. Singh,"Proceedings of ICRC 2011", **2011ICRC....8..127S** .

5. *Multiwavelength study of TeV Blazar Mrk 421 during giant flare and observations of TeV AGNs with HAGAR*
   A. Shukla, P. R. Vishwanath, G. C. Anupama, T. P. Prabhu, V. R. Chitnis, B. S. Acharya, R. J. Britto, B. B. Singh, P. Bhattacharjee, L. Saha; 2011arXiv1110.6795S (2011 Fermi Symposium proceedings - eConf C110509).

6. *Multiwavelength study of TeV Blazar Mrk 421 during giant flare*
   Amit Shukla, B. S. Acharya, G. C. Anupama, Richard J. Britto , P. Bhattacharjee, Varsha R. Chitnis, Sahana Kale, T. P. Prabhu , Lab Saha, B. B. Singh, P. R. Vishwanath, "Proceedings Astronomical Soc.of India"**2011ASInC...3R.159S** .

7. *Study of VHE gamma ray emission from AGN using HAGAR*
   Amit Shukla, B. S. Acharya, G. C. Anupama, Richard J. Britto , P. Bhattacharjee, Varsha R. Chitnis, Sahana Kale, T. P. Prabhu , Lab Saha, B. B. Singh, P. R. Vishwanath, "Proceedings Astronomical Soc.of India"**2011ASInC...3Q.159S**.

Contents

List of Figures

List of Tables

Abstract

Active galactic nuclei (AGN) are one of the most luminous objects in the universe. They are the sub-class of galaxies which emit extremely luminous emission from the nuclear regions of the galaxy. This emission is spread widely across the electromagnetic spectrum from radio wavelengths to γ-rays. This radiation from AGN is believed to be the result of accretion of matter onto the supermassive black hole of mass 10^8- 10^{10} $M_\odot$ at the center of the host galaxy. The AGN are classified by their random pointing directions to the observer in the unified scheme. AGN are mainly divided into three classes : (i) Seyfert galaxies, (ii) quasars and (iii) blazars. (i) Seyfert galaxies have modest luminosities and they are best studied since they generally lie near to us; (ii) quasars are more luminous than the host galaxy and found further away, and (iii) blazars are characterized by nonthermal emission extending from radio to high energies. The broadband radiation originates within a relativistic jet that is oriented very close to the line of sight of the observer.

The extragalactic TeV astronomy began with the detection of the nearby (z=0.031) blazar Mrk 421 above 500 GeV by the Whipple observatory [1]. Spectral energy distribution (SED) of the high energy peaked TeV blazars show two broad peaks. The first peak is located between infrared to X-ray energies and the second peak at γ-ray energies. It is believed that the first peak of the SED originates due to synchrotron radiation by relativistic electrons gyrating in the magnetic field of the jet. The origin of the high energy GeV/TeV peak is still under debate. This high energy peak might originate either due to interaction of electrons with photon field via Inverse Compton (IC) scattering as in leptonic models [2, 3, 4] or due to interaction of protons with matter, magnetic field [5, 6] or photon fields as in the hadronic models.

The existing data from multiwavelength observations are not good enough to constrain the dominant emission mechanisms in the jet that are responsible for the high energy bump. The main reason behind this is the lack of the data in the energies from 100 MeV to hundreds of GeVs. In the past few years, ground based Atmospheric Cherenkov Telescope (>100 GeV) and the space based *Fermi*-LAT

telescope (30 MeV- 300 GeV) have started providing data in this energy range.

The multiwavelength observations from radio to very high energy (VHE) γ-rays have started to provide better constraints on the AGN models [7] and also enhance our understanding about the these sources.

A multiwavelength study of Mrk 421 and Mrk 501 are presented in this thesis. The very high energy γ-ray data obtaining using HAGAR array are combined with archival data from *Fermi*-LAT, RXTE-ASM, Swift-BAT, Swift-XRT, RXTE-PCA, SPOL and OVRO for a multiwavelength study. The observed multiwavelength SED is explained by using a one zone homogeneous SSC model [8]. We have attempted to obtain SEDs for different flux states using multiwavelength data of Mrk 421 and Mrk 501. The evolution of SED during a giant flare in February 2010 from Mrk 421 is also studied in detail. This study of TeV blazars shows that the observed broadband SED is oriented by Synchrotron self Compton (SSC) mechanism. It also suggests that the electron population in the jet is accelerated by shocks which are present in the jets.

Modeling of the flux variability from Mrk 501 is also attempted to constrain the physical properties and emission mechanisms. Recently observed minute timescale variability of Mrk 501 at TeV energies has imposed severe constraints on jet models and TeV emission mechanisms. We present a viable model to explain this fast variability.

Details of HAGAR telescope array located at an altitude of 4300 m in IAO, Hanle are also presented in this thesis, with a detailed description of the instrument. In addition to the telescope system, data analysis techniques adopted to detect point sources, and the basics of atmospheric Cherenkov technique are described.

Chapter 1

γ-ray astronomy

1.1 Introduction

γ-ray astronomy is a young and relatively unexplored field compared to studies at other wavelengths. First attempts to detect γ-rays from astronomical sources were made in 1970 by the Crimen group which observed Cygnus X-3. γ-ray astronomy can be divided into two subclasses based on the energy range, (1) High Energy (HE) (30MeV-10GeV) and (2) Very High Energy (VHE) (10GeV-100TeV). The Earth's atmosphere is opaque to γ-rays, so it is necessary to use a spaceborne detector to detect γ-rays from outer space. The first γ-ray detector was flown on OSO-3 satellite in 1967. This instrument detected γ-ray emission from the Galactic center, but initial advancement in the field came only with SAS-2 in 1972 [9]. This detector made some preliminary discoveries, mapped the galactic plane and detected an isotropic γ-ray background. After three years of the launch of SAS-2, an European γ-ray satellite COS-B was launched in 1975 [10]. This experiment confirmed the SAS-2 sources and extended the γ-ray catalog upto 25 sources, including Crab, Vela pulsar [11] and 3C 279 [12], in the energy range 35 MeV to 5 GeV. The major advancement, however, came with the launch of CGRO satellite in 1991 by NASA. This satellite carried four instruments onboard: BATSE (20-1000 keV), OSSE (0.05-10MeV),

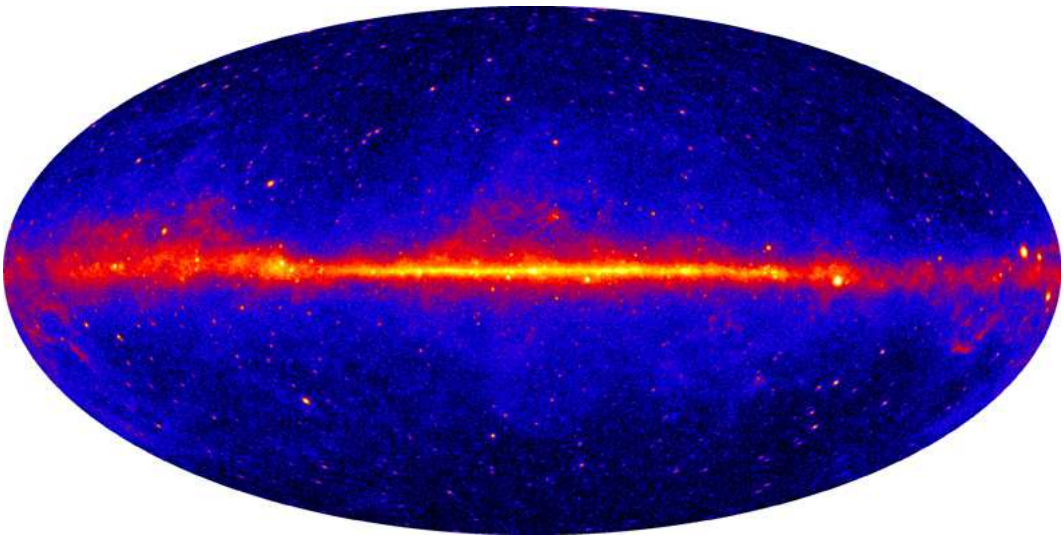

Figure 1.1: Sky map above 100 MeV produced by Fermi-LAT in the last 3 years, Figure taken from [15].

COMPTEL (0.8-30 MeV) and EGRET (20 MeV - 30 GeV)[13]. The EGRET detector was the most sensitive instrument of that time upto energies of 30 GeV, and detected 271 γ-ray sources above 100 MeV (3rd EGRET catalog) [14]. Recently, the *Fermi* Gamma-ray Space Telescope was launched in a low Earth orbit by NASA to perform γ-ray observations in the energy band of 30 MeV - 300 GeV.

Large Area Telescope (LAT) is the main instrument onboard *Fermi* satellite. This instrument revolutionized the entire field with its improved sensitivity and a wide field of view that is an added advantage over all previous missions [16]. The main goals of *Fermi*-LAT instrument are to study active galactic nuclei (AGN), pulsars, Galactic center, and search for γ-ray photons that are produced via annihilation of dark matter. LAT has already made several discoveries by now, such as the detection of Fermi-bubbles [17], and several γ-ray pulsars [18]. Till now, *Fermi*-LAT has discovered more than 1900 sources [19]. The *Fermi*-LAT all-sky map above 100 MeV is shown in Figure 1.1. *Fermi*-LAT reveals bright emission in the plane of the Milky Way (center), bright pulsars and several AGNs.

The spaceborne experiments are effective to detect γ-rays till energies of 100

GeV, but detection of VHE γ-rays become very difficult above these energies from these instruments. The main constraints are due to the size of payload and instrument in satellite borne experiments, which intrinsically limit their effective area and thus their sensitivity at very high energies, as the detectable photon flux is also rapidly decreasing with energy. To overcome this problem, ground based Cherenkov telescopes are used to detect VHE γ-rays. In Atmospheric Cherenkov Technique (ACT), the Earth's atmosphere is used as a part of the detector, which allows huge detector volumes. The ground based TeV γ-ray astronomy was practically started with the detection of Crab nebula by Whipple observatory above 500 GeV [20] in 1989. Since the detection of the Crab Nebula, TeV γ-ray astronomy has grown slowly, but steadily, throughout the 1990s and the early 2000s. This field has matured significantly over the past five years due to the availability of a third generation of Cherenkov γ-ray observatories. The number of sources detected has grown rapidly from a handful to 143 [21]. More significantly, an increasing number of classes of sources have been established as TeV γ-ray emitters, including BL Lac objects, radio galaxies, quasars, shell-type supernova remnants (SNRs), pulsar wind nebulae (PWNe), X-ray binaries, and stellar clusters. The third generation ground based telescopes with lower threshold and greater sensitivity, such as MAGIC II, HESS II and VERITAS have started detecting new sources every month. A TeV γ-ray sky is shown in Figure 1.2. γ-ray sources can be mainly divided into two categories (I) galactic and (II) extragalactic sources.

1.2 Cosmic rays

Cosmic rays (CR) were discovered by Victor Hess almost a hundred years ago. Cosmic rays are charged particles incident on the Earth from outer space. Victor Hess discovered that the flux of these CR's does not change significantly during the day or night time, using ground as well as space based experiments (balloon-borne-detector), and then concluded that this charged particle radiation does not come from the Sun. 96% of these particles are protons and rest 4% consists of alpha

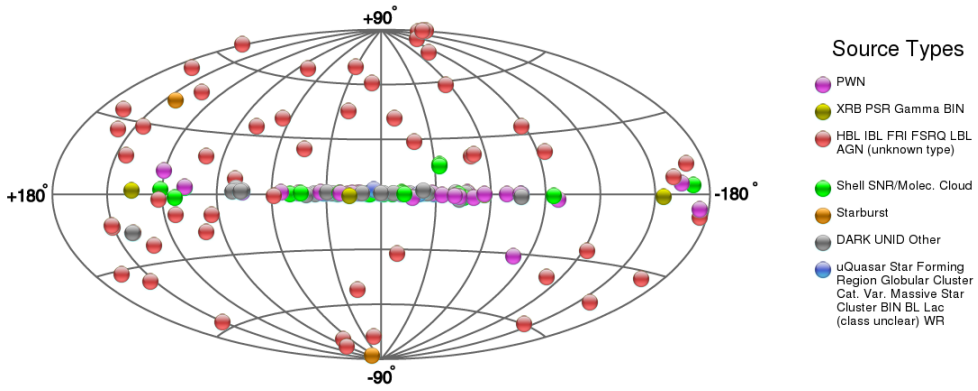

Figure 1.2: TeV γ-ray sky, Figure obtained from [21]

particles, heavy nuclei and electrons. The origin of these charged particles have been a mystery since their discovery. The CRs are mostly charged particles and they get deflected by the intergalactic magnetic fields and lose the information on their origin during their travel through the universe, making the understanding of their origin very difficult.

The energy spectrum of the CR is shown in Figure 1.3. The CR spectrum is characterized by a steep power law slope of an index of 2.7 till energies 100 TeV, which is generally referred to as the knee region. The CR spectrum changes slope from 2.7 to 3 from knee to ankle at energies of $\sim 10^{18}$ eV and again starts flattening above these energies. This change of slope in the spectrum is also not very well understood. The reason for the change in slope at knee region is presumably due to higher energy protons produced within the Milky Way not being confined anymore to our Galaxy. The changes in the spectral slope at knee at $\sim 10^{14}$ eV and at the ankle $\sim 10^{18}$ eV suggest that different energy cosmic rays are probably accelerated and produced via different processes from a variety of sources. Since the discovery of CR, there has been a great interest in understanding their origin, and how these particles are accelerated to very high energies.

Although it is generally believed that the bulk of Galactic cosmic rays are accelerated at shock fronts of supernovae remnants, no convincing evidence has been

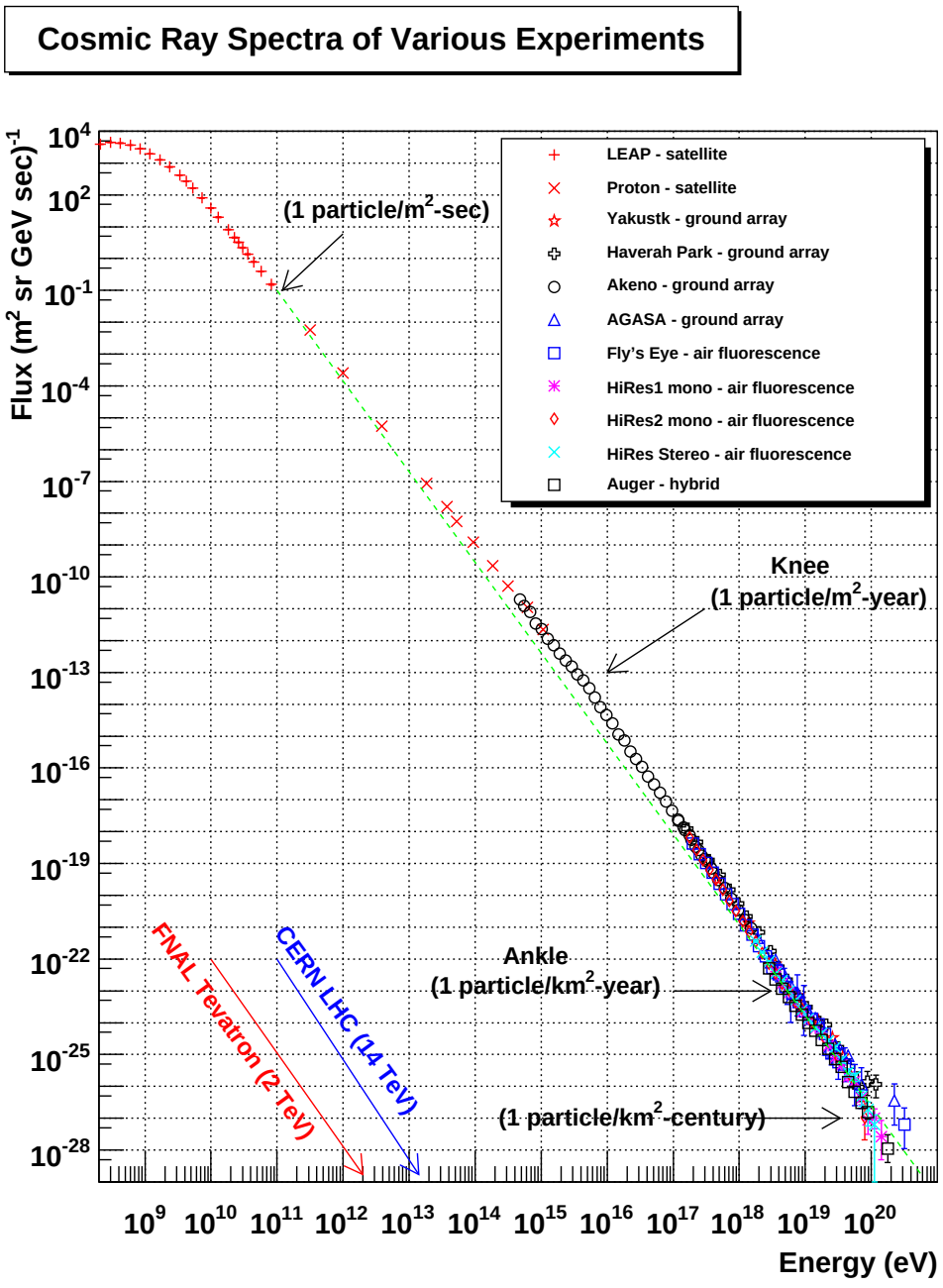

Figure 1.3: The primary cosmic ray differential energy spectrum, obtained from [22]

detected. The HESS collaboration detected a supernova shell SNR RX J1713.73946 at TeV energies in 2004 , which may accelerate particles to such energies [23]. The origin of cosmic ray above the energy 10^{15} eV is believed to be extra galactic and these CRs may be accelerated at the shock front in the active galactic nuclei (AGN) jets or/and Gamma-Ray Bursts.

The basic power law behavior of the cosmic ray energy spectrum can be explained by the Fermi acceleration processes, formulated by E. Fermi in 1949 [24]. Fermi's original idea suggests that charged particles will gain energy while being accelerated when they are repeatedly reflected by clouds of ionized interstellar gas (magnetic mirrors). If such clouds have predominantly random directions of motion, then the frequency of head-on collisions between the cosmic rays and the clouds would exceed the rate of tail encounters, leading to a net acceleration of a particle. But, it was realized later that such a mechanism is too slow to accelerate particles to very high energies. Fermi also postulated that particles can be accelerated at shock fronts, and this mechanism is responsible for particle acceleration in strong shocks, and is referred to as diffuse shock acceleration. When a shock propagates through the plasma, and charged particles cross the shock front iteratively from downstream to upstream, and vice versa, particles are accelerated more efficiently.

Fermi acceleration only applies to particles with energies exceeding the thermal energies. The environment for Fermi mechanisms (first and second order) to be effective should be collision-less, as frequent collisions with surrounding particles will cause severe energy loss and as a result, no acceleration will occur. A power law index close to 2, an outcome of the diffuse shock acceleration mechanism, is found to be consistent with the observed index of cosmic ray spectrum. This strengthens the belief that cosmic ray can be accelerated at shock fronts in astronomical sources.

Recent results from the Pierre Auger Observatory show that ultra-high-energy cosmic ray arrival directions appear to be correlated with extragalactic supermassive black holes at the center of nearby galaxies called active galactic nuclei [25]. However, since the angular correlation scale used is fairly large (3.1 degrees), these results do not unambiguously identify the origins of such cosmic ray particles. Cos-

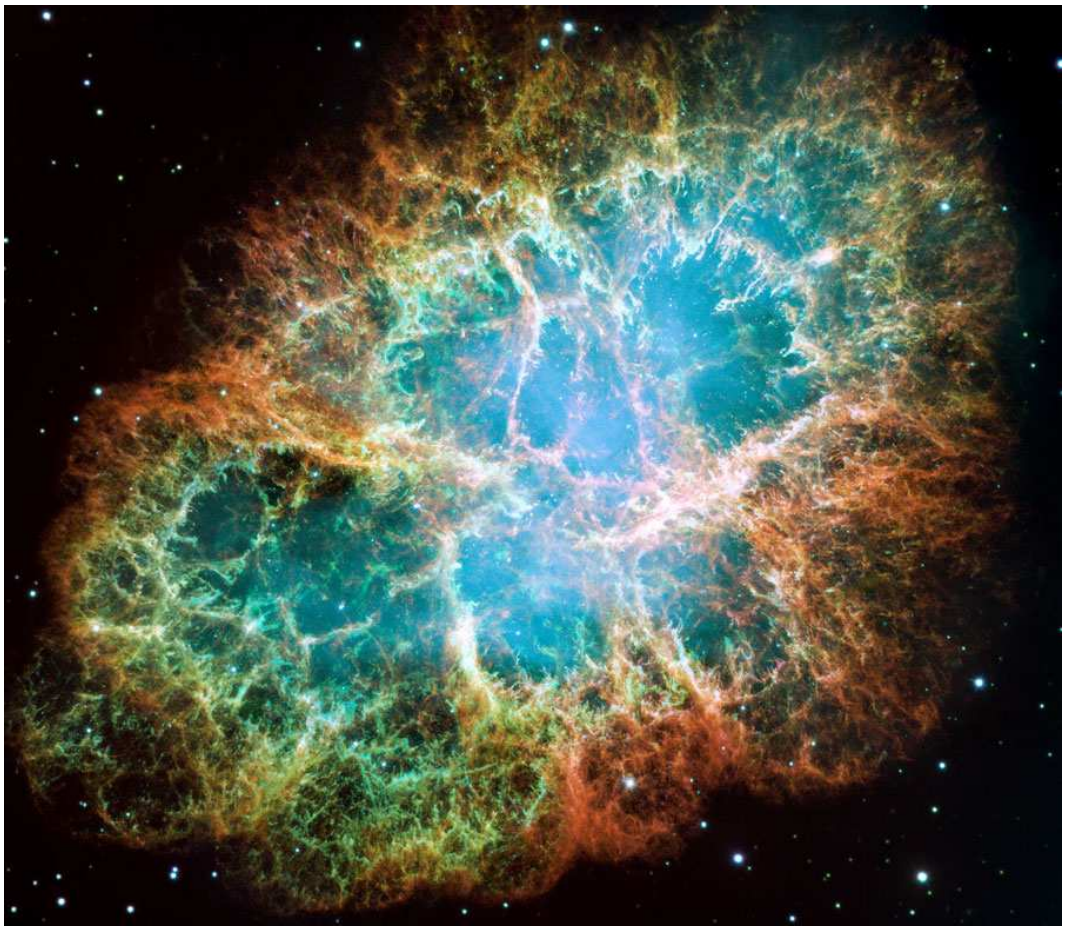

Figure 1.4: Optical image of Crab Nebula taken by HST [28]

mic rays with energies above 10^{18} eV, also known as "Ultra-High Energy Cosmic Rays" (UHECR) interact with the Cosmic Microwave Background (CMB) causing the Greisen-Zatsepin-Kuzmin (GZK) cut-off at $\sim 10^{20}$ eV [26, 27].

1.3 VHE γ-ray sources

γ-rays are mainly emitted by non-thermal sources in the universe, tracing the most violent and energetic phenomena at work inside our Galaxy and beyond. These

phenomena include supernova explosions, particle winds and shocks driven by neutron stars spinning on their axes, and superluminal jets of active galaxies powered by super-massive black holes. Observations of VHE γ-ray sources have provided a great opportunity to understand and study the non-thermal emission from different types of sources such as active galactic nuclei (AGN), pulsars, X-ray binaries (XRB), Pulsar Wind Nebula (PWN), supernova remnants and star burst galaxies.

1.3.1 Pulsar Wind Nebula (Galactic)

A pulsar wind nebula is a nebula powered by the wind of a pulsar. PWNs are often found inside the shells of supernova remnants in their early stages of evolution. PWNs are the largest VHE γ-ray sources known amongst the Galactic sources. The first TeV γ-ray source discovered, the Crab Nebula, is also a PWN, and it was discovered by HEGRA telescope in 1989. An optical image of Crab Nebula obtained with the HST is shown in Figure 1.4. The current understanding of the emission of VHE γ-ray photons from PWN are that they are produced in three distinct regions. The MeV to GeV emission is produced within the light cylinder of the pulsar's magnetosphere by synchrotron, curvature or inverse Compton radiation. The γ-rays of energy range of 10 GeV to 1 TeV can be produced through the relativistic bulk-motion Comptonization, and the broad-band emission is produced in the nebula via synchrotron and inverse Compton (IC) mechanisms [29]. Figure 1.5 shows the various emission mechanisms and zones.

1.3.2 Supernova Shell (Galactic)

Cosmic rays below the knee region in the cosmic ray spectrum (around 1 PeV) are considered to have originated within our Galaxy. These CRs might be accelerated by diffusive shock present in the supernova shells. The first detection of VHE γ-ray from a supernova shell was that of Cas A by the HEGRA telescope [30]. These VHE γ-rays might have originated by the interaction of accelerated electrons with

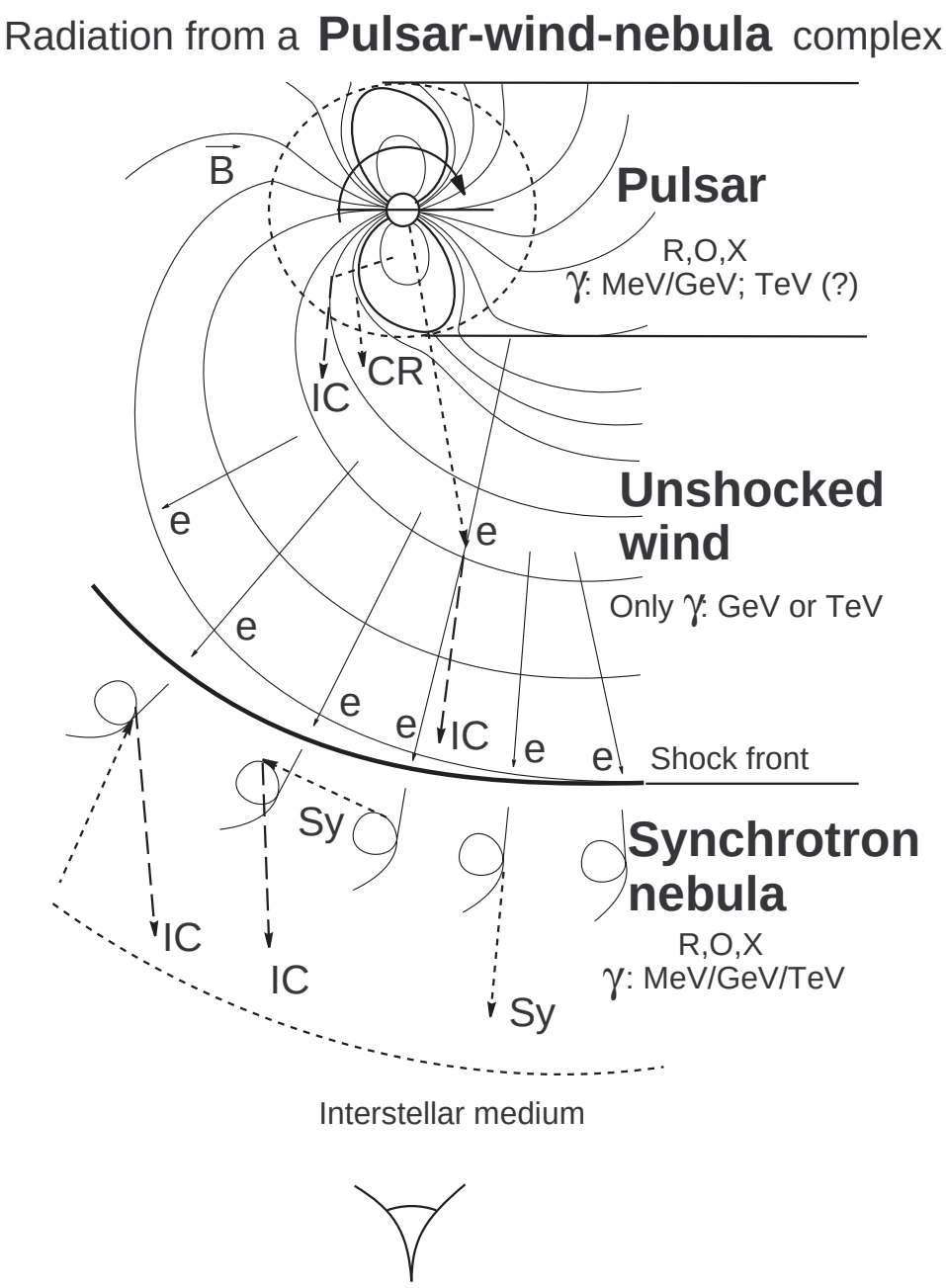

Figure 1.5: Various emission mechanisms and zones of pulsar wind nebula are shown [29].

ambient gas in leptonic models, or pion decay in hadronic models.

1.3.3 X-ray Binaries (Galactic)

X-ray binaries (XRB) are typically composed of a very compact object such as a black hole or a neutron star and a companion star. There are two different theories of VHE γ- ray emission from XRBs. The first is that the compact object has a structure similar to the AGN, called microquasar, and the emission mechanism would be rather similar to the AGN, but at much smaller scales. The second assumes that the VHE γ-ray emission is produced in a system made of a pulsar and massive star, where the γ-rays are generated in the shock from the pulsar wind interacting with the massive companion. Currently, just a handful of VHE γ-ray emitters are known to be in binary systems.

1.4 Active Galactic Nuclei (Extra-galactic)

Galaxies are gravitationally bound systems consisting of stars, stellar remnants, an interstellar medium of gas and dust, and dark matter. A sub-class of galaxies emit extremely luminous emission from their nuclear regions. This emission is spread widely across the electromagnetic spectrum from radio wavelengths to γ-rays. These compact regions at the centers of galaxies that have much higher luminosity than the rest of the galaxy, in the entire electromagnetic spectrum, are called active galactic nuclei (AGN). The spectral continuum emission coming from these nuclei is characterized as non-thermal emission and cannot be attributed to stars. The radiation from AGN is believed to be the result of the accretion of matter onto a supermassive black hole of mass 10^8- 10^{10} $M_\odot$, which resides at the center of the host galaxy. The study of AGN began in early 1900s when E. A. Fath observed a spiral galaxy, NGC 1068, at the Lick observatory in the year 1908.

Some of the active galaxies also show collimated relativistic jets emanating from the nucleus and extending to hundreds of kilo-parsecs. The energy which drives the

nuclear activity is believed to come from the release of gravitational potential energy of surrounding material falling on to supermassive black hole (SMBH) via an accretion disk which radiates powerfully across much of the electromagnetic spectrum. In addition to the great energy output, AGN can be highly variable.

Typical AGN include (i) seyfert galaxies which have modest luminosities (L$\sim 10^{44}$ erg s^{-1}). These objects are well studied since they generally are at lower redshifts (z$\sim$ 0.2); (ii) quasars, which are more luminous (L$\sim 10^{46}$ erg s^{-1}) than the host galaxy and found further away (z$\sim$ 2); and (iii) blazars. Blazars are characterized by nonthermal emission extending from radio to high energies. It is generally believed that the broadband radiation originates within a relativistic jet that is oriented very close to the line of sight of the observer.

1.4.1 The Unified Model

Despite the large diversity in the AGN, they seem to share some common properties. Therefore, it is useful to attempt to construct a detailed classification scheme and develop a Unified Model of AGN. One of the most accepted unification models of Active Galactic Nuclei is that suggested by Urry and Padovani in 1995 [31], who postulated that all the observed differences among the AGN are due to orientation effects with respect to the line of sight to the observer. The AGN are classified by their random pointing directions to the observer in the unified scheme.

According to this model, all classes of AGN host a super massive black hole at their center, whose gravitational potential is the source of AGN luminosity. The SMBH-accretion disc system releases a large fraction of its gravitational energy in the form of radiation, via heating of the accreting material (the standard model for this was proposed by Shakura & Sunyaev in 1973 [32]). This accretion disk emits thermal radiation ranging from optical to X-rays. This accretion disk and SMBH are surrounded by a thick dusty torus that emits thermal radiation which falls at IR wavelengths. Rapidly moving clouds which produce Doppler broadened emission lines are located above (and below) the accretion disk. These clouds are responsible

for the broad lines. Further out from the disk, slower moving clouds produce narrow emission lines. In radio-loud AGN, powerful, relativistic jets of particles flow out from the region near the central black hole, oriented generally perperpendicular to the accretion disk. The radiation emitted by these jets are mainly non-thermal synchrotron radiation. Sometimes these jets also emit high energy radiation via inverse Compton or some hadronic processes. A schematic diagram of AGN as described by Urry and Padovani is shown in Figure 1.6. This diagram shows the basic ingredients of the standard model of AGN, and it also shows the differences among the different types of objects that are observed in the sky. The taxonomical diversity of AGN can be readily understood from this diagram.

In addition to orientation based model, AGNs are also classified in two groups according to their radio emission, (i) radio loud and (ii) radio quiet. This classification is made using the radio-loudness parameter (R) which is defined as the ratio of the 5 GHz radio flux to the B-band optical flux of the source $R = F_5/F_B$. A bimodal distribution is seen using this classification for a sample where most of the galaxies are clustered at R < 1 and 10% of them are at R >1.5 [33], (see Figure 1.7). The Radio-quiet galaxies are further divided depending on the optical spectral line widths.

In the Urry and Padovani's model, if the AGN is observed edge-on and its line of sight to observer is close to the torus plane then the BLR is obscured by the torus, hence only the narrow line region (NLR) is visible, and these AGN appear as a Seyfert II (SyII) galaxy in the case of radio quiet AGN, and narrow line region galaxy (NLRG) in case of radio loud AGN. But, as the observer's line-of-sight moves away from the plane of the torus and the line of sight is close to the axis of the torus, the broad line region (BLR) is visible, and the AGN appears as a Seyfert I (Sy I) galaxy in the case of radio quiet AGN and broad line region galaxy (BLRG) in case of radio louds. This happens until a face-on view of the jet is attained and its non-thermal, featureless continuum emission starts to dominate the entire source spectrum due to strong relativistic boosting effects. Blazars or a flat spectrum radio quasar (FSRQ) are observed in this orientation. Sy II and NLRG are an observer's

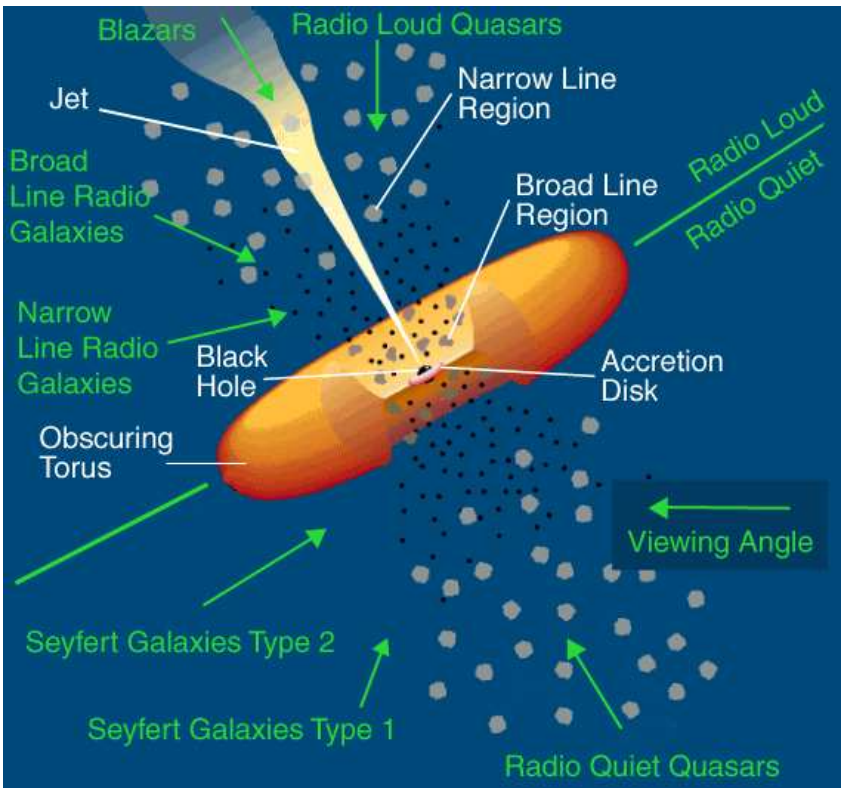

Figure 1.6: Unification scheme of AGN showing how the different classes of sources result from the relative orientation between observer and jet-accretion disk geometry. The image was adapted from Urry & Padovani (1995).

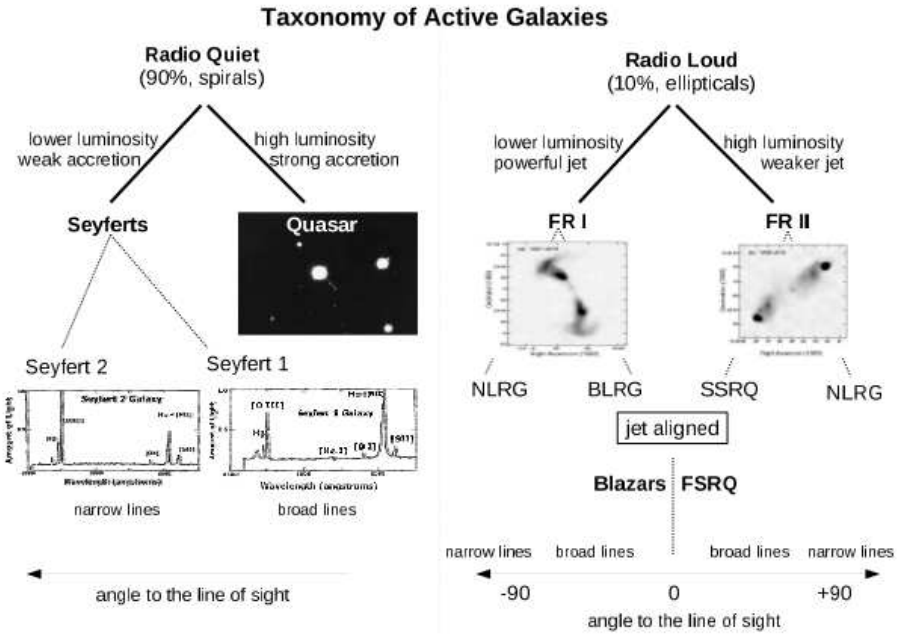

Figure 1.7: Classification of AGN, image taken from [34]

equatorial view of an AGN, Sy I and BLRG are an intermediate view, and blazar & FSRQ's are a face-on view.

1.4.2 Blazars

Blazars are radio-loud AGN that display highly variable, beamed, non-thermal emission, covering a broad range, from radio to γ-ray energies. Blazars are the most powerful sub-class of AGN comprising FSRQ, OVV and BL Lac objects characterized by very rapid variability, high and variable polarization, superluminal motion, and very high luminosities. As mentioned earlier, blazars are radio-loud AGN which possess relativistic jets pointing towards the Earth (line of sight of the observer), and are therefore characterized by a dominant, featureless non-thermal continuum emission. This emission is thought to originate in the relativistic plasma jet which is believed to be powered and accelerated by an accreting, billion solar mass black hole. The radiation is boosted due to bulk relativistic motion of the emitting plasma that causes radiation to be beamed in a forward direction, making the variability appear more rapid and the luminosity higher than in the rest frame. The present understanding about the energy and origin of the jets in the AGN comes from the Blandford-Znajek [35] processes. The energy of jets is gained from the energy and angular momentum of the rotating black hole in the BZ process. In Blandford-Payne (BP) process, the jet energy is extracted from the disk matter by virtue of frozen poloidal magnetic field lines in the disk [36]. The rapid variability of these objects implies that the extreme emission is produced within highly compact regions, and the small angles to the line of sight result in relativistic effects such as beaming and apparent superluminal motion.

1.4.3 Relativistic Effects: Beaming and Doppler Boost

When an emitting source moves with a relativistic velocity towards the observer, the observed flux is Doppler boosted due to relativistic effects. This effect is known

as relativistic beaming. In the case of blazars, the angle between the jet and the line of sight of observer is close to zero, so the intensity of the emitted radiation from the jet is boosted significantly for the observer due to relativistic bulk motion of the jet. In addition, the relativistic Doppler effect can significantly boost the frequency at which the radiation is observed. The Doppler boosting factor (Doppler factor), δ, of an object, which is moving at with velocity v, can be defined as

$$\delta = [\Gamma(1 - \beta \cos(\theta))]^{-1}, \tag{1.1}$$

where β is the bulk velocity of the object in units of the speed of light, θ is the angle between jet axis and the line of sight in the observer frame.

$$\beta = \frac{v}{c} \tag{1.2}$$

and Γ is the bulk Lorenz factor of the object defined in terms of bulk velocity of the object

$$\Gamma = \frac{1}{\sqrt{1 - \beta^2}} \tag{1.3}$$

1.5 Emission models

The spectral energy distribution (SED) of blazars is characterized by nonthermal continuum emission extending over twenty orders of magnitude. This non-thermal emission shows two humps in ν vs νF_ν representation (Figure 1.8). In order to explain the structure of the SED, different emission models can be considered. The low energy peak can be attributed to synchrotron radiation from relativistic electrons. The origin of high energy peak is still highly debatable and different possible scenarios based on either leptonic or hadronic induced γ-ray emission are introduced. The observed radio emission from blazars is the total flux density of the source integrated over the whole source extension. The low-frequency radio observations performed with single-dish instruments have a relatively large contamination from non-blazar

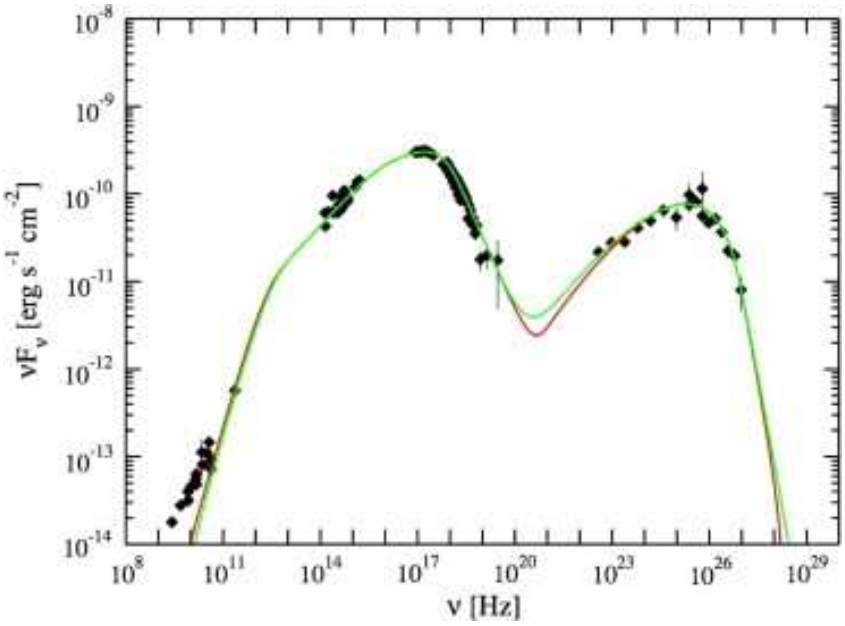

Figure 1.8: SED of Mrk 421 shows two hump in ν vs νF_ν representation [7]

emission due to the underlying extended jet component, and hence they only provide upper limits for the radio flux density of the blazar emission zone. Therefore one zone SED models under predict radio flux as these models only estimate flux from the core.

1.5.1 Leptonic Models

The leptonic models of blazars assumes that both low energy and high energy hump originate in the relativistic jets due to synchrotron and inverse Compton (IC) radiation of the same population of directly accelerated electrons. The high energy electrons are accelerated at the shock front which produces TeV photons. In the simplest scenario, a single homogeneous spherical region moving down stream (away from the source) in a relativistic jet, populated by non-thermal electrons and uniform magnetic fields, emits both the synchrotron and IC radiation.

Synchrotron Self Compton

Synchrotron Self Compton (SSC) model is the most widely accepted and popular emission model for blazars, especially for TeV blazars. In the SSC model, the energetic electrons interact with the magnetic field to emit synchrotron emission. These synchrotron photons act as the seed photons for emission of higher energy photons by the same population of electrons via IC scattering [37, 38, 2, 39]. More complex scenarios are introduced by considering multizone SSC models [40] or Mirror models where synchrotron photons reflect back to the jet from the BLR and act as seed photons [4]. A one zone homogeneous SSC model developed by Krawczynski et. al. [8] is discussed in §4.3.4.

External Compton

External Compton (EC) model also assumes that the low energy hump is caused by the interaction of electron with magnetic field, but the high energy hump is produced via IC scattering of external photon fields. These external photons can be from the optical-UV emission from the accretion disk [3, 41] and the IR radiation field produced by the torus or from the BLR region [4, 42].

1.5.2 Hadronic Models

The hadronic models suggest that TeV emission is produced by π° or charged pion decay with subsequent synchrotron and/or Compton emission from decay products, or synchrotron radiation from ultra-relativistic hadrons. In this alternative scenario, it is assumed that AGN jets consist of hadronic matter (electron-proton plasma) and protons are accelerated along with electrons, and the high-energy component is produced via photo-pion interactions [43, 6, 44]. The target photons for photo-pion interaction may either be produced inside the jet via synchrotron emission from a coaccelerated population of electrons [45], originate outside the jet [46, 47, 48], or be produced via synchrotron emission from the protons themselves [5, 49]. The protons

need to be accelerated to very high energies ($> 10^{18}$ eV) in hadronic models to provide sufficient γ-rays flux inside the jets. Particularly, in the proton synchrotron and proton-radiation interaction models, protons have to be accelerated to close to 10^{20} eV. Moreover, in order to make the proton synchrotron radiation become an effective mechanism of γ-ray production, the emission zone needs a strong magnetic field, close to 100 G. As leptonic models predict co-related variability in X-rays and γ-ray bands, hadronic models uniquely predict the production of neutrinos. However neutrinos have to be still detected from a blazar. Detection of neutrinos from the blazars would be a definitive proof in favor of hadronic models.

The pions decay giving rise to γ-rays, electrons, muons, and neutrinos. The strong magnetic fields required to collimate the hadronic jets also lead to the generation of considerable synchrotron radiation by protons and charged leptons in the pair cascade. The electrons from the pair cascade contribute to the lower energy synchrotron peak, whereas the muons together with the secondary photons from neutral pion decay contribute to the higher energy γ-ray peak.

1.5.3 Motivation for Blazars study

Blazars are excellent laboratories to study the environment within the jets of active galactic nuclei, as dominant part of the observed nonthermal emission from AGN originates within them. The emission from the jets of blazars is spread widely across the electromagnetic spectrum from radio wavelengths to γ-rays. Blazars display extreme flux and spectral variability on multiple timescales over a broad energy range. Their multiwavelength flux and spectral studies have also provided substantial progress to understanding blazars jets.

The content of these jets is highly debated. It is unclear whether the jet content is mostly electron-positron pairs (leptonic jets), or electron-proton pairs (hadronic jets), or if the jets are particle starved and magnetic field (Poynting flux) dominated instead.

Inspite of the progress that has been made to understand the blazar jets, several key questions are still unanswered. Some of the open questions are (i) the content of their jets, whether these jets are composed of electron-proton plasma or electron-positron plasma; (ii) the location and structure of their dominant emission zones; (iii) the origin of observed variability on timescales from minutes to tens of years; (iv) the role of external photon fields in VHE γ-ray production; (v) the particle energy distribution and the dominant acceleration mechanism for the underlying radiating particles; (vi) the role of magnetic fields in the origin, confinement and propagation of relativistic jets. The main reason behind these unanswered questions is the lack of data in the energies from 100 MeV to hundreds of GeVs, where the second hump of the SED peaks in blazars.

1.6 Thesis Summary

We present in this thesis multiwavelength studies of two blazars that emit in the TeV energy ranges. The TeV observations have been made using HAGAR telescope, while the rest of the multiwavelength data are obtained from various data archives. Using these studies, an attempt is made to understand some of the physical processes that produce the observed SEDs.

Chapter 1 provides a brief introduction to the field of γ-ray astronomy. The main source of γ-rays are discussed in this Chapter, with an emphasis on the AGN.
Chapter 2 discusses the basics of atmospheric Cherenkov technique, the HAGAR telescope and its data reduction methods.
Chapter 3 explains briefly other multiwavelength instruments and their data reduction procedure which are used in the study.
Chapter 4 outlines the multiwavelength studies of the TeV blazar Mrk 421 during its giant flare and moderate activity state.
Chapter 5 discusses the detection of Mrk 501 by HAGAR telescope and its multiwavelength study during 2011. We also discuss a viable mechanism to explain rapid scale variability seen in the source.

Conclusions based on the work presented in this thesis are presented in **Chapter 6**, the final chapter. Future plans related to the present work are also discussed in this Chapter.

Chapter 2

Atmospheric Cherenkov Technique

2.1 Introduction

The Earth's atmosphere is opaque to high energy γ-ray photons from the celestial sources as they are completely absorbed. Therefore, they cannot be detected by detectors situated on the ground. The low energy γ-ray observations are possible using high altitude balloons and space based satellite instruments. But, space-based detectors become less effective in detecting high and very high energy (10 GeV - 100 TeV) γ-ray photons due to their small collection areas, which are generally limited to a few hundreds of square centimeters. The flux of γ-ray photons from cosmic sources in the (10 GeV - 100 TeV) VHE range falls very rapidly, which makes detection of these high energy photons very difficult by spaceborne instruments. But these VHE γ-ray photons can be detected using Atmospheric Cherenkov Technique (ACT) [50, 51]. This technique uses the Earth's atmosphere as the detection medium, enabling a large collection area (several hundreds of square meters).

The showers of secondary particles are produced when a VHE γ-ray or cosmic ray interacts with the air molecules at the top of the atmosphere. These showers are known as extensive air showers (EAS) and can be detected on the ground. The secondary particles of these showers are very energetic and move at nearly the speed

of light. If the speed of these particles is faster than the local speed of light in air they emit Cherenkov radiation. The Cherenkov light emitted from an air shower is rather bright, but extremely short-lived. The shape of these air showers is like an ellipsoid which points back to the origin (incoming γ-rays or cosmic rays). The Cherenkov light produced by these EAS can be detected using an array of optical detectors having fast camera/photomultiplier tubes (PMTs) at ground level.

Cosmic ray air showers are much more common than γ-ray air showers and are a source of background, or noise, to a γ-ray telescope. They are less uniform and larger than the γ-ray air showers. They spread more laterally, due to large transverse momentum of secondary particles, than γ-ray air showers and they are not constrained to an ellipsoid. Also, the secondary particles are created much deeper in the atmosphere in case of cosmic ray air showers.

Atmospheric Cherenkov Technique covers the VHE range. This technique is blooming in the recent years because of its advantages over the spaceborne missions in the VHE γ-ray energy regime.

A detailed description of the ACT and various aspects of this technique are presented in this Chapter. The basics of EAS and Cherenkov emission are also discussed. The HAGAR telescope, its design and electronics used in the telescope are presented in great detail. The data analysis technique, simulations and calibration of the telescope are also discussed.

2.2 Extensive air showers

The Earth is continuously bombarded by charged particles from the outer space, which are known as cosmic rays. The composition of cosmic rays is dominated by protons (96%). Helium nuclei and other heavy nuclei, γ-rays, $e^- - e^+$, etc constitute the remaining 4%. When a cosmic ray particle reaches the Earth's atmosphere, it collides with the nucleus of Nitrogen or Oxygen high in the atmosphere. This interaction produces a shower of secondary particles. These secondary particles

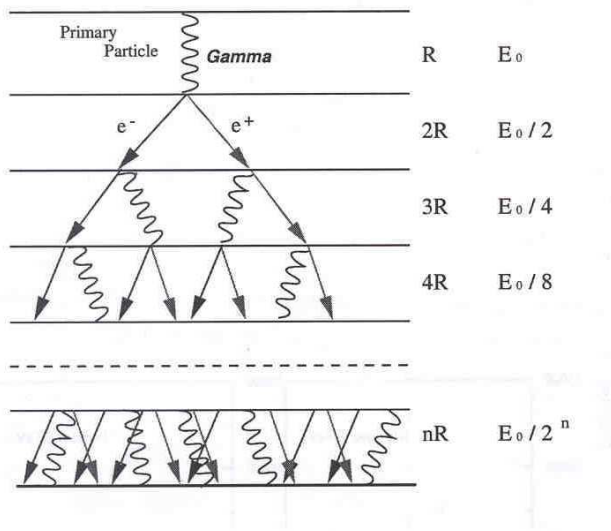

Figure 2.1: Extensive Air Showers initiated by a γ-ray based on Heitler's model (1954)

share the primary particle's energy. These secondary particles subsequently collide with other nuclei in the atmosphere, creating a new generation of energetic particles. This process continues as long as the particles have sufficient energy to interact, and this results in a particle cascade. The EAS was discovered by Rossi, Schmeiser, Bothe and Auger in 1930s.

2.2.1 γ-ray initiated shower

When a γ-ray enters the Earth's atmosphere it interacts with the Oxygen or Nitrogen nuclei of air molecules. Three effects can take place in this radiation-matter interaction depending upon the energy of incident photon. They are: (a) photo-electric effect, (b) Compton scattering and (c) pair production. If the energy of the incident γ-ray photon is higher than the pair-production threshold of 1.02 MeV, the incident photon produces an e^- and e^+ via pair production. If this pair has

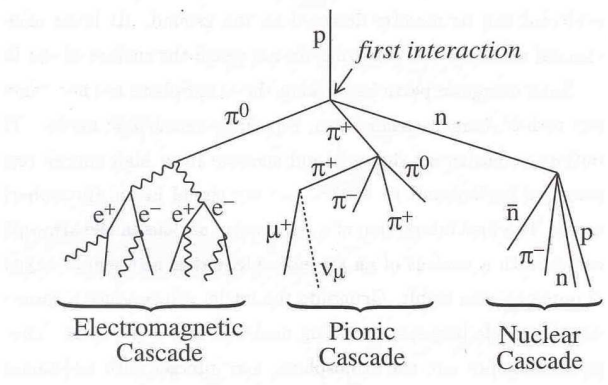

Figure 2.2: Model of a cosmic ray induced extensive air shower.

sufficient energy, it interacts with another nucleus in the atmosphere and produces γ-rays via bremsstrahlung radiation. And, if this γ-ray photon which is produced via bremsstrahlung emission still has energy higher than 1.02 MeV, it again produces $e^- - e^+$ pairs which may again undergo interaction with another nucleus and produce more bremsstrahlung emission. Thus, these two processes produce a cascade of particles, constituting electrons, positrons and photons and, as a result of this cascade an electromagnetic (EM) air shower develops. This particle shower propagates in the longitudinal direction and spreads over laterally too in the atmosphere. Pair production and bremsstrahlung processes continue until the mean particle energy drops below the critical energy ($\sim$ 80 MeV), where the energy loss of electrons by ionizations of air molecules become dominant over the bremsstrahlung emission. Then, the electromagnetic shower reaches its maximum particle number and no further particles are created, and all the shower energy is used up to ionize the medium, and is thereby dissipated.

Now, we can define a characteristic length for the bremsstrahlung emission which is the mean free path of the process. This is called radiation length ($X_\circ$). The radiation length ($X_\circ$) is the mean distance over which a high energy electron loses all but 1/e of its initial energy $E_\circ$ via bremsstrahlung emission. This radiation length ($X_\circ$) is measured in gm/cm^2.

The energy loss of an electron via bremsstrahlung emission is proportional to its energy:

$$-\frac{dE}{dx} \propto \frac{E_\circ}{X_\circ} \tag{2.1}$$

The integration of the above equation provides :

$$E(x) = E_\circ . e^{-x/X_\circ} \tag{2.2}$$

The value of radiation length ($X_\circ$) in air is = 37.2 gm/cm^2

The main properties of the electromagnetic shower can be explained by using a model developed by Heitler [52]. A simple model is presented here to understand the EM cascade. This model assumes that the energy of the primary particle is equally divided between the secondary particles, and considers only bremsstrahlung and pair production processes for photon and $e^- - e^+$ generation. The radiation length and conversion lengths (the attenuation length due to pair production) are also considered to be equal to $X_\circ$. The number of particles at the shower maximum can be derived using above model. After the n^{th} branching, the shower consists of $N(x)=2^{x/X_\circ}$ particles, each having energy of

$E(x)=E_\circ 2^{-x/X_\circ}$,

where x is the distance traveled along the shower axis. An image of electromagnetic shower based on the Heitler's model, is shown in Figure 2.1.

2.2.2 Hadronic Showers

The high energy particles such as protons and heavy nuclei from cosmic rays also undergo a similar process as γ-rays when they reach the Earth's atmosphere. These particles interact with a nucleus in the air at a typical height of 15 to 35 km from the ground and produce a shower of secondary particles. A hadronic air shower has three components (1) hadronic, (2) electromagnetic and (3) muonic. The most frequently produced secondary particles are charged ($\pi^\pm$) and neutral (π°) pions.

The production of secondary particles in a hadron cascade is caused by hadronic processes via strong interaction. Along with charged and neutral pions, kaons, nucleons and other hadrons are also produced with lower multiplicities. In each hadronic interaction, one-third of the energy of the primary particle is transferred via π° decay to the EM shower component. The charged pions ($\pi^{\pm}$) decay further into charged muons ($\mu^{\pm}$) depending on its energy. These charged muons further decay into electrons and neutrinos, or interact with air nuclei and produce secondary particles. An image of hadronic air shower induced by cosmic ray based on the Heitler's model is shown in Figure 2.2.

The strong interaction governs the hadronic process and all the processes are shown below. Here τ is the decay times of the respective interaction:

$$\pi^{\circ} \rightarrow 2\ \gamma \qquad \tau = 1.8 \times 10^{-16} sec \tag{2.3}$$

$$\pi^{\pm} \rightarrow \mu^{\pm} + \nu_{\mu}(\bar{\nu}_{\mu}) \qquad \tau = 2.5 \times 10^{-8} sec \tag{2.4}$$

$$\mu^{\pm} \rightarrow e^{\pm} + \nu_{\mu}(\bar{\nu}_{\mu}) \qquad \tau = 2.2 \times 10^{6} sec \tag{2.5}$$

The neutral particles decay immediately into two photons ($\pi \rightarrow 2\gamma$) which constitute the EM part of the hadronic shower.

2.2.3 Basic differences in EM and Hadronic showers

The hadronic air showers have several differences with EM air showers. These differences arise due to particle content, and development of these showers in the atmosphere. Hadronic shower penetrates much deeper into the atmosphere than EM shower because the interaction length of hadrons is higher compared to the radiation length of VHE γ-ray photons. The lateral distribution of these air showers

Table 2.1: Differences in EM and Hadronic showers

Properties -	γ-ray	Proton
Particle content	e^+, e^-, γ-ray	$\mu^{\pm}$, $\pi^{\pm}$, π°, n, p, e^+, e^-
Penetrates into the atmosphere	Less than proton induced shower	More than γ-ray induced shower
Lateral distribution	Less than proton induced shower	More than γ-ray induced showe
Interaction length (gm/cm^2)	$\sim$48.5	$\sim$ 80

is also different because of the difference in the mechanism by which the showers are generated. In the case of EM showers, the elastic multiple Coulomb scattering of electrons is responsible for lateral distribution, and scattering angle of electrons with energy close to $E_c \sim 80$ MeV is small, which makes the lateral spread of the EM shower smaller than that of the hadronic showers. Lateral spread of hadronic showers is more due to the transverse momentum obtained by the secondary particles. A comparison of simulated EM and hadronic shower is shown in Figure 2.3. Differences between EM and Hadronic showers are listed in table 2.1.

2.3 Cherenkov emission

Cherenkov radiation is an electromagnetic emission which is radiated when a charged particle passes through a dielectric medium at a velocity greater than the speed of light in that medium. As the charged particle passes through, it disturbs the local electromagnetic field of its medium. This disturbance caused by passing charge particle displaces the electrons in the atom and polarizes them. As the charge passes away, electrons come back to their original place by emitting Cherenkov radiation. Pavel Cherenkov detected this phenomenon experimentally in 1934 and a theoretical explanation of this effect was developed by Igor Tamm and Ilya Frank, who shared the Nobel Prize with Pavel Cherenkov in 1958.

When a charged particle passes through a dielectric medium at a velocity greater than the phase velocity of light in that medium ($v > c_m$), it momentarily polarizes the medium by pushing like charges in the atom away, and inducing a dipole state as shown in Figure 2.4 (b). This polarization state is only symmetric in the azimuthal plane, but not along the axis of motion, and a cone of dipoles develops behind the electron. This polarization produces a dipole field in the dielectric which collapses with the emission of Cherenkov radiation. This radiation would be emitted perpendicular to the surface of this cone. The Cherenkov radiation is emitted at an angle that depends on the refractive index of the medium and is beamed in the forward direction [53].

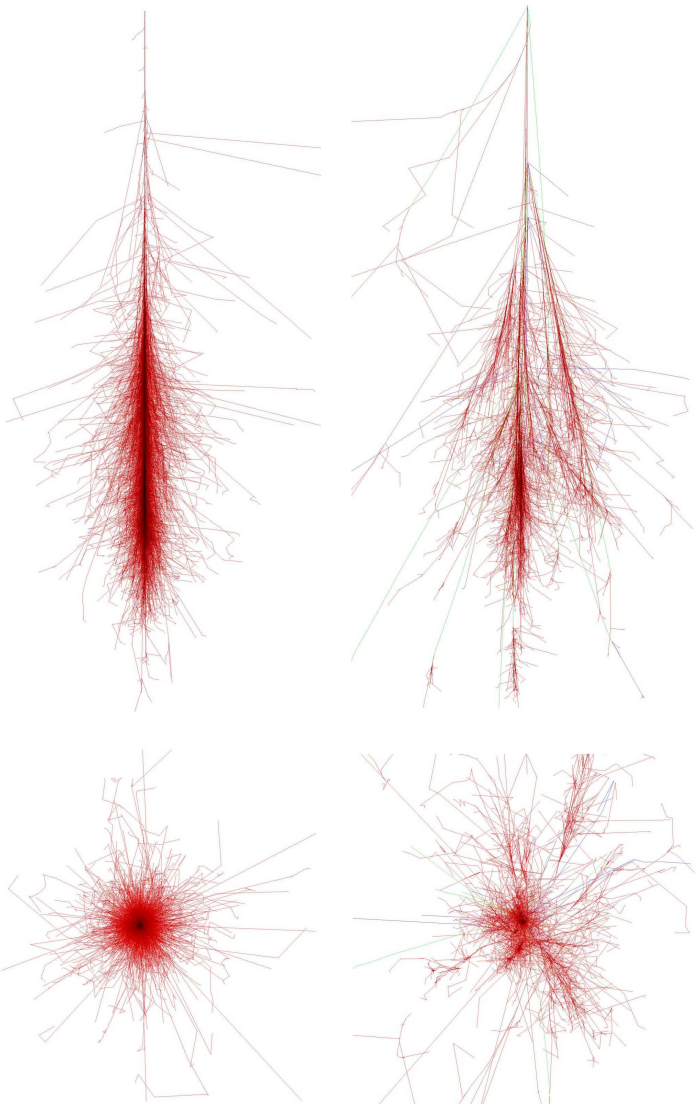

Figure 2.3: Corsika simulations of photon (left) and proton (right) induced EAS, assuming an energy of 100 GeV. The upper parts represent shower evolution while the bottom ones are the projected view at ground (taken from F. Schmidt, CORSIKA Shower Images, http://www.ast.leeds.ac.uk/ fs/showerimages.html)

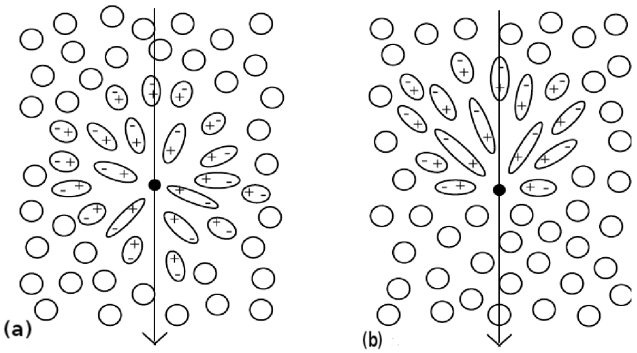

Figure 2.4: Polarization set up when a charged particle passing through a dielectric medium with (a) v< c/n (left) and (b)v> c/n (right)

Slow moving particles (v < c_m) also polarize the medium, but this polarization state is perfectly symmetrical with respect to particle position as shown in Figure 2.4 (a). Due to this symmetry, no electric field develops at long distances and thus no radiation is emitted. This emission is coherent [54] in nature and observed at a an angle Θ as shown in Figure 2.5.

Suppose, the Cherenkov emission, which is coherent in nature, is emitted when a particle moves in a dielectric from position A to B. As shown in Figure 2.5 the light also travels from point A to point C in the same time. Waves from arbitrary points P1, P2 and P3 over the track AB are coherent and combine to form a plane wavefront BC. If the velocity of the particle is v (or $\beta.c$ where c is the velocity of light in the vacuum) and c/n is the velocity of light in the medium then Θ can be defined as

$$cos\Theta = \frac{\frac{c}{n(\lambda)}.\Delta T}{\beta.c.\Delta T} \tag{2.6}$$

$$cos\Theta = \frac{1}{\beta.n(\lambda)} \tag{2.7}$$

Here ΔT is the time taken by the particle to move from point A to B and n(λ) is the refractive index of the medium at wavelength λ. There is a threshold velocity for a particle in a given medium of refractive index n. Below this velocity no emission

takes place. This threshold velocity corresponds to an energy:

$$E_{min} = \Gamma_{min} m_0 c^2 \tag{2.8}$$

Where

$$\Gamma_{min} = \frac{1}{\sqrt{1 - \beta^2{}_{min}}} \tag{2.9}$$

If particle moves ultra-relativistically, ($\beta \sim 1$), then equation 2.9 becomes

$$cos\Theta_{max} = \frac{1}{n} \tag{2.10}$$

The emission takes place in optical and near optical wavelengths where n(λ) > 1. The emission in X-rays and γ-rays is forbidden as n(λ) < 1. The refractive index of the Earth's atmosphere at ground level is n=1.00029, which corresponds to Θ_{max} of 1.3°. The energy thresholds to produce Cherenkov photons from electron, muon and proton are 21MeV, 4 GeV and 39 GeV respectively. Number of Cherenkov photons produced per unit path length in the wavelength interval λ_1 and λ_2 are

$$\frac{dN}{dl} = 2\pi\alpha(\frac{1}{\lambda_1} - \frac{1}{\lambda_2})(1 - \frac{1}{\beta^2 n^2}). \tag{2.11}$$

Here α is the fine structure constant. Number of Cherenkov photons produced per unit wavelength interval is given by equation 2.12 [51]

$$\frac{dN}{d\lambda} \propto \frac{1}{\lambda^2} \tag{2.12}$$

2.3.1 Cherenkov emission from EAS

The Cherenkov emission produced by EAS is coherent and it can be detected by an array of optical detectors on the ground by using multiple detector trigger against the night sky background (NSB) and ambient light. The effect of NSB and ambient light

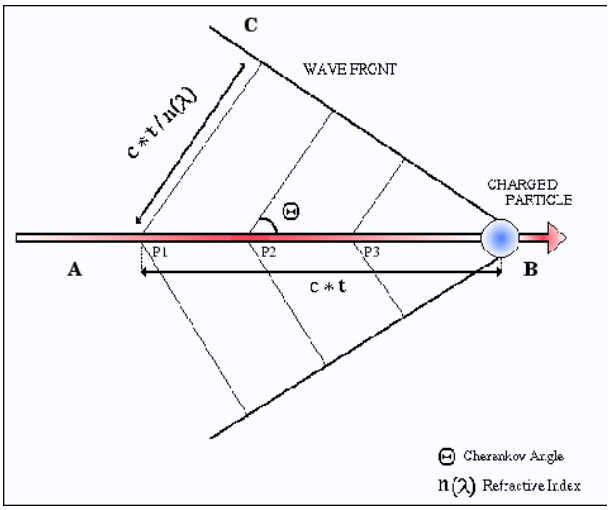

Figure 2.5: Coherent nature of the Cherenkov radiation, Figure taken from [55]

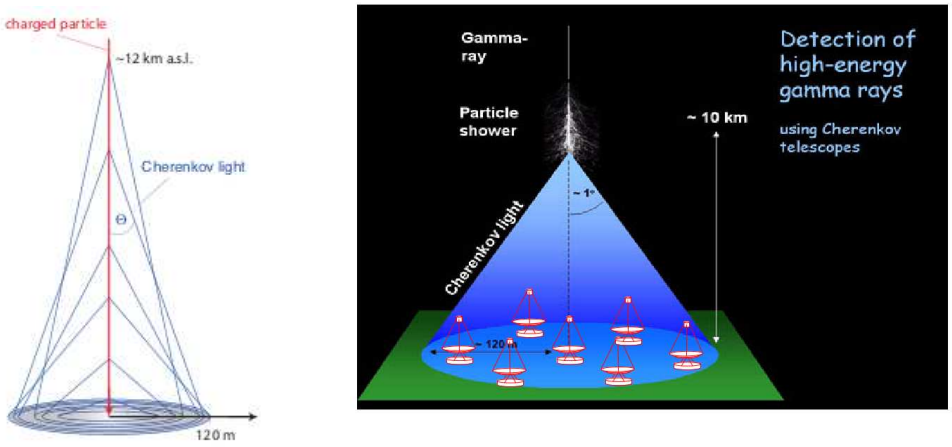

Figure 2.6: Cherenkov light pool

can be minimized as they are not coherent and do not trigger multiple detectors at the same time. The yield of Cherenkov photons is very small (0.36 photons/cm at sea level) in the atmosphere but most of the Cherenkov photons reach the ground level due to less attenuation in the atmosphere. The observed Cherenkov emission has a spectrum ranging from 300-600 nm and this radiation mainly gets attenuated by absorption and scattering processes. Scattering of Cherenkov photons via Rayleigh scattering is the main cause of the attenuation. The UV photons suffer maximum attenuation as cross-section of Rayleigh scattering goes as $1/\lambda^4$.

The Cherenkov light distribution of γ-ray and cosmic ray induced showers are different at the ground. This difference in Cherenkov light distribution is due to the differences in development of air showers in the atmosphere for these two types of showers [56, 57]. The angle of Cherenkov emission is 1° at $\sim$ 8 km height and it increases as altitude decreases. The γ-ray shower shows a hump in the lateral distribution of Cherenkov photons around 120 m from the shower core at sea level [58]. Cherenkov angle increases when a particle travels downwards in the atmosphere due to increase in the refractive index. This hump is produced because of the superposition of the different emitting cones at different altitudes, see Figure 2.6 (left). The effect of the emission at different altitudes cancel the effect of the Cherenkov emission angle. The resulting effect of both the processes focus the Cherenkov photons around 120 m from the shower core. This hump is absent in the proton induced showers due to large transverse momentum of pions. The opening angles of secondary particles in hadronic cascade are much larger compared to the secondary particles of an electromagnetic shower due to large transverse momentum of pions. The opening angles of electrons in the hadronic showers depend on the opening angles of pions. Hence, in hadronic cascade, electrons need to have much higher energy compared to EM cascade for Cherenkov angle to exceed r.m.s. scattering angle plus production angles of pions. In addition to this, the interaction length for a primary proton in the atmosphere is about 80 gm/cm^2 compared to 48.5 gm/cm^2 for γ-rays. Therefore, proton showers will develop further down into the atmosphere, and as a result, there is a more intense pool of Cherenkov light close to the shower axis. So, only very few energetic electrons contribute to the hump. As a result there is no

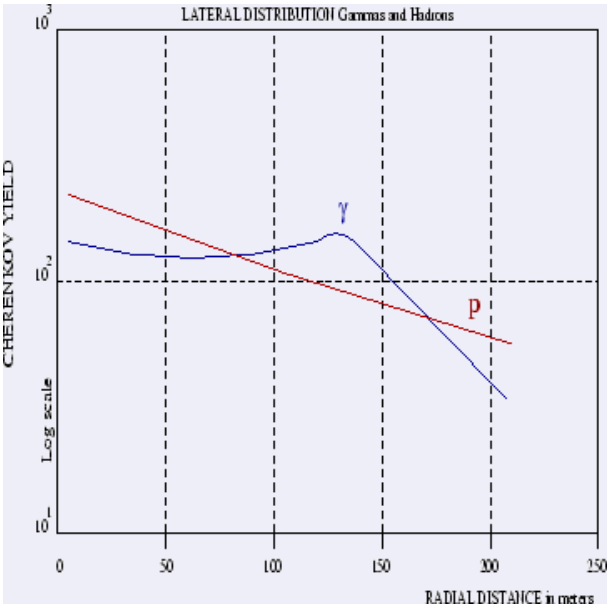

Figure 2.7: Lateral distribution of Cherenkov photons by γ-ray and cosmic ray showers at sea level, Figure taken from [59]

sharp peak in the lateral distribution of hadronic showers. The lateral distributions for γ-rays and hadron initiated showers at sea level are shown in Figure 2.7. The γ-ray shower shows a relatively flat distribution with a hump at 120-130 m from the core, whereas for proton shower, photon density decreases gradually with increasing core distance.

The γ-ray showers also differ from the cosmic rays showers in their lateral timing profiles. Cherenkov wavefront of proton initiated showers have more irregular timing profiles at observation level as these showers are mixture of several sub-showers. This property can also be used to separate the γ-ray induced shower from cosmic ray induced showers. The arrival timing of Cherenkov wavefront as a function of the position on the ground is shown in Figure 2.8 for simulated proton and γ-rays.

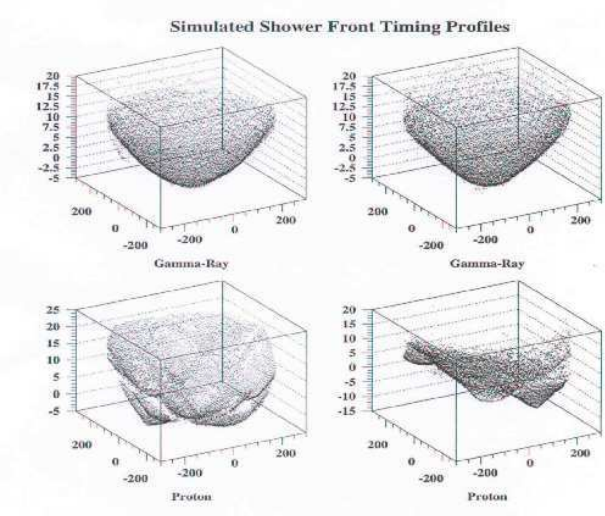

Figure 2.8: Lateral timing profiles of the arrival times of the shower wavefronts at different locations are shown for γ-ray and proton showers. The horizontal axes are positions on the ground, in meters, while the vertical axes are arrival times in nanoseconds [60]

2.4 Atmospheric Cherenkov Telescope

The atmospheric Cherenkov technique is divided into two sub classes, namely, Imaging Atmospheric Cherenkov Technique (IACT) and Wavefront Sampling Technique (WST). These two techniques differ in the methods by which EAS event is reconstructed and the way isotropic cosmic ray background is rejected.

An image of the EAS is obtained in IACT by collecting the Cherenkov photons emitted by that shower using a single large mirror (or small segmented mirrors) and a camera which is placed at the focal plane of the mirror. The energy of the primary particle is computed by the length of the image and the total charge deposited in the triggered PMTs. Direction of the primary incident particle or γ-ray is estimated by the orientation of the shower. There are four IACTs operating globally now:

MAGIC[1], HESS[2], VERITAS[3] and TACTIC.

The lateral distribution of Cherenkov photons is measured in WST. The multiple optical detectors sample the Cherenkov wavefront at different location across the Cherenkov light pool at the ground. This technique exploits the difference of lateral distribution of Cherenkov photons produced by cosmic rays and γ-rays to reject isotropic cosmic rays. The arrival direction and energies of primary particles are obtained by measuring relative arrival time and density of Cherenkov photon at each detector. The density of Cherenkov photons is computed by measuring the pulse height at each PMT. The spatially separated detectors enable us to measure the lateral distribution of Cherenkov photons, estimate the energy of the primary particle and the relative spatial fluctuations.

The timing profile of γ-ray and proton showers are different and this property can distinguish between these two species. The study of timing jitter in the arrival of Cherenkov photons and the pulse shape of Cherenkov photons can be used as a tool to separate cosmic rays from γ-rays. Timing jitter is defined as sigma over mean of arrival times of shower at various mirrors of a given telescope. Pulse shape of γ-ray induced shower is narrower than proton induced shower. In addition to this, proton induced shower pulses also show larger decay time than γ-ray induced shower pulses. The differences in the pulse shape of γ-ray and proton showers can be exploited. Curvature study of the Cherenkov wavefront will lead us to shower parameters such as core location, shower maximum and arrival direction [61, 62, 63]. The arrival angle of the shower can be computed very accurately by fitting a spherical front to Cherenkov wavefront. Off-axis events which are mainly caused by cosmic rays can be rejected once arrival angle of shower is precisely known. This off-axis events rejection improves the sensitivity of the telescope. A 90% rejection of cosmic ray showers and retention of 70% of γ-ray showers will improve the HAGAR sensitivity by $\sim$5 times. If retention of 99% of γ-rays is achieved, then HAGAR sensitivity will reach close to 10 times the present sensitivity.

[1] http://wwwmagic.mppmu.mpg.de/
[2] http://www.mpi-hd.mpg.de/hfm/HESS/pages/about/telescopes/
[3] http://veritas.sao.arizona.edu/

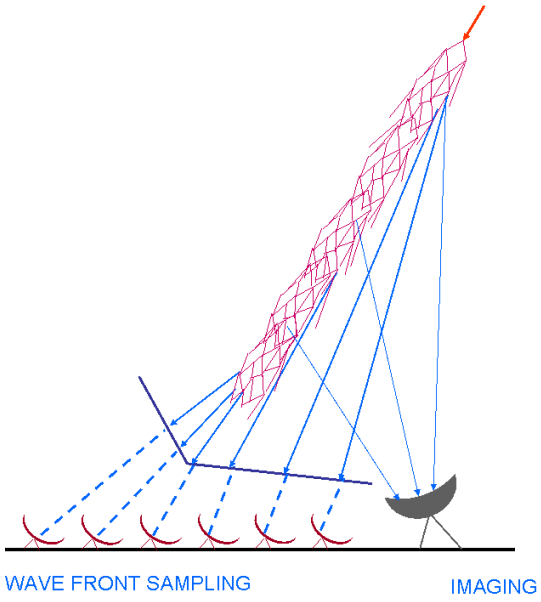

Figure 2.9: Illustration of difference between Imaging technique and wavefront sampling technique to detect Cherenkov emission shown in this schematic diagram.

Figure 2.9 illustrates the differences between the detection techniques IACT and WST. The PACT and HAGAR telescopes are the WST based experiments operational currently in India. Simulations of Cherenkov light pools at ground level produced by a γ-ray of energy 300 GeV and cosmic ray (proton) of energy 1 TeV are shown in Figure 2.10.

2.5 HAGAR Telescope

The High Altitude GAmma Ray (HAGAR) telescope array is an ACT to detect VHE γ-rays from the celestial sources. This array uses the wavefront sampling technique, and is located at the Indian Astronomical Observatory (IAO), Hanle (32° 46′ 46″ N, 78° 58′ 35″ E), in the Ladakh region of India, at an altitude of 4270 m. The main motivation behind setting up this array at a high altitude is to exploit the

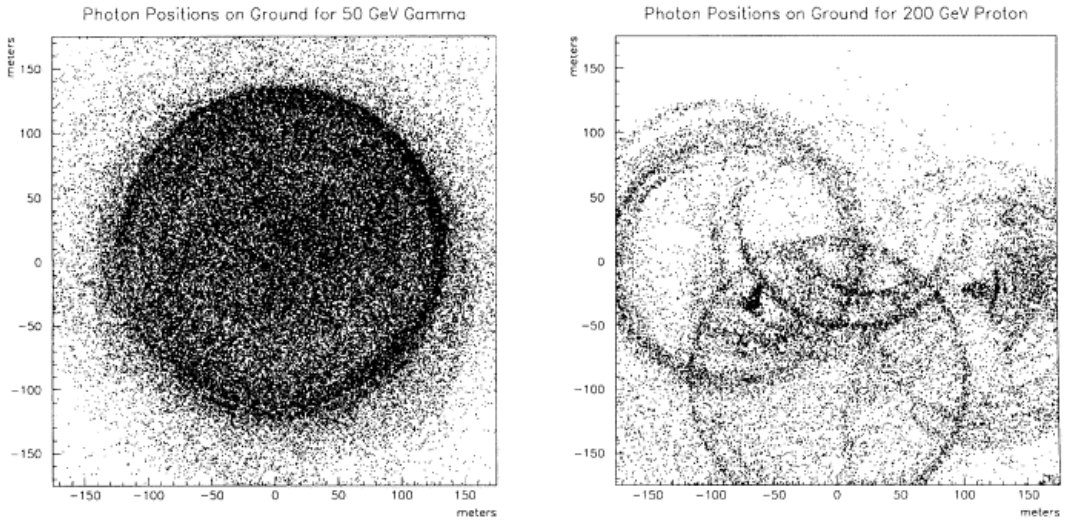

Figure 2.10: The Cherenkov light pool on the ground (sea level). The small black dots are the Cherenkov photons. The left plot is the from a 300 GeV γ-ray shower, the right plot is from a 1 TeV proton shower [64]

higher Cherenkov photon density to achieve a lower energy threshold using modest size telescopes [65]. The lateral distributions of Cherenkov photons were simulated for γ-rays and hadron initiated showers at Hanle. The Cherenkov photon densities at core of the showers were found 4-5 times higher at Hanle compared to sea level as Cherenkov photons suffer only 15 % attenuation at Hanle compared to sea level, where it is close to 50%. The low energy threshold for ACT is achieved by installing HAGAR array at high altitude using small size telescopes.

The Cherenkov hump which is observed in γ-ray induced showers at lower altitudes is absent at Hanle. As altitude of observation increases, shower maximum of a given primary energy comes closer to the observation level. Therefore Cherenkov photons do not get focused and due to this effect hump appears much closer to core and fainter at higher altitudes. At very high altitudes such as Hanle the shower maximum is very close to the observation level, and Cherenkov photons do not get focused. So, no hump is observed at Hanle in the distribution of Cherenkov photons. Due to this effect, γ -ray / proton shower separation will be more complex at this altitude. The simulations of lateral distributions of Cherenkov photons induced

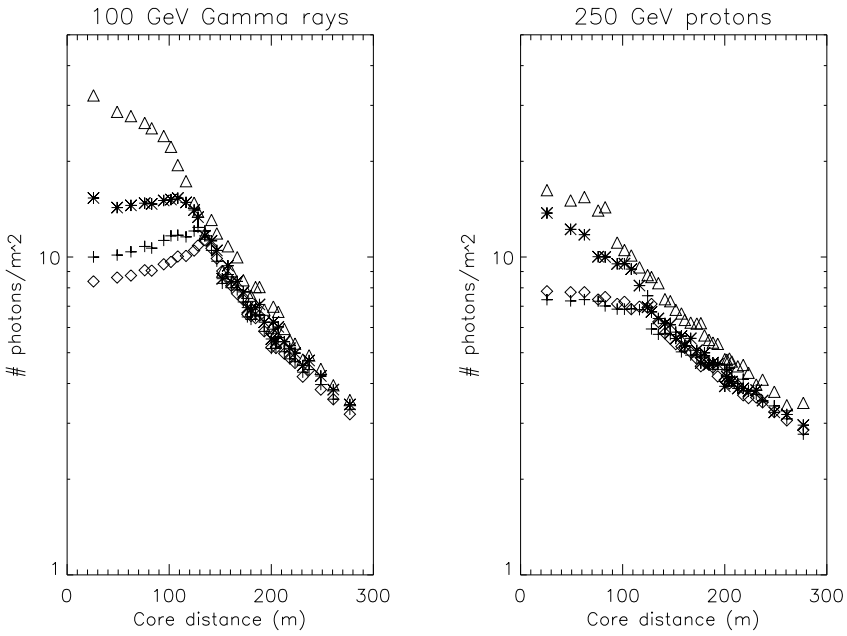

Figure 2.11: Lateral distributions of Cherenkov photons at different altitudes (not corrected for atmospheric attenuation). The open triangles $\triangle$ represent the photon densities at Hanle (4.3 km), asterisks ($*$) represent the photon densities at 2.2 km altitude, plus signs ($+$) represent the photon densities at 1 km altitude and diamonds ($\Diamond$) represent the photon densities at sea level.

by γ-rays and cosmic rays at different altitudes were performed. Higher Cherenkov photon densities were observed at Hanle for both γ-ray and cosmic rays induced showers. Figure 2.11 show lateral distributions of γ-ray and cosmic rays induced showers at different altitudes. The open triangles $\triangle$ represent the photon densities at Hanle (4.3 km), asterisks ($*$) represent the photon densities at 2.2 km altitude, plus signs($+$) represent the photon densities at 1 km altitude and diamonds ($\Diamond$) represent the photon densities at sea level. The Cherenkov photon densities are compared for γ-rays and proton induced showers at Hanle for different energies in Figure 2.12.

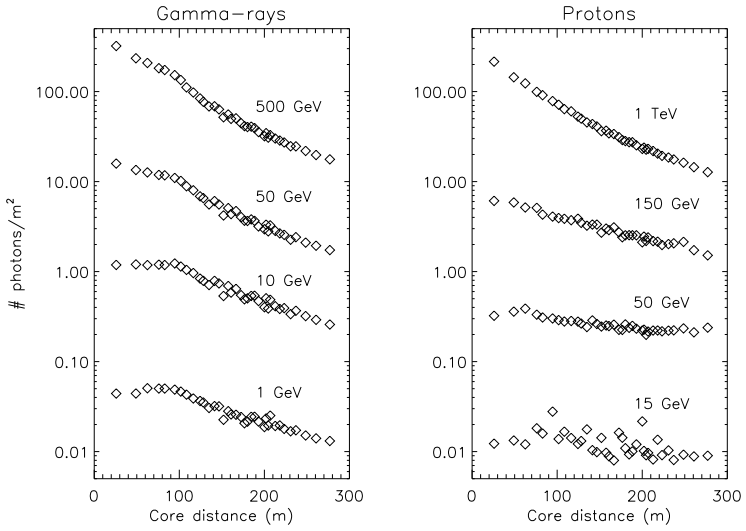

Figure 2.12: Lateral distributions of Cherenkov photons from different energy γ-rays and proton induced showers at Hanle

2.5.1 The Telescope Array

HAGAR consists of an array of seven telescopes in the form of a hexagon, with one telescope at the center. An image and a diagram of HAGAR telescope array are shown in Figure 2.13. All seven telescopes have seven para-axially mounted front coated parabolic mirrors of diameter 0.9 m, with a UV-sensitive photo-tube at the focus of individual mirrors. These parabolic mirrors have f/d ratio of 1 and they were fabricated by using 10 mm thick float glass sheets. FOV of HAGAR telescope is 3°. The photo tubes which are mounted at the focus of these mirrors are manufactured by Photonis (XP2268B). These PMTs have a peak quantum efficiency of 24 % at 400 nm. The specified diameter of photocathode of the PMT is 44 mm and the corresponding field of view is $\sim 3°$. The high voltages fed to these PMT are monitored and controlled by C.A.E.N controller module (SY1527). Each telescope is separated by 50 m distance from its neighbouring telescope.

These telescopes use alt-azimuth mounting. This mount has two axes for supporting and rotating a telescope about two mutually perpendicular axes, one vertical

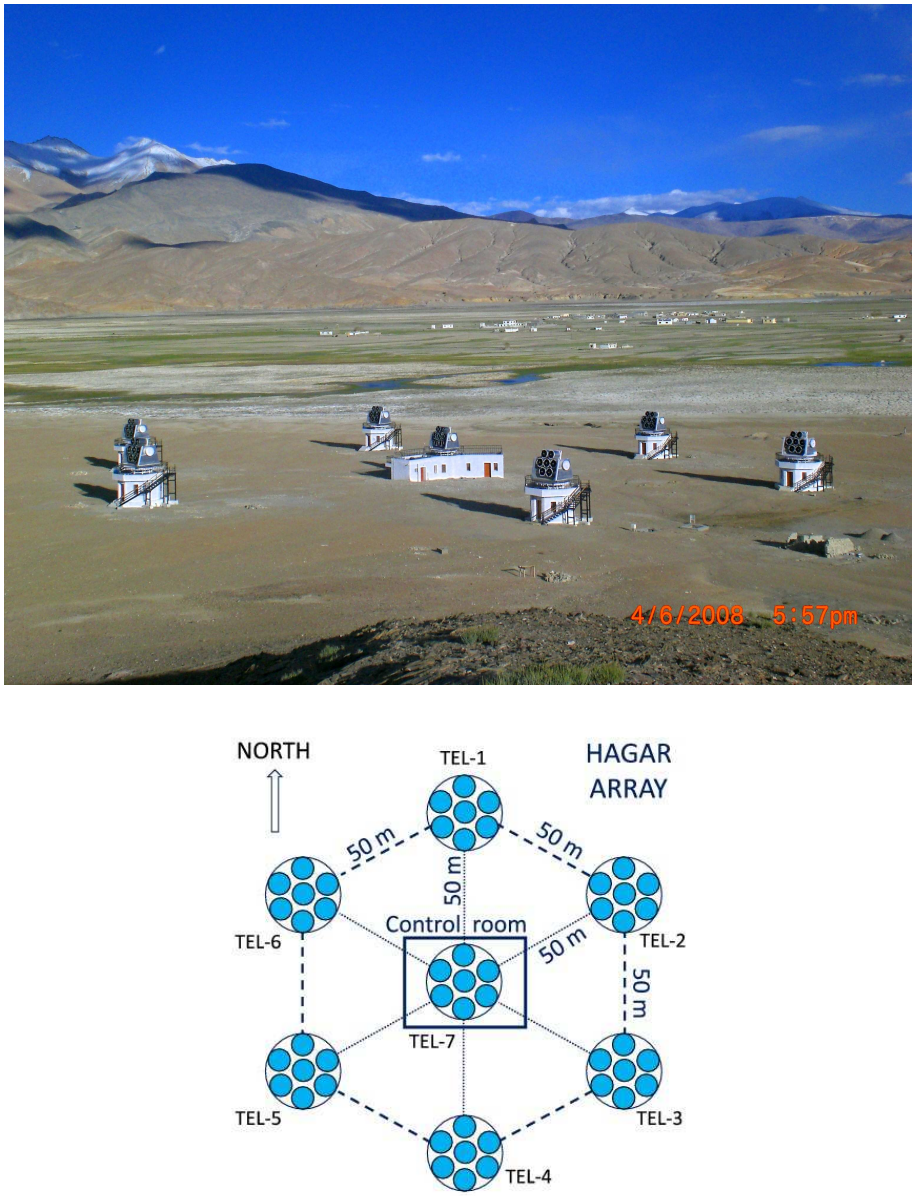

Figure 2.13: HAGAR telescope array at Hanle, Ladakh, India (Top) and its schematic diagram (Bottom)

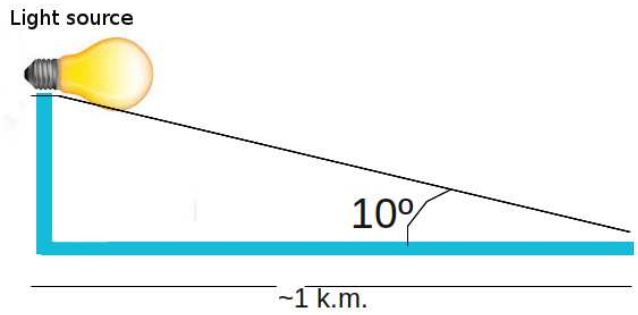

Figure 2.14: The geometric configuration of the co-alignment system between the guide telescope and the seven mirrors.

and the other horizontal. The azimuth can be varied by rotation about the vertical axis and the altitude can be varied by rotation about the horizontal axis. Each axis of the telescope is driven by a stepper motor. The movement control system of HAGAR telescope is made of two 17-bit rotary encoders, two stepper motors and a micro-controller based Motion Control Interface Unit (MCIU). A single control computer provides a user interface, computes the source position in real time and controls the motion of all seven telescopes under program control from the control room below telescope seven. Mean tracking accuracy of the motion control servo is estimated to be about 16 arcsec. The seven mirrors of each telescope are independently mounted on a single platform. It is necessary to ensure that the optical axes of these mirrors are aligned with each other and also with the guide telescope axis. HAGAR mirror may lose 6-12 % of the Cherenkov photons due to a pointing error of 0.2°-0.6°, given that the field of view of the mirror is 3°. The co-alignment between the guide telescope and the seven mirrors is done manually by sighting a stationary distant light source which is situated at a distance of ∼1 km at an elevation angle ∼10°. The geometric configuration of the alignment system is show in Figure 2.14. To align any given mirror, the photo-tube is replaced with a ground glass assembly at the focus. The mounting of the assembly is such that the glass sits at the same

position as the cathode of the photo-tube and one can see the image of the light source directly onto the glass. The centering of the image is achieved by using three tip-tilt screws provided on the back of the mirror cell. Cross wire markings made on the ground glass help to judge the centroid of the image.

A pointing model is needed to transform the star position as seen by the ideal telescope into the position seen by a real telescope. The model is a set of terms, each term being some function of a target position (azimuth and zenith distance) in the sky. The pointing model for HAGAR telescopes is a blend of analytical and empirical terms. The analytical terms attempt to provide pointing corrections based on possible physical misalignments and other mechanical distortions. These terms may also help to trace back to mechanical components of the telescope structure that cause the observed pointing errors. The model implemented for each of the seven telescopes is the same. But the values of the coefficients in the model are different for each telescope. It should be noted that pointing model coefficients are worked out based on the pointing deviations of bright stars with respect to the telescopes. Details of the HAGAR tracking and pointing system can be found in [66].

The pointing error of a mirror in a telescope can have three main components:

1. Pointing error due to error in guide telescope itself.
2. An offset of the mean pointing direction of seven mirrors with respect to the guide telescope axis.
3. An offset of the optic axis of the mirror with respect to the mean pointing direction.

The first two components will have the same errors for all the seven mirrors in a telescope, but the third component will differ from mirror to mirror. A bright star RA-Dec scan is used to estimate these error components.

The region around the telescope pointing direction is scanned independently in RA and declination space for a maximal rate of PMTs pulses in a RA-dec scan.

Figure 2.15: An image of a single telescope of HAGAR array and backend electronics

At the beginning of each scan, the telescope control program acquires and tracks a bright star. Then, a series of manual offsets in the stars RA coordinates are introduced while holding onto the star's declination (i.e. declination offset = 0°). At each step, the PMT pulse rates are recorded for a few seconds. Similarly, a series of manual offsets in declination coordinates are introduced while holding onto the RA coordinate of the star (i.e. RA offset = 0°) and the PMT pulse rates are recorded.

A PMT pulse rate profile as a function of offset angle (i.e. PMT pulse rate vs. offset profile) for a mirror in a telescope is obtained from these scans. The image of the star may not go through the center of field of view of PMT during these two independent scans and the central value of the profile gives the corresponding offset of the star in RA or declination, as the case may be, with respect to mirror axis. These offsets are used to correct the first two error components. The third error component, which originates due to the misalignments of the optic axes of individual mirrors with respect to the mean pointing direction, is fixed by re-aligning those mirrors mechanically using hit and trial method.

2.5.2 Data Acquisition (DAQ) system

The HAGAR data acquisition (DAQ) system is CAMAC-based. The signals from 49 PMTs from all seven telescopes are recorded and monitored by a CAMAC-based system at regular intervals using monitoring interrupts of frequency 1 Hz. Data recorded for each event consist of relative arrival times of Cherenkov shower front at each mirror, as measured by time to digital converters (TDC) with a resolution of 250 ps. A real time clock (RTC) module synchronized with GPS is used to record the absolute arrival time of these events, accurate up to μs. The density of Cherenkov photons at each telescope is measured by the total charge present in PMT pulses (this is recorded by using 12 bit QDCs). The seven PMT pulses of a telescope are linearly added to form a telescope output called the *Royal Sum* (RS) pulse. A coincidence of at least four RS pulses out of seven, above a predetermined threshold, is taken within a time window of 150 ns or 300 ns depending on the zenith angle of the pointing direction to generate a trigger for initiating the data recording. Information on RS pulses are recorded in the same way as the individual PMT pulses. Information of the triggered telescopes on latch and other house-keeping information on various scalar readings are also recorded. In addition, a parallel DAQ using commercial waveform digitizers with a sampling rate of 1 GS/s (ACQIRIS make model DC271A) is also used.

The HAGAR electronics can be mainly divided into two parts, the telescope and the trigger processing electronics. The electronics is duplicated for all the seven telescopes. An image of single element of HAGAR telescope (left) and back-end electronics (right) situated at control room is shown in Figure 2.15. The analog pulses from the 49 PMTs of all the seven telescopes are conditioned, processed for trigger generation and relevant information of the Cherenkov shower is recorded.

The experimental setup for data acquisition and monitoring for the HAGAR array of 7 telescopes is designed under Linux platform. HAGAR DAQ system is handled by several independent computerized systems and they are networked together for data sharing and control. The entire HAGAR DAQ system is easily upgradeable

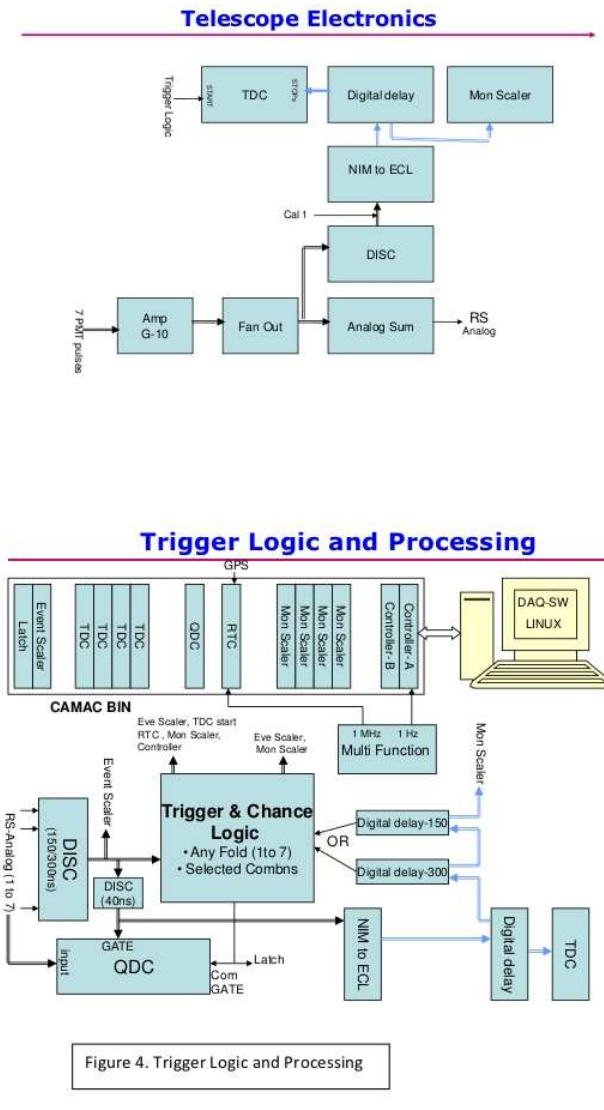

Figure 2.16: Flowchart of the electronics of HAGAR and Trigger system

and it can be made remotely accessible in the future. The main modules of the HAGAR's DAQ system contains :

1. Computerized High Voltage system
2. Electronics and DAQ system
3. Digitizer based DAQ
4. Auxiliary monitoring system

2.5.3 Detector Electronics

The amplitude and relative arrival times of signals from each of the 49 PMTs are to be processed and recorded on each trigger. The shape and amplitude of each pulse is necessary to be preserved to improve the angular as well as energy resolution. Low loss coaxial cables like LMR 400 and RG213 are used to transport the PMT signals from telescopes to control room. Amplifiers are also used for each of these pulses to operate PMTs in low gain for their prolonged operation life in an environment of high night sky background light levels.

The fast pulses from each of the seven PMTs of a telescope are passed through an amplifier of gain 10 in the control room. These analog signals are fanned out to a summing amplifier (FIFO) to get a RS pulse signal and other fan out is converted to a digital signal using discriminator (NIM output). The NIM to ECL module accepts these 7 digital signals from a telescope along with a calibration signal of fixed delay with respect to the trigger to generate differential ECL bus of 8 signals. These bus signals are catered by delay module and monitor scalers in daisy chain fashion. The delayed ECL bus signals are connected to TDC stops and the TDC records relative arrival times of these PMT pulses with respect to the reference trigger (TDC start). Monitor scalers count these signals and PMT rates are read periodically on a periodic monitor trigger. A diagram showing all the modules of the telescope electronics is shown in Figure 2.16.

2.5.4 Trigger and Processing Electronics

As discussed earlier, all HAGAR telescopes use common electronics and the RS analog pulses from all the seven telescopes are fed to a programmable threshold Octal Discriminator to produce desired telescope triggers. We apply a user defined trigger and chance logic which is typically a 4 fold coincidence out of seven telescopes. A final event trigger is generated here. These 7 telescope triggers go as stops to TDC and inputs to Monitor scalers after going through NIM to ECL module and delay module as shown in Figure 2.16 (Bottom). These telescope trigger bus signals are also daisy chained to inputs of two digital delay modules. The delays and output widths in two modules are set for two different trigger coincidence windows and their outputs selectively multiplexed to chance logic to produce coincidence pulse. The event trigger latches telescope trigger status, event time in real time clock (RTC), event scaler, initiates TDC and QDC conversion processes and finally initiates event process. In the event process, all necessary event information are recorded. A periodic 1 Hz pulse triggers Monitor process to record all PMT rates as well as telescope trigger rates.

The CAMAC based RTC is a time keeping module with a precision up to a μ s. The RTC is based on 1 MHz stable clock from oven controlled oscillator. The RTC is synchronized with a GPS system to an accuracy of μs. On a trigger, event time stamp is latched in the RTC and is read in the event process, and monitor trigger time stamp is read in the monitor process using software latch command.

The pulses from PMT are brought down to control room which is situated below the central telescope. The coaxial cable of length of 85 m, LMR-ultraflux-400 cable of 30 m length and RG213 cable of 55 m are used to transmit the pulse from PMT to control room.

Table 2.2: Energy threshold and corresponding collaboration area of HAGAR telescope array

NDF -	Zenith Angle (Deg)	Energy Threshold (GeV)	Collection area $\times 10^8 cm^2$
4 fold	0	204	3.44
5 fold	0	229	2.72
6 Fold	0	257	2.02
7 Fold	0	316	1.40
4 fold	15	214	4.01
5 fold	15	257	3.11
6 Fold	15	275	2.33
7 Fold	15	355	1.73

2.5.5 Simulation

The performance of the IACTs can only be understood by simulations since EAS can not be produced in the laboratory. In the absence of direct calibration, simulations play a very crucial role in the calibration of telescopes. The performance of the HAGAR telescope array was studied by simulations, which were performed in two steps: (1) study of Cherenkov emission caused by γ-ray and cosmic-ray-induced air showers in the atmosphere, by using the Monte Carlo simulation package CORSIKA, developed by the KASCADE group [67], (2) study of the response of the array toward the Cherenkov radiation produced by the simulated showers. The performance parameters such as the energy threshold, the collection area and the sensitivity of the experiment are obtained by a detector simulation package indigenously developed by the HAGAR collaboration.

Even in the absence of moon and artificial light, the night sky is not totally dark. Scattering of light in the Earth's atmosphere produces a background of optical light. The sources of this light are both natural and man made. This background is called night sky background (NSB). The main natural sources which contribute to night

sky background are (1) zodiacal light (caused by sunlight scattered off interplanetary dust), (ii) faint unresolved stars and diffuse galactic light due to atomic processes within our galaxy, (iii) diffuse extragalactic light (due to distant, faint unresolved galaxies) and (iv) airglow and aurorae. Apart from these natural sources, light pollution due to scattering of lights of cities also contribute to the local night sky background.

The minimum energy of γ-rays or cosmic rays for which the signal to noise ratio is sufficient to trigger the detector is defined as the energy threshold [68]. The night sky background photons act as noise over the air shower induced signal. The energy threshold of HAGAR telescope is obtained from the differential rate plot which is shown in Figure 2.17. The energy corresponding to the peak of the differential rate curve is conventionally quoted as the energy threshold. The energy threshold of the HAGAR telescope is estimated to be 208 GeV for vertically incident γ-ray showers for a $\geq$ four-fold trigger condition, for which the corresponding collection area is 3.44×10^8 cm^2. We found four fold trigger as optimal to avoid chance co-incident events from NSB. If we increase the triggers condition to higher fold we may be able to further minimize the chance co-incident events from NSB, but at the same time we may also lose low energy events induced by an air shower.

The sensitivity of an atmospheric Cherenkov telescope is determined by its ability to detect a γ-ray signal over the isotropic cosmic ray background. As we know, cosmic rays flux follows the power law spectrum, and the integral γ-ray and cosmic ray flux can be written as

$$F_\gamma(E) \equiv K_\gamma E^{-\alpha\gamma} \qquad ph/cm^2/sec \tag{2.13}$$

$$F_{CR}(E) \equiv K_{CR} E^{-\alpha_{CR}} \qquad ph/cm^2/sec/sr \tag{2.14}$$

Here $F_\gamma(E)$ & $F_{CR}(E)$ are the integral fluxes of γ-rays and cosmic rays respectively. In the above equations, K_γ & K_{CR} are constants and α_{CR} & α_γ are the spectral indices of the cosmic ray and γ-ray fluxes respectively.

If S is the number of γ-rays detected in a given time t then

$$S = F_\gamma(E) A_\gamma t \tag{2.15}$$

where A_γ is the collection area of γ-rays as a function of E in the experiment. Similarly, we can write an equation for the background B

$$B = F_{CR}(E) A_{CR} \Omega t \tag{2.16}$$

where A_{CR} is the collection area of cosmic ray and Ω is the solid angle of the telescope. The spectral index of the cosmic rays is $\alpha_{CR} \sim 1.7$. The minimum number of standard deviations N_σ for the value of $\alpha_{CR} \sim 1.7$ is defined as:

$$N_\sigma \propto \frac{S}{\sqrt{B}} \propto E^{\frac{1.7}{2} - \alpha_\gamma} \sqrt{t} \frac{A_\gamma}{\sqrt{A_{CR}} \Omega} \tag{2.17}$$

HAGAR sensitivity is such that it will detect a Crab-nebula-like source at a significance level of 5σ in 17 hours of observation [69, 70], assuming no additional criteria for the rejection of background cosmic ray events. A plot between observation duration vs source flux in Crab units for detection of source at 5 σ significance level with HAGAR telescope with no cosmic ray events rejection is shown in Figure 2.17. This corresponds to HAGAR sensitivity for Crab Nebula of 1.2 $\sigma \times \sqrt{hour}$.

The collection area in atmospheric Cherenkov telescope is not restricted to the collection area of the reflector. The radius of the Cherenkov light pool is about 120 m at sea level as shown in Figure 2.6. This radius corresponds to a collection area of $\sim 5 \times 10^8$ cm^2. The details of the energy thresholds and the corresponding collection area are provided in Table 2.2.

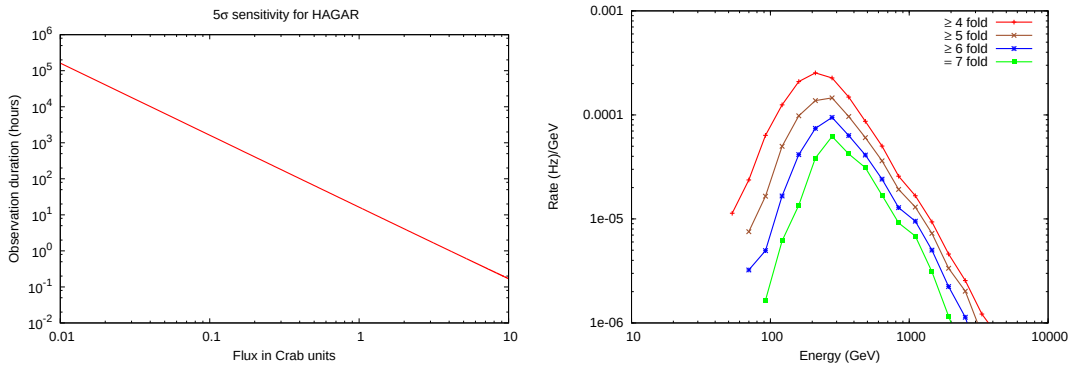

Figure 2.17: Observation duration vs source flux for detection of source at 5σ significance level with HAGAR with no additional criteria for the rejection of cosmic ray events and Differential rate plot for different trigger conditions [70].

2.6 Observations

The observations using HAGAR telescope were carried out on moonless nights by pointing all seven telescopes towards the source or background direction at a time. Each source run (On source) was followed (or preceded) by a background run (Off source). Data selection was done by using parameters which characterize good quality data, in order to reduce systematic errors. Several astronomical sources and fixed angle runs were observed since 2008.

2.6.1 Fixed Angle Runs

When the telescope is pointed towards a dark region in the sky where γ-ray sources are absent, it detects Cherenkov photons only from the cosmic ray shower from that direction. These observations are called fixed angle runs and are used to compute delays present in the system due to electronic or telescope system.

2.6.2 On source

HAGAR telescope observes galactic and extra-galactic sources above 200 GeV. The observations in which telescope observes a γ-ray source is called On source observations. The HAGAR telescope array continuously tracks the source during the observations. Other information regarding night sky background and calibration data are also monitored and stored during these observations.

2.6.3 Off source

The detection of TeV γ-ray emission from any celestial source is very difficult because of the large number of background events coming from isotropic cosmic rays. The signal is buried in the noise all the time and the source will show very small excess over the background. The selection of good and stable background region is one of the most challenging task in HAGAR observations. A γ-ray source free region is selected at the same declination, with the same night sky brightness as that of the source region, as a background region. HAGAR telescope continuously tracks the background during observation, and this observation is called Off source observation. Background observations are made such that they cover the same zenith angle range as that of the source to ensure that the observations were carried out at almost the same energy threshold. A typical exposure of background observation is around 40 min.

2.7 Analysis Procedure

Data reduction technique for HAGAR telescope is derived from the method used for the data analysis of PACT experiment at Pachmarhi [71]. The analysis software is an extension of the software which was used for PACT data analysis. The software is written in IDL, ROOT and Shell Script. HAGAR data analysis can be divided into three main parts : (1) Estimation of electronic delays present in telescopes, (2)

Computation of arrival angle of the air showers and, (3) Signal extraction.

Data analysis starts with the selection of good quality data in order to reduce systematics in results by imposing cuts which characterize the data. Participation of all the seven telescopes in both the source and the background observations is essential. This cut helps in better event reconstruction during plane wavefront fitting. The other main data selection cut is to ensure that the observations were taken at almost the same threshold, which is done by comparing the ON source trigger rate with the off source trigger rate. A low zenith angle cut is also imposed to select the low threshold data. Variation in the trigger rate during the observations are also checked. Most of the time it is caused by the change in the sky conditions at Hanle. If sky condition changes very much during the observations then the data are discarded.

2.7.1 T0 analysis

The estimation of the direction of air shower is done by measuring the relative arrival time of Cherenkov wavefront induced by the shower at each telescope or PMT. This relative arrival time information should be very accurate to obtain the correct direction of the air shower. Difference in cable lengths, difference in PMT transit time or electronics present in telescope introduces some finite electronic delays between pulses from different PMTs. These offsets caused by electronics or telescope system are called T0 and these delays should be corrected before computing the direction of showers. The T0s can be computed by analysis of fixed angle runs or vertical runs.

The difference between expected arrival time to observed arrival time of Cherenkov wavefront induced by an air shower from a fixed angle can be computed for two telescopes placed side by side using the geometry. The average difference between observed and expected time delay is mainly due to the offset caused by the whole telescope and electronics system.

As reconstruction of shower angle will depend upon T0 estimation, we have undertaken a detailed study of T0s and their systematic effects on final results. This analysis also helped us to understand any kind of systematics present in HAGAR system. A basic algorithm is described in following paragraphs to compute T0s from the fixed angle run:

If $T0_i$ and $T0_j$ are the time offsets for the PMTs i and j, we can write an equation of the form

$$T0_i - T0_j = T_{ij} \tag{2.18}$$

Where T_{ij} is the mean delay between a pair of PMTs after correcting for the time difference due to Z-coordinates (height of the PMTs) The total χ^2 of the above equation could be written as

$$\chi^2 = \sum_{i,j=1;i\neq j}^{n} W_{ij}(T0_i - T0_j - T_{ij})^2 \tag{2.19}$$

where n is the total number of PMTs, and W_{ij}'s, are the statistical weight factors. χ^2 minimization will give a set of n equations of the form

$$\sum_{i,j=1;i\neq j}^{n} W_{ij}(T0_i - T0_j) = \sum_{i,j=1;i\neq j}^{n} W_{ij}T_{ij} \equiv T_i^{'} \tag{2.20}$$

Thus we have a set of simultaneous equations, which can be written as

$$WT0 = T^{'} \tag{2.21}$$

in matrix form.
The offsets for (n-1) detectors can be computed with respect to nth detector by solving the above equations and T0's can be computed for each PMT, and for each telescope by using the Royal sum pulse.

2.8 Methods to compute T0

The basic algorithm to compute T0s is explained in the previous section. The Cherenkov light produced by air showers is coherent in nature and is emitted in a very small angle of 1°. The property of the coherent emission of Cherenkov light produced by the air shower is used to discriminate between the light from stars or night sky with the Cherenkov light from air showers. As the Cherenkov light from the air shower is coherent it reaches all the detectors nearly simultaneously. To minimize the effect of night sky background and the light from stars, HAGAR data is recorded only when the RS pulse of at least four telescopes crosses a given discriminator threshold, and triggered the telescopes in a given time window of typically, 150 ns. If n telescopes are triggered we call that event a n-fold event; i.e. if five telescopes are triggered in 150 ns then we call that event a five fold event.

2.8.1 All Events Equal

This is our old method which was used in the analysis of PACT experiment [71, 72]. The T_{ij} distributions are computed from the fixed angle runs regardless of the number of the triggered telescopes and T0s are computed by previously discussed algorithms.

2.8.2 Fold wise Event (NDF)

T_{ij} distributions were computed for each fold (number of triggered telescopes) and T0s are computed only for that fold by the algorithm discussed in previous section. The T0s are estimated for each fold and subtracted for the same fold while estimating the direction of the air showers.

2.8.3 Combination wise (CWT)

The T_{ij} distributions of a given combination of the telescopes are computed. Sixty four combinations are possible with minimum four telescopes trigger in HAGAR system. All sixty four sets of T0s are computed using the algorithm discussed in § 2.7.1. The T0s of a given combination are subtracted from the same combination during the estimation of arrival angle of the air shower.

2.8.4 Arrival direction estimation

The arrival direction of each shower is obtained by reconstructing the shower front using relative arrival times of Cherenkov photons at various telescopes. Cherenkov emission caused by induced air showers forms a spherical wavefront with a large radius of curvature and thickness of $\sim$ 1 m at the observation level. This Cherenkov emission mainly originates at the shower maximum region, which is at a height of about 5 km above the ground level at Hanle. This spherical wavefront is approximated as a plane wavefront in the data analysis procedure, which is a good approximation at the observation level. The arrival direction of each shower in the Cherenkov light pool is computed by measuring the relative arrival times of the shower front at different telescopes. The normal to this plane front gives the arrival direction of the incident shower. The angle between the direction of the shower axis and the pointing direction of the telescope is defined as the space angle (ψ). This is estimated for every event by measuring the relative arrival time of the shower front at each telescope.

Assume two detectors A and B at a distance D from each other as shown in Figure 2.18. A Cherenkov wave front reached the telescope B first and then A after a time delay Δt. The arrival angle θ of the shower could be computed by using the geometry as

$$sin\theta = c\frac{\Delta t}{D} \tag{2.22}$$

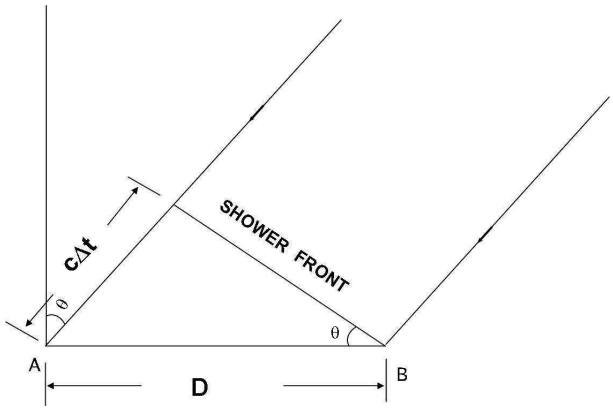

Figure 2.18: Arrival angle determination of a shower using two telescopes A and B separated by distance D

But the actual scenario is more complicated than that explained above. In case of HAGAR we have seven telescopes, so we have used generalized approach. x_i, y_i and z_i are the co-ordinates of the i^{th} telescope, l, m, n are the direction cosines of the shower axis and t_i is the time at which the photon from the shower arrives at the telescope. We can write an equation relating the above quantities as:

$$lx_i + my_i + z_i + c(t_i - t_0) = 0 \tag{2.23}$$

Where c is the speed of the light in vacuum and t_0 is the time at which the shower front passes through the origin of the coordinate system. The above equation could be solved by using χ^2 minimization method to obtain the arrival direction of the shower. The above equation will take the form

$$\chi^2 = \sum_{i=1}^{n} W_i(lx_i + my_i + z_i + c(t_i - t_0))^2 \tag{2.24}$$

where W_i is the statistical weight factor for the i^{th} timing measurement and $t_i$time at which time front arrives at the telescope. The values of l, m, n and t_0 are computed by solving

$$\frac{\delta\chi^2}{\delta l} = 0, \frac{\delta\chi^2}{\delta m} = 0, \frac{\delta\chi^2}{\delta t_0} = 0, and \quad l^2 + m^2 + n^2 = 1 \tag{2.25}$$

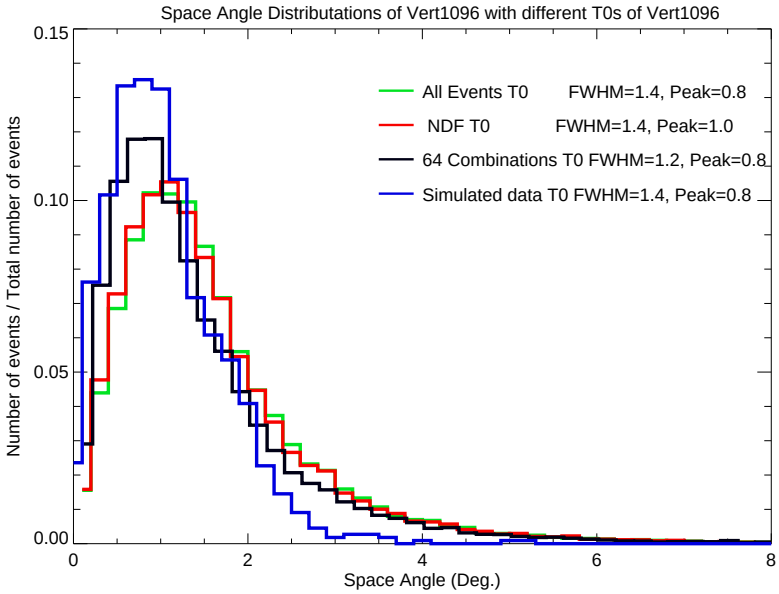

Figure 2.19: Comparison between simulated and observed data

The arrival angles θ and ϕ of the shower are obtained by using these direction cosines, neglecting the terms that contain $\frac{\delta n}{\delta l}$ and $\frac{\delta n}{\delta m}$, as they are very small.

2.8.5 Results and Discussion

Obtaining the best set of T0s for the system from above method is one of the most challenging tasks. We have tested all the three methods mentioned above for computing the best sets of T0s. One way to check which algorithm is best is to compare the obtained space angle distributions (SAD) with the simulated space angle distributions. Narrower distribution implies that the estimation of arrival direction is better for corresponding method. These tests were applied on few Fixed Angle, Vertical and Background runs. SADs were computed with all the three algorithms for these runs and only good quality data are used.

The space angle distributions obtained by using T0s from all the methods for a vertical run are plotted with the simulated data in Figure 2.19. It is clear from

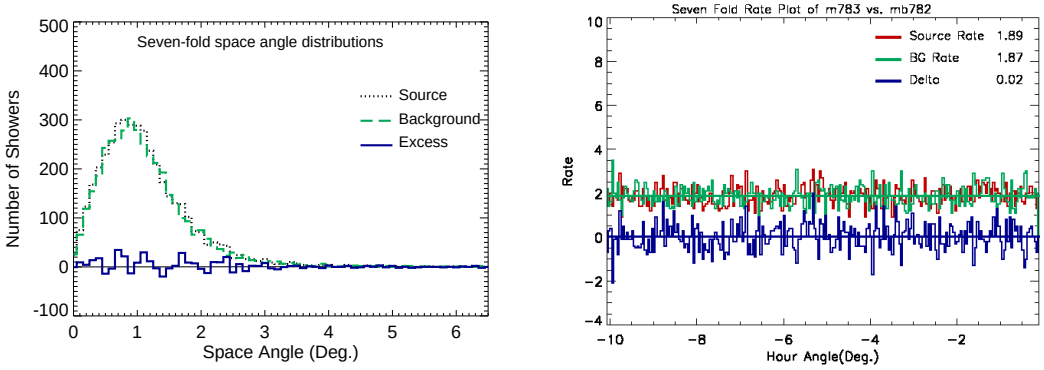

Figure 2.20: Typical space angle distribution plot obtained by HAGAR for a seven-fold trigger (left)and rate plot (Right).

the plot that SAD obtained using CWT (64 Combination wise T0) method is more closely matched to the simulated data. The SADs with other method are broader compared to the CWT method and are not in good agreement with the simulation.

2.8.6 Signal extraction

The observations were carried out by pointing all seven telescopes toward the source or background direction at a time. Each source run was followed (or preceded) by a background run with the same exposure time (typically 40 minutes) and covered the same zenith angle range as that of the source to ensure that observations were carried out at almost the same energy threshold. Data selection was made by using parameters that characterize good quality data to reduce systematic errors.

Extraction of the γ-ray signal was carried out by comparing the ON source and OFF source space angle distributions obtained during the same night. The excess events were computed from 0° to lower limit (LL), where LL is defined as the foot of distant half-maximum point computed by fitting a Gaussian function to the space angle distribution. Background space angle distribution was normalized with source space angle distribution by comparing the tails of the distribution (LL to 6.5°), since no γ-ray events are expected in this region. This normalization is required to

compensate for possible changes in observation conditions or sky conditions during ON source and OFF source regions. Thus the number of γ-ray events is estimated as

$$\text{Number of } \gamma - \text{rays} = \Sigma_0^{LL}(S_i - c_k B_i), \tag{2.26}$$

where S_i and B_i are source and background events, respectively, and c_k is the normalization constant obtained using the tail of the space angle distribution.

A typical space angle plot obtained for the seven-fold trigger is shown in Figure 2.20 (Left). The dotted (black) line histogram corresponds to source observations, the dashed (green) line histogram corresponds to background observations. The histogram shown as solid (blue) line corresponds to the estimation of γ-ray events computed as the excess of ON source events over the normalized OFF source background events. To check the quality of the data an event rate plot is made which is shown in 2.20 (Right). The events rates of On source events, Off source events, and the difference between these two are sampled in every 10 sec. This plot also tells us about the threshold of the observation, if source (On source) and background (Off source) were observed at different thresholds, we will observe difference in the rates. As shown in Figure 2.20 (Right), the difference between On source rate and Off source rate is very small, which implies that both On source rate and Off source observations were made at almost same threshold.

2.9 Calibration of the HAGAR telescope

The HAGAR telescope was commissioned in September 2007 and astronomical observations were started from September 2008. The calibration of the HAGAR telescope was done using simulations, and the comparison of simulations with observations of Crab Nebula. We have also understood the systematics present in HAGAR telescope by analyzing DARK runs. The results are discussed in Table 2.3.

Table 2.3: HAGAR results for Crab Nebula and DARK runs

Source -	Epoch -	Exposure Duration (Hrs.)	Excess -	Error -	Rate (/min)	Signifi- cance (σ)	Number of Pairs
Crab	2009 (Nov.-Dec.)	3.3	1127.9	257.9	5.6±1.3	4.4	6
Crab	2010	5.5	1277.0	346.4	3.9±1.05	3.7	9
Crab (Total)	2009-2010	8.8	2404.9	431.9	4.5±0.8	5.6	15
DARK (Mrk421)	2010	5.3	178.9	426.7	0.56±1.3	0.4	8

2.9.1 Crab nebula

Crab nebula is a part of the remnant of a core-collapse supernova that occurred in 1054 AD at a distance of $\sim$ 2 kpc. Observations of the Crab nebula have been carried out covering the entire electro-magnetic spectrum, resulting in a remarkably well-determined SED, which has made Crab nebula a standard candle source for VHE γ-ray experiments, and is used for calibrating the instruments. The Crab Nebula was observed by HAGAR telescope and analyzed using the data analysis pipeline, discussed in this chapter. The flux obtained from the HAGAR telescope is in good agreement with that of the simulations and other experiments above 250 GeV. The observed integral Crab Nebula flux using HAGAR is $2.4 \pm 0.42 \times 10^{-10}$ ph/cm^2/sec above 250 GeV.

2.9.2 Dark

We have analyzed the Mrk 421 background regions to understand systematics present in the HAGAR telescope using similar analysis discussed in § 2.7. We have used two adjacent background runs to estimate the systematics. The first background run is treated as source and second run as a background run. We have not detected any significant signal from Dark (background) regions which suggests that the systematic errors are small.

2.9.3 Calibration Results

The detailed results of Calibration are shown in Table 2.3. First column contains source names, second column shows the epoch in which source was observed, third column shows the total exposure duration during that epoch, fourth and fifth columns are total excess and its corresponding errors, the sixth column shows the rate of the observed γ-rays during that period. The seventh column shows the significance by which the source is detected and last column tells the number of the pairs,

which are used to obtain the excess, rate, error and significance during that epoch. The results indicate the observations are in good agreement with the simulations, and the systematics errors are small.

2.10 Summary

We have discussed the basic techniques to detect VHE γ-rays at ground using the HAGAR telescope array in this Chapter. The calibration of the HAGAR telescope is also presented. The HAGAR telescope is operating successfully at Hanle since 2007 and several galactic and extra-galactic astronomical sources were observed. Results on a few TeV blazars detected by HAGAR telescope are presented in the coming Chapters.

Chapter 3

Multiwavelength Instrumentation

3.1 Introduction

In this thesis, we have undertaken a multiwaveband study of TeV blazars to understand their global as well as specific properties. The data from ground as well as space based instruments were used in this study. γ-ray observations using HAGAR and optical observations using 2 m Himalayan Chandra Telescope (HCT) were made. Archival UV, X-ray and γ-rays data from *RXTE*, *Swift* and *Fermi* telescopes were used. In addition, fully analyzed optical data from Steward Observatory, and radio data at 15 GHz from Owens Valley Radio Observatory (OVRO) were also used. A brief description of the data, instruments and their analysis procedures, which were used for this study are discussed in this Chapter.

3.2 *Fermi-LAT*

3.2.1 LAT Instrument

Fermi is a γ-ray telescope, launched by NASA using a Delta II Heavy launch vehicle into a near-Earth orbit on 2008, June 11. The *Fermi* telescope was known as the

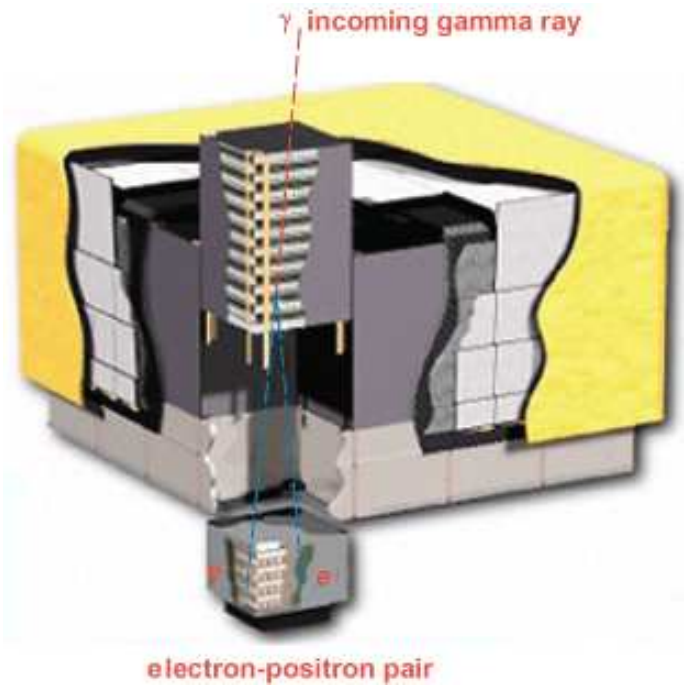

Figure 3.1: Large area telescope (LAT) onboard *Fermi* telescope, Figure taken from [73]

Gamma-ray Large Area Space Telescope (GLAST) before launch and its name was changed after launch to *Fermi*. This telescope is built by joint efforts of NASA, different universities and institutes of USA, Europe and Japan. *Fermi* spacecraft carried two onboard instruments, (1) Large Area Telescope (LAT), see Figure 3.1 and (2) Gamma Ray Burst Monitor. The former is the main instrument onboard *Fermi* Gamma-ray Space Telescope.

LAT is a pair production telescope [16]. It uses high-resolution converter trackers to estimate the directions of the incident γ-rays and a CsI(Tl) crystal calorimeter to measure their energies. LAT has an array of sixteen trackers and calorimeter modules. These trackers measure the tracks of the electron and positron that result when an incident γ-ray undergoes pair-conversion, preferentially in a thin, high-Z foil while the calorimeter estimates the energy of the subsequent electromagnetic shower. The entire LAT telescope is covered with an anti-coincidence detector, which is used to eliminate the background due to charged particles.

Each tracker module consists of 18 XY tracker planes and each XY plane has an array of silicon-strip tracking detectors (SSDs) for charged particle detection. These trackers reconstruct the arrival direction, and calorimeter which is located below these trackers estimate the energy of the γ-ray photons.

The *Fermi*-LAT's field of view covers about 20% of the sky at any time of observation. It operates in a survey mode in most of its observing time and scans continuously, covering the whole sky in every three hours. It covers the energy range from 20 MeV to greater than 300 GeV, with a field of view $\geq$ 2.5 sr.

The LAT point spread function (PSF), effective area and angular resolution are the functions of the incident photon's energy, inclination angle, and the event class. This effective area does not take the deadtime into account, and therefore the observed count rate is a product of the effective area, and incident photon flux with the livetime fraction. The PSF of LAT for an on-axis γ-ray has a 68% containment radius of 3° at 100 MeV and 0.04° at 100 GeV. The effective area in the center of the field of view is about 7000 cm^2 at 1 GeV and it decreases at lower and higher

energies. Details of *Fermi*-LAT performance can be found at website[1].

3.2.2 *Fermi*-LAT Data Analysis procedure

Fermi-LAT archival data can be obtained from NASA's website[2]. The *Fermi*-LAT data contains the list of photons and information about the spacecraft (SC) for a given time of observations. The event file contains the list of photons and other related information. The spacecraft file consists of information regarding the pointing direction, and position of the spacecraft in the orbit. This file also stores the live-time and the information regarding the time when the spacecraft passes the South Atlantic Anomaly (SSA). LAT does not collect data during the SSA to avoid high charge background. The LAT data server provides the photon (event) and spacecraft files for given time and energy bins.

The photon data is analyzed by *Fermi* ScienceTools (FST) package developed and provided by NASA. FST is an extension of the FTOOLS environment, which is a collection of utility programs used to analyze the contents of FITS data files that is obtained by space based instruments. These programs perform a single simple operation on fits file. The FTOOLS uses simple standardized subroutines to perform operations on the data.

The maximum likelihood optimization technique is used for detection, computing flux and obtaining spectral parameters from the *Fermi* γ-rays sources. This maximum likelihood optimization technique was introduced for the analysis of EGRET γ-ray data primarily.

Two types of likelihood analysis techniques, "binned" and "unbinned" are available to analyze the *Fermi*-LAT data. The unbinned analysis is recommended by *Fermi*-LAT collaboration for analyzing point sources, where the number of events in each time bin is expected to be small. However, binned analysis is preferred when the source is close to a very bright background region such as the Galactic

[1] http://www.slac.stanford.edu/exp/glast/groups/canda/lat_Performance.htm
[2] http://fermi.gsfc.nasa.gov/

plane. The binned and unbinned likelihood analysis are performed by the set of tasks provided with ScienceTools.

While modeling a *Fermi*-LAT source the influence of sources at large distance from target source will be greatly attenuated in LAT FOV, but it can not be neglected. To achieve greater accuracy, entire LAT sky needs to be modeled along with the main source, but due to computational and time constraints it is not feasible. A circular region of interest (ROI) was chosen around sources for event reconstruction. The ROI should be selected in such a way that it is several times the characteristic PSF size, in order to satisfy the restrictions of the likelihood package. Sources from a region larger than ROI can be included while modeling. This large region is called "Source Region". The "Source Region" is centered on the ROI, with a radius that is larger than the ROI radius by several PSF length scales. LAT PSF is energy dependent and it varies with energy. It is large ($\sim$3.5 degrees) at low energy ($\sim$100 MeV), and small ($<$0.15 degrees) at high energy ($\sim$10 GeV). An ROI with a radius of 10 degrees and a Source Region radius of 20 degrees would be appropriate while fitting a point source. A model file can be made which contains the best guess of the locations and spectral forms for all the sources in Source Region. This model file can be generated using "Modeleditor", a GUI-tool, or by running python scripts along with *Fermi* catalog for target source. These applications generate an XML file which contains all the information regarding all the sources present in ROI and Source Region from the *Fermi*-catalog [19].

A zenith-angle cut of 100° was applied to eliminate albedo γ-rays from the Earth's limb. In addition, time intervals were removed during which the observatory was transiting the South Atlantic Anomaly, or the rocking angle exceeded 52°. The spectral analysis on the resulting data set was carried out by including galactic diffuse emission component model and an isotropic background component model with post-launch instrumental response function.

To determine the significance of the sources, the likelihood-ratio test statistics is used, which is defined as,

Table 3.1: Details of background component model and post-launch instrumental response function versions used for *Fermi*-LAT analysis.

Source	Observation period	Galactic diffuse model	Extra galactic diffuse isotropic model	response function	data type
Mrk421	Feb. 2010	gll_iem_v02.fit	isotropic_iem_v02	P6V3 DIFFUSE	pass6
Mrk421	2011	gll_iem_v02.fit	iso_p7v6source	P7SOURCE_V6	pass7
Mrk501	2011	gll_iem_v02.fit	iso_p7v6source	P7SOURCE_V6	pass7

$$\mathrm{TS} = -2(\ln L_0 - \ln L), \tag{3.1}$$

where L_0 is the maximum likelihood value for the null hypothesis and L is the maximum likelihood with the additional source at a given position on the sky. The spatial parameters of the sources were kept fixed at the values given in the catalog, whereas the spectral parameters of the point sources in the ROI, along with the normalization of the diffuse components, were allowed to freely vary in the likelihood analysis.

The *Fermi* collaboration has recommended maximum likelihood analysis to compute flux and spectrum for point like sources. We have analyzed *Fermi*-LAT data of Mrk 421 and Mrk 501 using the standard analysis procedure *(ScienceTools)*. An unbinned likelihood analysis was performed for Mrk 421 and Mrk 501 by using Science tool and PYTHON scripts. All details of the used Galactic diffuse emission component model version, response function version, and data type used in analysis for each source are discussed in Table 3.1.

3.2.3 Unbinned Likelihood

This section provides a brief discription of all the *Fermi*-tasks used in unbinned likelihood analysis to obtain the flux and spectrum :

1. *gtselect* : The *gtselect* performs the user-specified cuts, such as cuts on position in sky, region of interest (ROI), selection of energy bin, time period of observations, and on maximum zenith angle value.

2. *gtmktime* : The *gtmktime* task computes Good Time Intervals (GTI) based on pointing and livetime history of the spacecraft. It also applies ROI-based zenith angle cut to exclude times where the region of interest is outside the field of view.

3. *gtbin* : A count map of ROI summed over photon energies can be created in order to identify candidate sources in the field using *gtbin* task. A count map of an AGN is shown in Figure 3.2.

4. *gtltcube* : As the LAT mostly operates in the survey mode, it makes an angle with the position in sky. The number of the events detected by LAT from a position of the sky or source depends on the amount of time that the source spent at a given inclination angle during an observation. The response function of the LAT also depends upon inclination angle between the observed position of the sky (source) and the LAT normal. The livetime is the time that the LAT observed a given position on the sky at a given inclination angle. Livetime cubes are calculated by the *gtltcube* task.

5. *gtexpmap* : The exposure map is defined as the total exposure for a given source in the sky in the ROI during observations. This is the product of effective area and time over which source is observed by LAT. The exposure map is calculated by the *gtexpmap* task. The exposure map is a function of photon energy and the response function.

6. *gtlike* : The likelihood statistic L is used to find the best fit model parameters between given input model and observed data. The input model contains the description of spectral forms, their positions, and intensities obtained from *Fermi*-catalog for all the sources present in source region.

   The *FERMI science tools* has five optimization algorithms to maximize the log likelihood function which are grouped into two classes. These optimizers

compute best fit spectral parameters and test statistics of the source. The co-ordinates of the source have been kept fixed while fitting spectral models.

The rule of thumb is to use "DRMNGB" class optimizer to maximize the likelihood and compute initial value of parameters and then use MINUIT class optimizers to find more accurate and final results. The optimizers determine the best-fit spectral parameters at given co-ordinates.

DRMNGB class optimizer finds the local minima of a continuously differentiable function subject to simple upper and lower bound constraints. It uses a variant of Newton's method, with a quasi-Newton Hessian updating method, and model-region technique to reach convergence.

"MINUIT" is a well known package from CERN which is used by *Fermi* Science Tools. All variables are treated as bounded and no user interaction is allowed in this class of optimizers. MIGRAD minimizing technique is implemented. This class of optimizer does not have limits on the number of free parameters.

The gtlike tool provides "result.dat" file which contains all the spectral parameters for all sources in ROI and a plot which shows the best fit models and the residuals. A plot of reconstructed events for all the sources is shown in Figure 3.3, the top panel shows counts/MeV vs MeV and bottom panel shows the residuals between model and the data. Here points are the data, and the lines are the models. Error bars on the points represent $\sqrt{(Nobs)}$ in that band, where Nobs is the observed number of counts. The black line is the sum of the models for all sources. Error bars here represent $(\sqrt{(Nopbs)})$/Npred, where Npred is the predicted number of counts in each band based on the fitted model.

3.3 *RXTE*: PCA and ASM

The Rossi X-ray Timing Explorer (*RXTE*) mission was the one of the most successful missions of NASA. It was launched on December 30, 1995 into a low-Earth orbit to

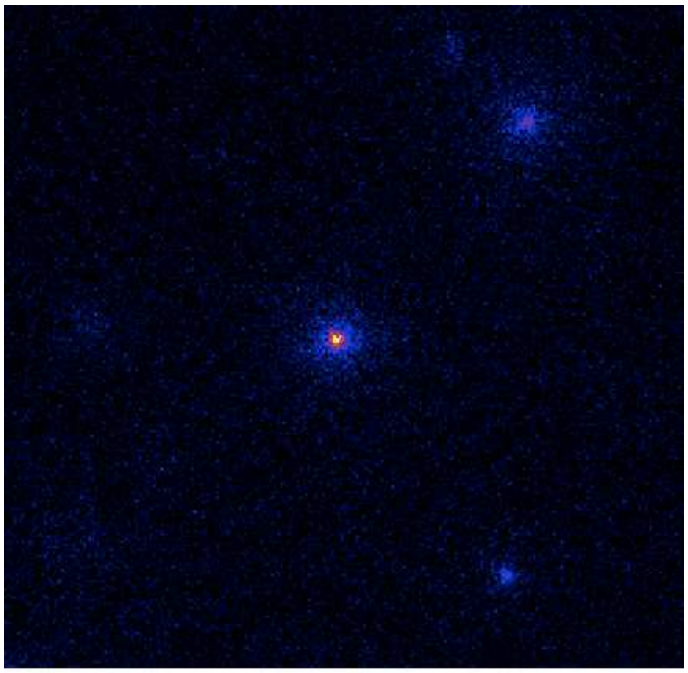

Figure 3.2: Counts map of an AGN integrated to entire energy band of *Fermi*-LAT

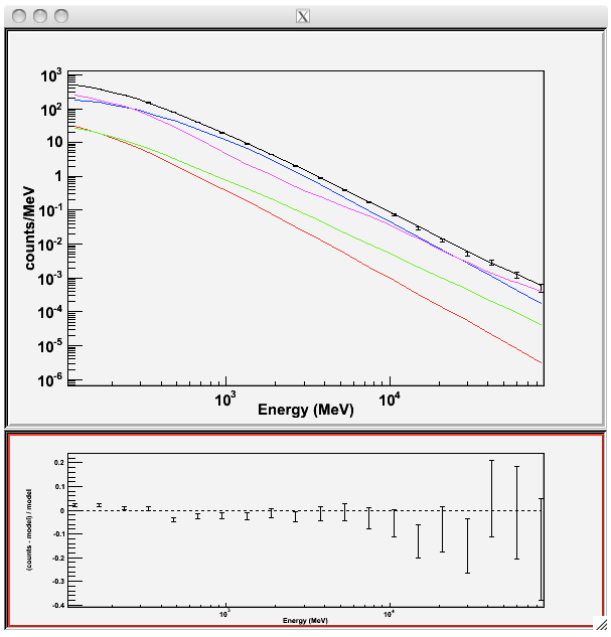

Figure 3.3: The points in above plot are the LAT data, and the lines are the best fitted models to the data

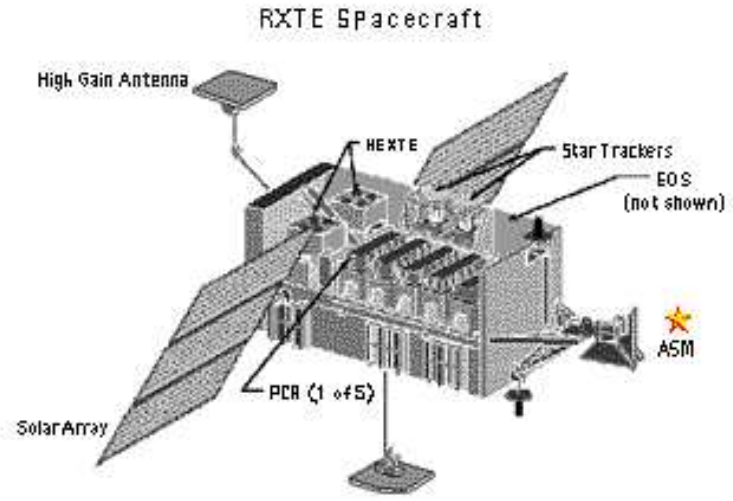

Figure 3.4: An image of *RXTE* satellite

facilitate the study of time variability, with a moderate spectral resolution, in the emission of X-ray sources. *RXTE* was decommissioned on January 5, 2012 after 16 years of incredible discoveries of extreme objects and environments in the universe.

Three instruments PCA, ASM and HEXTE were onboard the *RXTE* satellite, covering the energy range 2 - 250 keV. An image of the satellite is shown in Figure 3.4. The X-ray data from PCA and ASM are used for multiwaveband study of the selected TeV blazars. A brief discussion about the instruments and data analysis procedures are summarized here.

The Proportional Counters Array (PCA) [74] is an array of five identical xenon-filled proportional counter units (PCUs). The PCUs cover an energy range from $2-60$ keV with a total collecting area of 6500 cm^2. The archival X-ray data from PCA on board *RXTE* was analyzed to obtain the X-ray spectrum and light curve for selected TeV blazars.

We have analyzed standard 2 PCA data that have a time resolution of 16 sec-

onds with energy information in 128 channels. Data analysis was performed using FTOOLS (version 5.3.1) distributed as a part of HEASOFT (version 5.3). Data were filtered using the standard procedure given in the *RXTE* Cook Book 4 for each of the observations. The background models were generated with the tool "pcabackest", based on *RXTE* GOF calibration files.

The light curves of the sources in specified energy bin were obtained by running *seaxtrct* command on the data and background light curves were synthetically generated using *pcabackest* package by matching the background condition of the observations with those in various models files. An appropriate model was used to extract background for the light curve according to the source flux activity. *RXTE* website contains background models for both bright and faint flux state that can be used to obtain background light curves. The model "pca_bkgd_cmbbright_eMv20030330.mdl" is used for the bright flux state and the model "pca_bkgd_cmbfaint17_eMv20030330.mdl" is used for the faint state.

The PCA spectrum in the energy range of $3-30$ keV was fitted by using XSPEC. The pha file was generated by running *seaxtrct* command for source and background. A detector response matrix was obtained by running *pcarsp* task in FTOOLS to account for the response of the detector towards the X-ray photons of different energies.

The All Sky Monitor (ASM) onboard *RXTE* consists of three wide-angle shadow cameras equipped with position-sensitive Xenon proportional counters. These detectors have total collecting area of 90 cm^2 and they scan 80% of the sky in every 90 minutes. The energy range covered by ASM is 2-10 keV. The "Dwell" data from *RXTE*-ASM were obtained from the ASM website[3]. The usual selection cuts as prescribed by the ASM website were applied to "Dwell data". The ASM measurements also have a systematic error of 3% which is added in quadrature to the statistical errors. The weighted mean and weighted error are computed for the given bin size as flux and error on the flux. The details of the ASM data analysis method used is discussed in Chitnis et al. [75].

[3]http://xte.mit.edu/

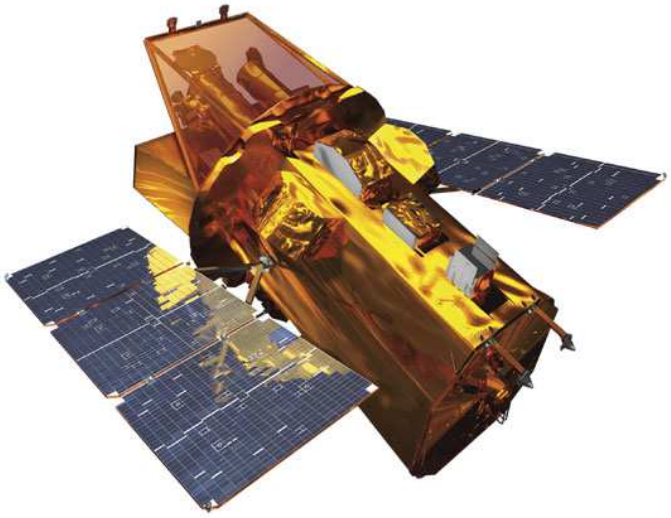

Figure 3.5: An image of *Swift* satellite, Figure taken from [76]

3.4 *Swift*: XRT and BAT

Swift is an X-Ray Telescope (XRT) designed to measure the fluxes, spectra, and light curves of X-ray sources in the 0.2 – 10 keV energy range.

The XRT onboard *Swift* satellite [77] uses a grazing incidence Wolter I telescope to focus X-rays onto a CCD. An image of *Swift* satellite is shown in Figure 3.5. The complete mirror module for the XRT consists of the X-ray mirrors, thermal baffle, a mirror collar, and an electron deflector. The CCD which is used in XRT, is located at the focal plane, and consists of an image area with 600×602 pixels (40×40 microns) and a storage region of 600×602 pixels (39 ×12 microns). The instrument has an effective area of 110 cm^2, 23.6×23.6 arcmin FOV, 15 arcsec resolution (half-power diameter), and an energy range of 0.2 – 10 keV. The FWHM energy resolution of the CCD decreases from ∼190 eV at 10 keV to ∼50 eV at 0.1 keV, where below ∼0.5 keV the effects of charge trapping and loss to surface states becomes significant. XRT operates in three observational modes imaging, timing, and photon-counting.

The windowed timing (WT) mode data were used to obtain the spectrum (0.3 –

3 keV) and light curve of the sources. Source photons were extracted using a box region with the length of 40 pixels and width about 20 pixels. Events with grades $0-2$ were selected for the WT mode data. The spectral data were rebinned by GRPPHA 3.0.0 with 20 photons per bin. Standard auxiliary response files and response matrices were used and spectra were fitted using XSPEC version 12.3.1.

Event files were calibrated and cleaned with standard filtering criteria with the *xrtpipeline* task using the latest calibration files available in the *Swift* CALDB. Average spectrum was extracted from the summed event file. The ancillary response files were generated with the *xrtmkarf* task applying corrections for the PSF losses and CCD defects using the cumulative exposure map. The latest response matrices (v.011) available in the *Swift* CALDB were used. A daily average flux between $15-50$ keV from *Swift*-BAT was obtained from BAT website[4].

3.5 Optical and Radio

3.5.1 Observations from Himalayan Chandra Telescope

Himalayan Chandra Telescope (HCT) is a 2 meter class optical telescope, installed at Indian Astronomical Observatory, Ladakh, India. HCT is remotely controlled and operated from the CREST campus of Indian Institute of Astrophysics, Bangalore via a dedicated satellite link. The HCT has Ritchey-Chretien (RC) optics with a f/9 beam at the cassegrain focus. The telescope is equipped with "Hanle Faint Object Spectrograph Camera (HFOSC)", which is an optical imager cum spectrograph. Only the central 2K×2k pixels of a 4K×4k cryogenically cooled SiTe CCD chip is used for imaging, which provides a FOV of 10×10 arcmin^2. Details of HCT telescope and HFOSC can be found here[5]. V band images of TeV blazar Mrk 501 were obtained to search for intra night optical variability (INOV).

[4]http://heasarc.nasa.gov/docs/swift/results/transients/
[5]http://www.iiap.res.in/iao_telescope

3.5.2 Data reduction

Data reduction of FITS files obtained by HCT was carried out using IRAF[6] software. Data reduction can be divided into two steps: (1) removing instrumental effects of CCD (preliminary processing) and (2) photometry of the cleaned source images.

Preliminary processing

Preliminary processing of the images, such as bias subtraction, flat fielding and cosmic ray removal were done through standard procedures in IRAF. The image with exposure of zero second represents the electronics background of the CCD. The sensitivity of the CCD is not uniform for all pixels across the chip and telescope also does not illuminate CCD homogeneously. These effects may cause some instrumental signatures on CCD such as spurious patterns on the CCD. The pixel-to-pixel sensitivity differences and electronic background needs to be corrected before measuring the flux of the source from CCD images.

Bias subtraction

The image with zero exposure is referred as bias image in CCD photometry and this is used to establish the pattern of readout noise across the chip. Several bias frames were taken without opening the shutter, with zero exposure, during the observation night. These bias images were averaged to create a master bias using *zerocombine* task in IRAF. This master bias frame is pixel-by-pixel subtracted from object and flat images.

[6]Image Reduction and Analysis Facility distributed by National Optical Astronomy Observatories (NOAO) in Tucson, Arizona

Flat fielding

The quantum efficiency of each pixel in the CCD is not necessarily the same. This pixel-to-pixel sensitivity variation has to be corrected before photometry. A flat field image can be obtained by exposing the CCD to a uniformly illuminated area, such as twilight sky. Several such flat images were obtained before and after the observations. These flat field frames were de-biased and then were combined using the task *flatcombine* in IRAF. The obtained flat frame was normalized by its mean. This normalized flat fielded image was used for flat fielding correction of source images.

Photometry

Photometry is a measurement of the flux that is emitted from the astronomical objects. All the source images were de-biased and flat fielded before the photometric measurements. The instrumental magnitudes of blazar Mrk 501 and field stars in the image frames were computed by aperture photometry, using DAOPHOT task of APPHOT package. This section explains the procedure used to obtained instrumental magnitudes of the sources.

Image center determination

Center of the sources in the CCD image were determined using centroid algorithm by *daofind* command of IRAF.

Choice of Aperture

Choosing an optimum aperture for photometry around the source is crucial for obtaining magnitude of the sources. In principal, the optimum aperture should be chosen in such a way that the noise from the background is minimized and signal from object is maximized and this aperture should contain almost all the light

from the source. A circular aperture is used for photometry around the source and comparison stars. The radius of optimum circular aperture was selected using curve of the growth method. In this method, source count vs radius of aperture is plotted. The total number of the counts from the object within the aperture grows initially but starts flattening after some radius and flux does not change more than 3% with radius. This aperture is considered as optimum aperture for photometry.

Background determination

Background determination is another crucial part of data reduction because the sky around the stars is not dark, but emits photons. The background value of sky was determined by taking an annulus of width of 5 to 10 pixels around the source using *Fitskypars*.

Differential photometry

Relative changes in brightness between target source and nearby comparison stars present in the telescope field are compared in differential photometry technique, rather than measuring absolute magnitude of a target source. Multiple reference stars can also be chosen and relative magnitudes are computed for the target source with respect to all reference stars. These relative measurements are made over time, and the differences are then plotted to study and illustrate the relative or differential change in magnitude. We have chosen three comparison stars in the field of Mrk 501. The intensity measurements of reference stars are used to correct the change in atmospheric effects and then target source is analyzed for flux variation.

3.5.3 Archival data

In addition to HCT data, optical V-band data obtained from Steward Observatory using SPOL instrument [78] and made available in the *Fermi* multiwavelength

support program websites[7] [8] are used.

The *Fermi* multiwavelength support program website also provided the 15 GHz radio fluxes of blazars obtained using the 40 meter single-dish telescope at Owens Valley Radio Observatory (OVRO) [79]. These fluxes are also used in this study.

[7] http://james.as.arizona.edu/p̃smith/Fermi/
[8] http://www.astro.caltech.edu/ovroblazars/index.php

Chapter 4

Multiwavelength Study of Mrk 421

4.1 Introduction

The blazar Mrk 421 ($z = 0.031$) is one of the brightest BL Lac objects in the northern sky at high energies. This source is the best studied blazar in VHE γ-rays. It was the first extragalactic source that was detected at γ-ray energies $E > 500$ GeV by the Whipple Observatory γ-ray telescope in 1992 [1]. Mrk 421 has also been detected with various other Atmospheric Cherenkov Telescopes (ACT) and air shower experiments [80, 81, 82, 71, 83, 84, 85], since its first detection. The spectral energy distribution (SED) of this object is dominated by non-thermal emission. The broadband emission (radio to γ-rays) in this source is produced in the jet which is oriented very close to the line of sight.

It is remains unclear whether the jet is composed of leptons or hadrons. The spectral energy distribution (SED) of blazars shows two humps. It is believed that the first hump is caused by synchrotron radiation from electron population gyrating in magnetic fields of jet. This radiation peaks at infrared to X-rays. The second hump peaks around GeV energies, and origin of this hump is not very clear. This hump may be produced by interaction of electrons with photon in leptonic models [2, 3, 4] or proton with photon field or magnetic field in the hadronic models [5, 6, 43].

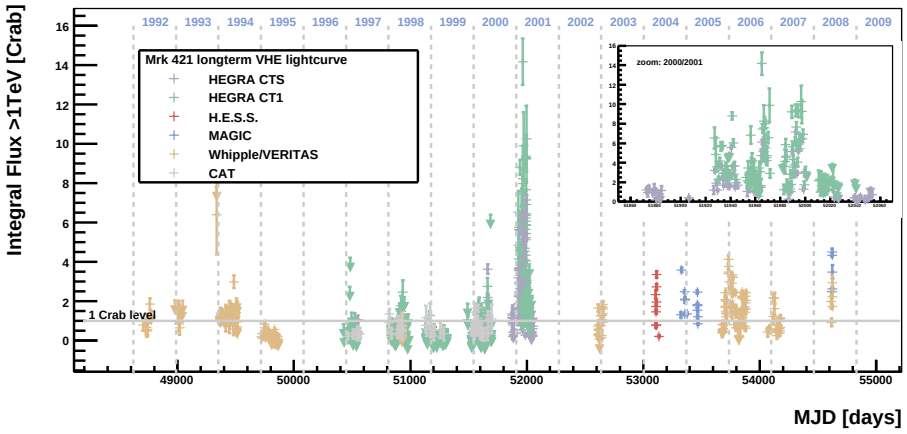

Figure 4.1: A historical light curve of Mrk 421, obtained from [98]

Mrk 421 is also highly variable over all time scales (minutes to years) and energy scales (radio to γ-rays). This makes it an ideal laboratory to study the environment of AGN jets. Even though the source has been studied since 1992, there are several unanswered questions. One of the main issues is how and where in the jet VHE γ-rays are produced, and whether jets are composed of electron-proton plasma or electron-positron plasma.

Mrk 421 has shown several high states of flux activity in X-rays and γ-rays over the past two decades [86, 87, 88, 89, 90, 91, 71, 92, 93, 94, 95, 96, 97]. It was observed in the brightest state of TeV γ-ray flux during the years 2000-2001, when its maximum flux reached as high as 14 Crab units above 1 TeV [98]. It has also shown several mildly high states since 2001, but was not found to be in an extremely high state till 2010. A historical light curve of Mrk 421 is shown in Figure 4.1, based on data obtained from DESY website[1].

In this Chapter, we study the multiwavelength behavior of Mrk 421 during its moderate and high state of activity during 2009-2011. A detailed multiwavelength study of a giant flare observed around 17 February 2010 is also presented. We have studied the evolution of its SED over a period of seven days (13-19 February

[1] http://astro.desy.de/gamma_astronomy/magic/projects/light_curve$_a$*rchive/index_eng.html*

Table 4.1: HAGAR results for Mrk421 during 2009-2011

Epoch -	Exposure Duration (Hrs.)	Excess -	Error -	Rate (/min)	Significance (σ)	Number of Pairs
2009 (March-May)	7.99	2095.0	516.94	4.36±1.07	4.05	14
2010 February	8.0	6418	503	13.4±1.05	12.7	12
2010 March-Apr	10.0	2938	579	4.9±0.97	5.1	15
2011 Jan-Apr	22.6	6313	878.7	4.9±0.64	7.5	34

2010) during this giant flare, based on data from HAGAR, *Fermi*-LAT, *RXTE*-PCA, *Swift*-XRT, SPOL and OVRO.

4.2 Multiwavelength observations and analysis

We have carried out a multiwaveband study of Mrk 421 to understand previously stated questions. The VHE γ-rays observations above 250 GeV were made using the HAGAR telescope during 2009-2011. The archival data from space borne instruments in X-ray (*SWIFT*, *RXTE*), HE γ-rays (*Fermi*-LAT), ground based optical (SPOL) and radio telescopes (OVRO) were combined to get a complete picture.

4.2.1 HAGAR Observations

TeV blazar Mrk 421 was observed using the HAGAR telescope during 2009 - 2011. The source was found in flaring and moderate activity state during the observations. Details of the flux states are provided in Table 4.1 where the first column shows the epoch of observations, second column shows the total exposure duration during that epoch, third and fourth columns are total excess and its corresponding errors, and the fifth column shows the rate of the observed γ-rays during that period. The sixth

column shows the significance of detection and the last column tells the number of the pairs, which are used to obtained the excess, rate, error and significance during that epoch. The data from HAGAR telescope were analyzed by the method discussed in § 2.7 and [99].

We analyzed only events with signals in at least five telescopes ($\geq$ five-fold) to reduce systematic errors in our data. The $\geq$ five-fold events correspond to an energy threshold of about 250 GeV. The main considerations for the data analysis were:

1. All seven telescopes should participate in the observations.

2. The mean zenith angle should be less than 20°.

3. There should be no fluctuation present in individual PMT or Royal Sum rates at the time of observations.

4. All spikes present in the runs are removed (This could cost a few minutes of exposure time).

4.2.2 *Fermi*-LAT data

Fermi-LAT data of Mrk 421 were obtained and analyzed using the standard analysis procedure *ScienceTools* provided by the *Fermi*-LAT collaboration. A circular region of 10° radius "region of interest (ROI)" was chosen around Mrk 421 for event reconstruction from the so-called "diffuse" event class data which has the maximum probability of being the source photons. Details of the analysis method can be found in § 3.2. A power law spectrum was used to model the source spectrum above 100 MeV. The flux, spectrum, and source location were determined by using unbinned maximum likelihood analysis using GTLIKE task of *ScienceTools*.

4.2.3 X-ray data from *RXTE* and *Swift*

The archival X-ray data from XRT onboard *Swift*, and PCA onboard *RXTE* were analyzed using FTOOLS (version 5.3.1) distributed as a part of HEASOFT (version 5.3) and XSPEC. The windowed timing (WT) mode data were used to obtain the spectrum in the (0.3 – 3 keV) range from *Swift*-XRT, and analyzed by the method discussed in §3.4. The PCA spectrum in the energy range of 3 – 30 keV was obtained by the method discussed in §3.3. The XRT and PCA spectra were fitted using XSPEC with a cutoff powerlaw with line-of-sight absorption. The line-of-sight absorption was fixed to the neutral hydrogen column density at 1.38×10^{20} cm^{-2} [100]. The "Dwell" data from *RXTE*-ASM were obtained from the ASM website[2] and were analyzed with the method discussed in [75]. A daily average flux between 15 – 50 keV from *Swift*-BAT was obtained from BAT website[3].

4.2.4 Optical and Radio data

The optical V-band observations from Steward Observatory and the 15 GHz radio observations from the OVRO are used in the study. These data are made available in the *Fermi* multiwavelength support program websites.

4.3 Giant flare during February 2010

Mrk 421 was reported to be in a high state of activity during November 2009 to April 2010, with flaring behavior in X-ray [101] and γ-ray bands detected in February, 2010. It was observed by the VERITAS collaboration in an extremely high flux state on February 17, 2010, who reported a maximum flux of 9 Crab units above 100 GeV [102], with an average flux of 4 Crab units. The HESS collaboration [103] also found this source in a high state during their follow-up observations. The results

[2] http://xte.mit.edu/
[3] http://heasarc.nasa.gov/docs/swift/results/transients/

from different experiments show rapid flux variation of minute to hour time scales in the VHE γ-rays during this bright outburst. We detected a giant flare on 17 February 2010 from HAGAR, a few hours after the VERITAS observations, with a maximum flux of 6 – 7 Crab units above 250 GeV (1 Crab unit $\sim$ 4.2 γ-rays/minute above 250 GeV). The source was detected with a 5 σ significance in less than 40 minutes of observations [99]. HAGAR continued the observations of Mrk 421 over the next two months. The average flux during February 2010 was found to be $\sim$ 3 Crab units and 1 Crab unit during March and April 2010 respectively.

The HAGAR observations were carried out for three months on moonless nights during February to April 2010 at a mean zenith angle of 6°. A total of 30 hours of data were collected during these observations. After imposing data quality cuts which are discussed in § 4.2.1, a total of 18 hours of observation was used for further analysis. The HAGAR observations during 13-19 February 2010 were divided into four states according to the flux level. All multiwavelength data were divided into these four states and average spectrum of each energy band obtained at each flux state. Table 4.2 provides the information on these flux states. We investigate in the following the multiwavelength behavior of Mrk421 during the flaring episode.

Figure 4.2 contains the daily light curve of Mrk 421 during February – April, 2010. The upper panel shows the daily average of VHE γ-ray flux obtained from HAGAR. The bottom panel shows the daily average from ASM onboard *RXTE* in 1.5 – 12 keV. It is clearly seen in the HAGAR as well as *RXTE*– ASM light curves that Mrk421 was in its brightest state in February 2010 in both VHE γ-rays and X-rays. The γ-ray and X-ray fluxes decreased in the later months, but were still higher than those during the quiescent state. Results of observations of Mrk 421 using HAGAR during the three months period are given in Table 4.3.

4.3.1 The high activity state : February 10 – 26, 2010

The multiwavelength (radio to γ-rays) quasi-simultaneous light curve of Mrk 421 during February 10 – 26, 2010 based on observations in § 4.2, is shown in Fig-

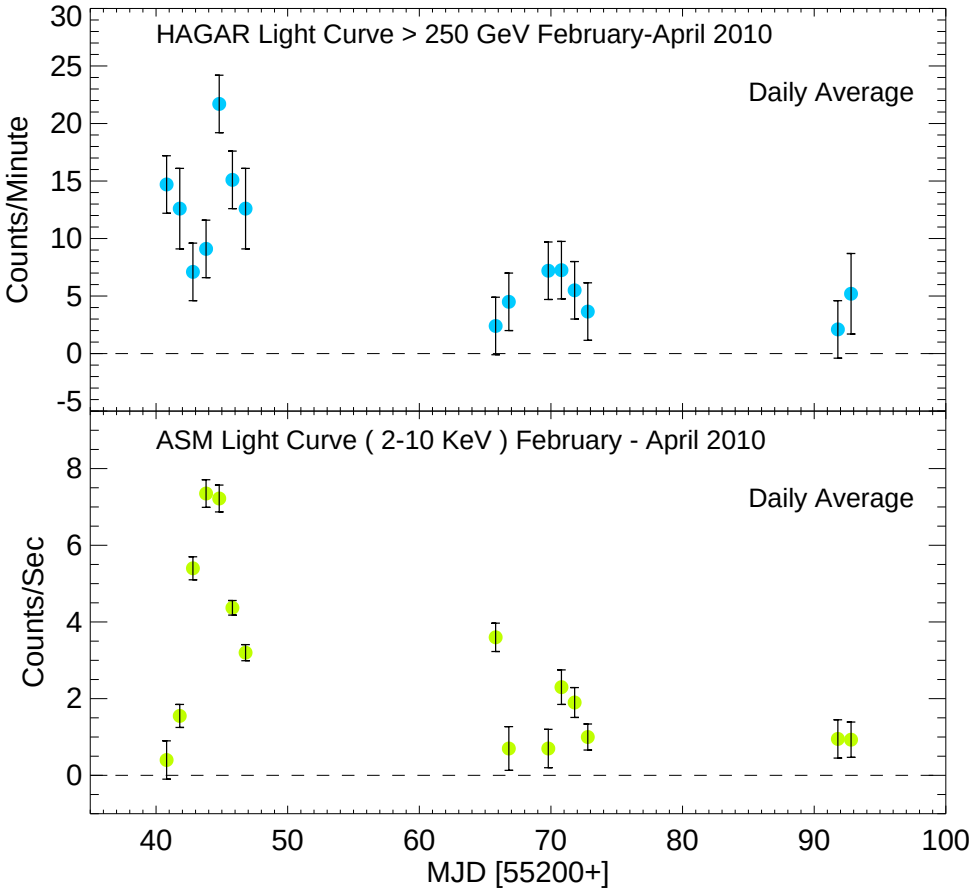

Figure 4.2: Top panel :Daily average light curve of Mrk421 during the period February – April, 2010 in VHE γ-rays above 250 GeV from HAGAR and the bottom panel shows the X-ray light curve in 1.5 – 12 kev from *RXTE*– ASM during the same period.

Table 4.2: Different activity states during February 13 – 19, 2010

State	Date	Duration (Days)
Pre Flare	13-15 February	3
Moderate Flare	16 February	1
TeV Flare	17 February	1
Post Flare	18-19 February	2

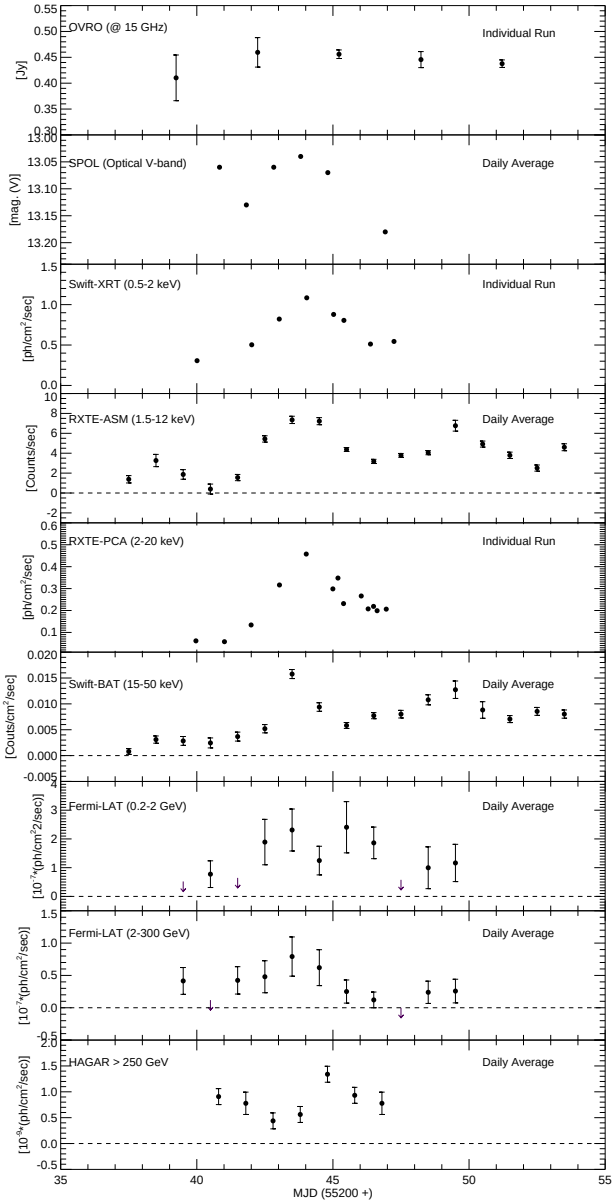

Figure 4.3: Multiwavelength light curve of Mrk421 during February 10 – 26, 2010

Table 4.3: HAGAR observations during the high state of activity

Month 2010	Total duration (min)	Excess number of on source events	Mean γ-ray rate (/min)	Significance σ
February	479	6418.22	13.4±1.05	12.7
March	478	2524.23	5.3±1.1	4.8
April	116	414	3.5±2.1	1.7

ure 4.3. The panels, in a descending order, correspond to data from OVRO, SPOL, *Swift*–XRT, *RXTE*–ASM, *RXTE*–PCA, *Swift*–BAT, *Fermi*-LAT (0.2 – 2 GeV), and *Fermi*-LAT (2 – 300 GeV). The bottom panel corresponds to HAGAR data above 250 GeV.

A clear variation of flux over a period of seven days (13-19 February 2010) is observed in the optical, X-rays, and γ-rays. The peak flux in optical, X-rays, and low-energy γ-rays is observed to be around February 16, 2010, while in the VHE γ-ray band, the peak is seen on February 17, 2010, with a possible one-day lag compared to the situation at lower energies. The radio flux has not changed significantly during this time.

The highest energy tail of the electron energy distribution is responsible for the production of the observed X-ray synchrotron continuum at $\geq$ 0.5 keV, while the TeV γ-rays might be produced through upscattering of synchrotron photons by the same population of electrons. The observed optical, and X-ray variability during February, 2010 may be explained by injection of fresh electrons in emission zone and cooling of the electrons due to SSC mechanism. The *Swift*–BAT light curve showed faster variability than *RXTE*–ASM, which could be due to the cooling effect of high-energy electrons, which produce X-rays at the 15 – 50 keV range.

The observed γ-ray variability is mainly divided into two bands, $<$ 2 GeV and above 2 GeV. The 0.2 – 2 GeV γ-rays observed by *Fermi*-LAT could be produced by low-energy electrons through IC scattering of UV synchrotron photons. *Fermi*-LAT detected a significant variation of flux in the 0.2 – 2 GeV band, observed over a period of eleven days during February 12 – 22, 2010.

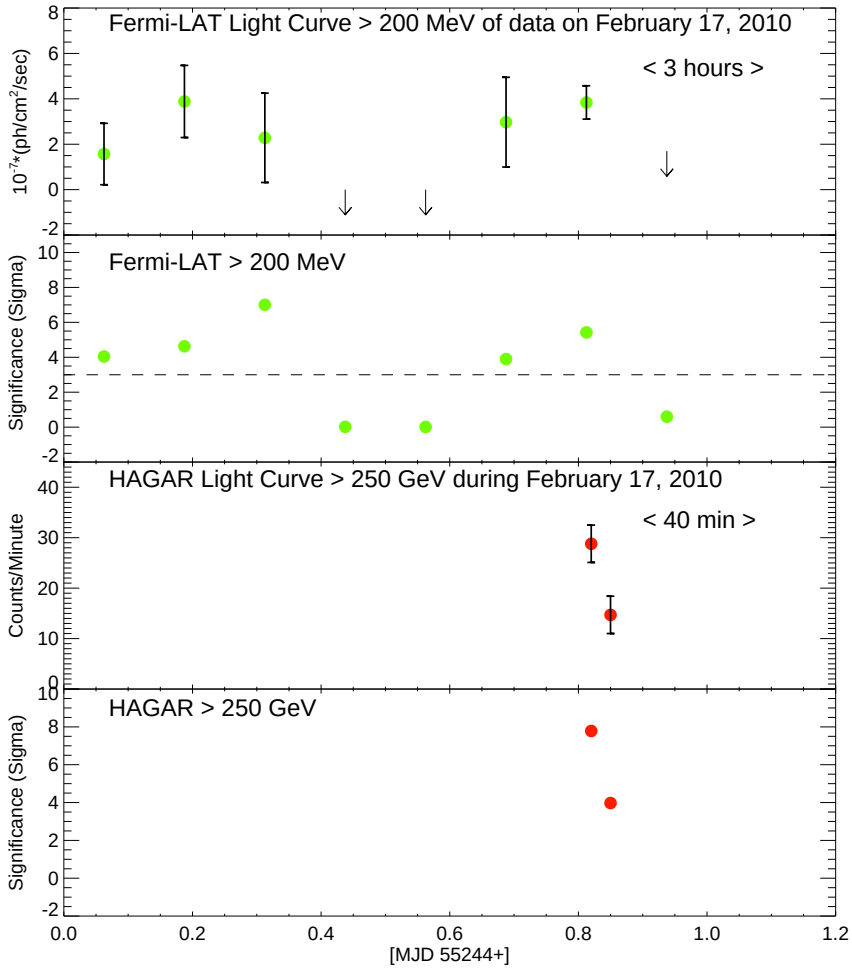

Figure 4.4: *Fermi*-LAT and HAGAR intra-day light curve of Mrk 421 during February 17, 2010.

The observed HE (>2 GeV) γ-rays by *Fermi*-LAT and VHE γ-rays by HAGAR could be produced by IC scattering of the electrons having a Lorentz factor in the range $\sim 10^4 - 10^5$. The observations from *Fermi*-LAT (2 – 300 GeV) show a symmetrical flare centered around February 16, 2010 but VHE γ-rays flux, observed by HAGAR reaches peak with a one-day lag on February 17, 2010. A fresh injection of high-energy electrons accelerated by shock could be responsible for the observed flare in γ-rays. If the SSC cooling time scale is shorter than the light-crossing time of the emission zone, the flare could be symmetric [104].

4.3.2 Intra-day and spectral variability.

Fermi-LAT data indicate an intra-day flux variability at energies > 200 MeV during the TeV flare on February 17, 2010. An increase in the flux is seen in the first 9 hours (MJD55244.0 – 55244.4) of LAT observations, followed by a quiescence that lasts for a few hours (MJD55244.4 – 55244.6) before the occurrence of another increase in flux during MJD55244.7 to MJD55244.85. A similar trend was detected by the VERITAS collaboration [102]. HAGAR also observed a continuous decrease in the flux over a period of $\sim$ 2 hrs (MJD55244.8 – 55244.86), which was simultaneous with *Fermi*-LAT during the later part of the night (see Figure 4.4).

Spectral variation was also detected over eleven days (February 12 – 22, 2010) of *Fermi*-LAT observations and seven days (February 13 – 19, 2010) of *RXTE*-PCA observations. A photon index of 1.39 ± 0.17, implying a flat/hard energy spectrum was observed in the *Fermi*-LAT data at energies above 100 MeV on February 17, 2010. On the other hand, maximum hardening in RXTE-PCA data was observed on February 16 (Figure 4.7 and Table 4.4). Spectral hardening in the X-rays [105] and γ-rays [81] during strong flares has been reported earlier also. The average folded spectra of Mrk 421 as observed from *RXTE*-PCA in energy band 3 – 20 keV during 13 – 19 February 2010 are provided in Figures 4.5 and 4.6. The first panel of the plots shows the folded spectrum and second panel shows the residuals of the fit to the data. The details of spectral index and cutoff value are given in Table 4.4.

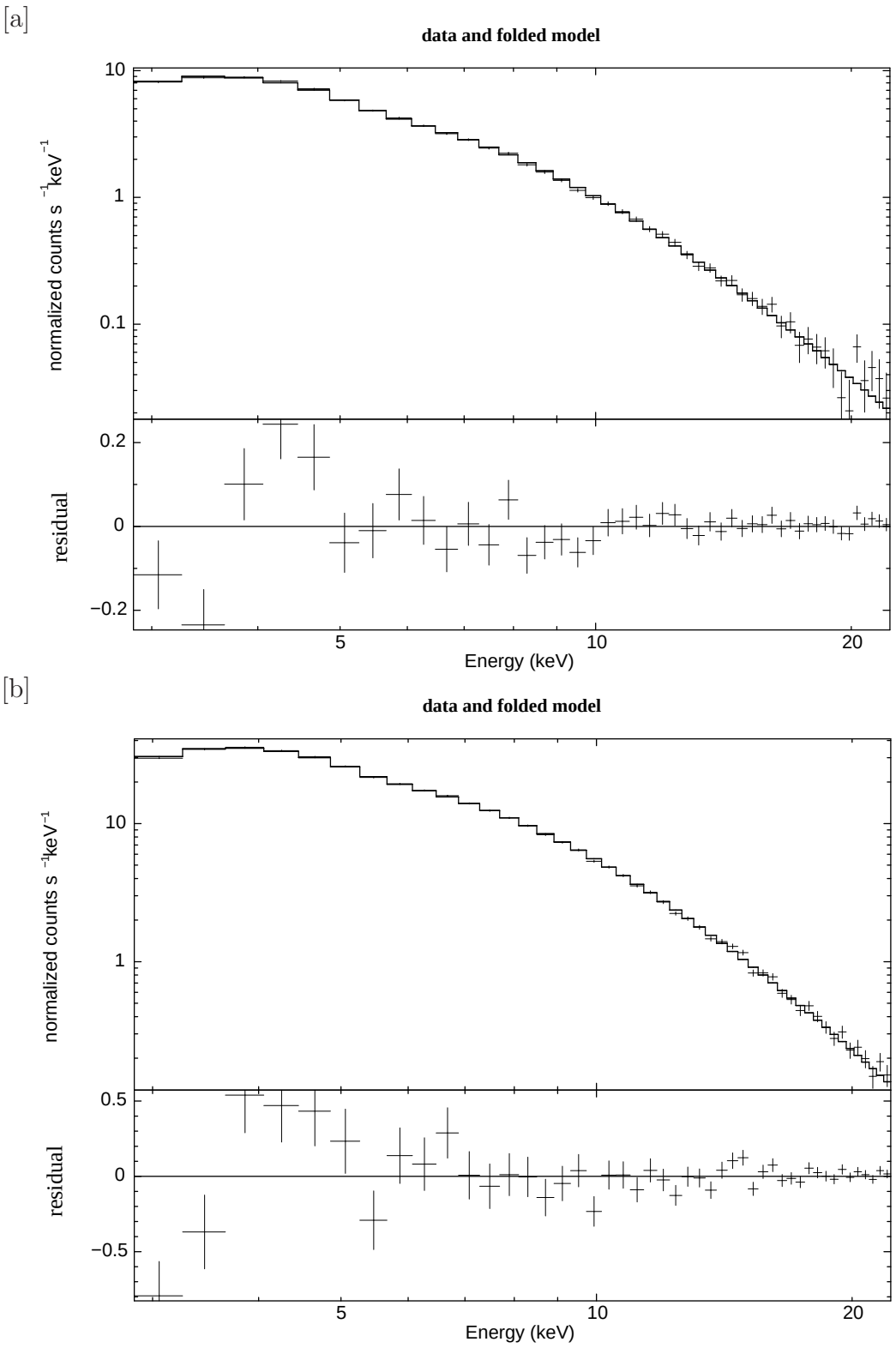

Figure 4.5: Folded spectra of Mrk 421 during 13-19 February 2010 Pre Flare [a], Moderate Flare [b].

[c]

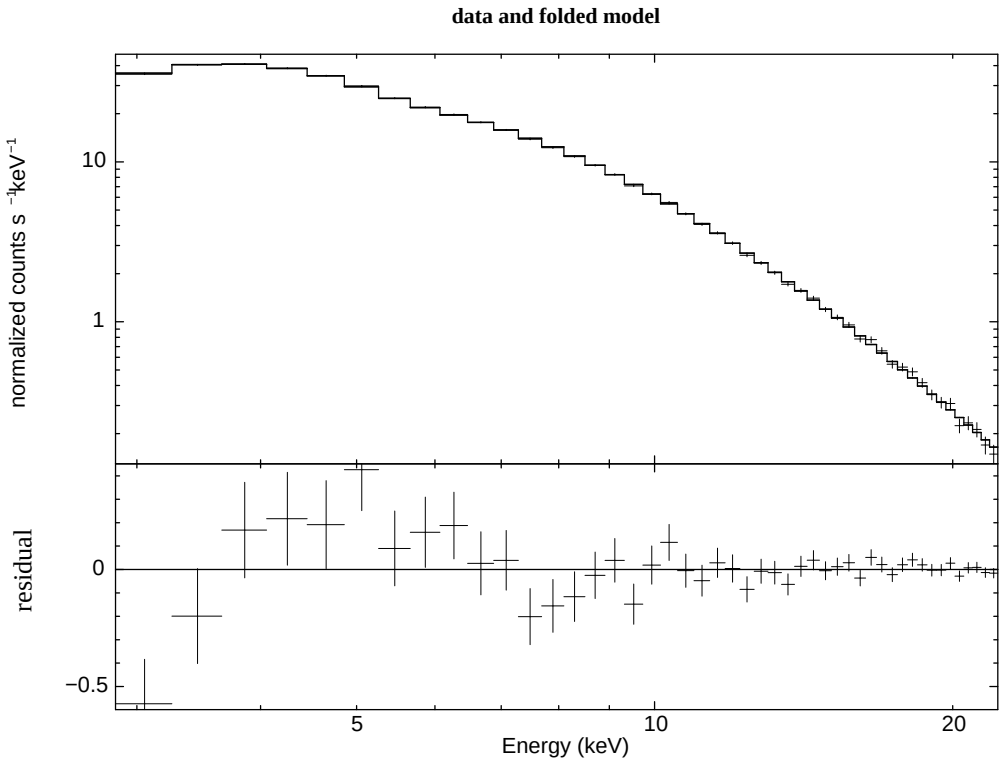

[d]

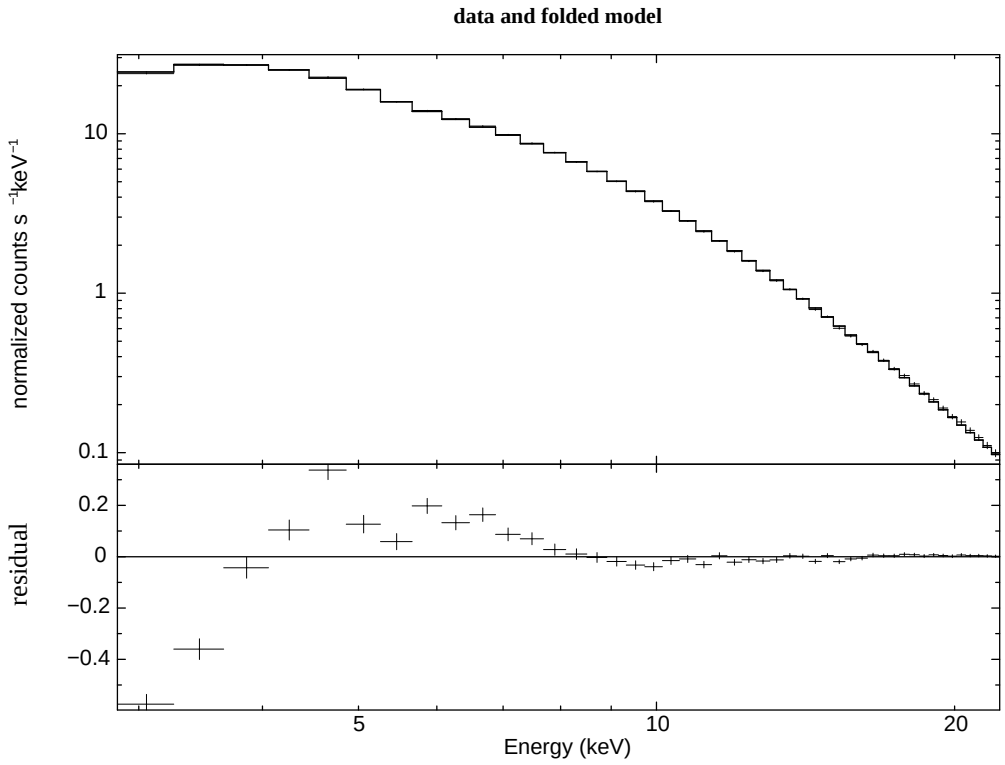

Figure 4.6: Folded spectra of Mrk 421 during 13-19 February 2010, TeV Flare [c] and Post Flare [d].

Table 4.4: Cutoff energy (PCA), spectral index (PCA) and photon index (*Fermi*-LAT >100 MeV) for four different activity states during February 13 – 19, 2010

State	**Cutoff PCA (keV)**	**Index PCA**	**Index LAT**
Pre Flare [a]	29.1±6.3	2.34±0.05	1.65±0.03
Moderate Flare [b]	19.5±1.5	1.91±0.03	1.67±0.15
TeV Flare [c]	26.8±2.2	2.03±0.02	1.39±0.16
Post Flare [d]	35.2±2.3	2.19±0.02	2.06±0.04

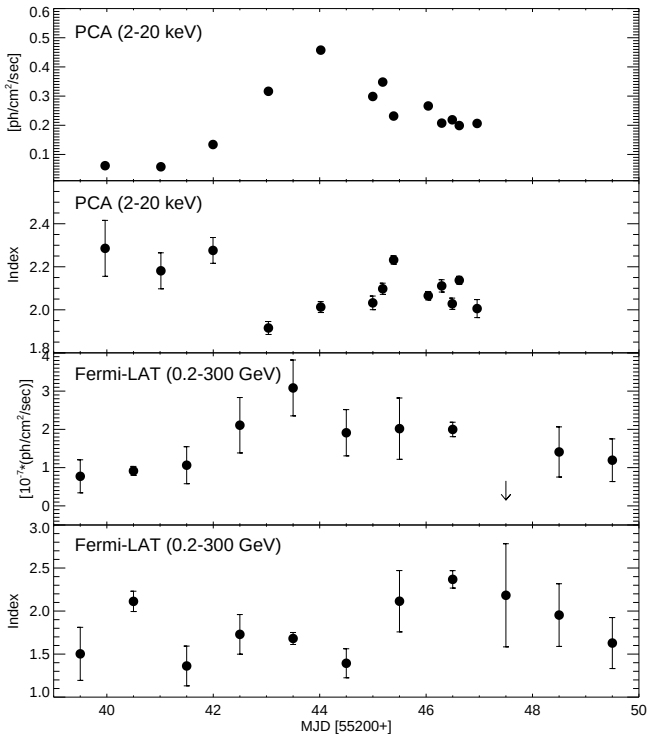

Figure 4.7: RXTE – PCA light curve and spectral index are plotted in the first two panels, *Fermi*-LAT light curve in the range 0.2 – 300 GeV and the photon index are plotted in the bottom two panels.

4.3.3 Cross-correlation study and time lag

From the X-ray and γ-ray light curves (Figures 4.2 and 4.3), we can see that the fluxes of Mrk 421 in these bands are roughly correlated. We investigated this correlation between X-ray and γ-ray bands using the cross-correlation function (CCF) and the z-transformed discrete correlation function (ZCDF) [106], a freely available FORTRAN 77 ZDCF code[4]. Observed lag and correlation coefficient between *RXTE*−ASM, *Swift*−BAT and HAGAR using CCF and ZDCF algorithms are listed in Table 4.5 for various cases. The time lag between X-ray and γ-ray emissions might impose constraints on emission region and could distinguish between SSC and external Compton (EC) models.

4.3.4 Spectral energy distribution

The spectral energy distribution of TeV blazars has a typical two-bump shape. It is often believed that the broadband emission from these sources is produced by a synchrotron self-Compton (SSC) mechanism. The lower energy bump, which peaks at infrared to X-ray is interpreted as synchrotron emission emitted by relativistic electrons gyrating in the magnetic field of the jet, and the GeV/TeV bump is attributed to IC scattering of synchrotron photons by the same population of electrons that produces the synchrotron radiation.

A one-zone homogeneous SSC model developed by Krawczynski et.al, [8] was used to fit the multiwavelength data to obtain the SED. This model assumes a spherical blob of plasma of a comoving radius R, which travels with a bulk Lorentz factor Γ towards the observer. The emission volume is filled with an isotropic population of electrons and a randomly oriented uniform magnetic field B. The energy spectrum of the injected electrons in the jet frame is described by a broken power law with low-energy ($E_{\rm min}$ to $E_{\rm b}$) and high-energy ($E_{\rm b}$ to $E_{\rm max}$) components with indices of $p1$ and $p2$. The emitted radiation is Doppler-boosted by the Doppler

[4]http://www.weizmann.ac.il/home/tal/zdcf2.html

factor

$$\delta = [\Gamma(1 - \beta\cos(\theta))]^{-1}, \tag{4.1}$$

where β is the bulk velocity of the plasma in units of the speed of light and θ the angle between jet axis and the line of sight in the observer frame. The observed luminosity of the source L_{obs} at a given frequency is related to the emitted luminosity L_{em} in the rest frame of the source via

$$L_{obs} = \delta^p L_{em}, \tag{4.2}$$

with p= 2 + α or 3 + α respectively in the case of a continuous jet or a moving isotropic source, here α being the spectral index. The VHE γ-ray spectrum is corrected for absorption by the extragalactic background light [107].

The radius of the emission zone is constrained by the variability time scales. Variability present in X-ray and γ-ray data is of the order of one day, so we have chosen $t_{VAR} \sim 1$ day. The comoving radius of the emission zone is defined as

$$R \sim c\delta t_{var}/(1+z). \tag{4.3}$$

We have obtained SEDs for different flux states using multiwavelength data of the Mrk421 during HAGAR observations of February 13 – 19, 2010 in an attempt to search for any changes in the physical parameters over this period [99]. The data are divided into four states according to the flux state of the source as follows: State 1: pre flare (13 – 15 February), State 2: moderate flare (16 February), State 3: TeV flare (17 February), and State 4: post flare (18 – 19 February). The pre flare state of the source is a moderately high state.

The *Fermi*-LAT data were divided into three bins (0.1 – 1 GeV, 1 – 3 GeV and 3 – 300 GeV) to obtain the spectrum of Mrk 421 for 'State 1', 'State 2' and 'State 4' by freezing the photon index to 1.65, 1.67 and 2.06 respectively. These photon indices were obtained by analyzing the 0.1 – 300 GeV data from *Fermi*-LAT. The *Fermi*-LAT spectrum of February 17, 2010 was obtained by dividing *Fermi*-LAT

Table 4.5: Correlation coefficient and time lag of Mrk421 emission during February – April, 2010

Instruments	**Lag (Days)**	**Correlation coefficient**	**Algorithm**	**Data Used 2010**
RXTE–ASM vs *Swift*–BAT	0.0	0.81	CCF	13 – 19 February
RXTE–ASM vs *Swift*–BAT	0.0	0.77	ZDCF	10 – 27 February
RXTE–ASM vs HAGAR	1.3	0.62	ZDCF	February to April
Swift–BAT vs HAGAR	1.3	0.88	CCF	13 – 19 February
Swift–BAT vs HAGAR	1.3	0.82	ZDCF	13 – 19 February
Swift–BAT vs HAGAR	1.3	0.74	ZDCF	February to April

data into four bins (0.1 – 1 GeV, 1 – 3 GeV, 3 – 10 GeV and 10 – 300 GeV) by freezing the photon index to 1.39, obtained by the analysis of the 0.1 – 300 GeV data. The best-fit photon indices and cutoff energies for all four states are presented in Table 4.4.

The magnetic field, Doppler factor ($\Gamma \sim \delta$), electron energy density, break present in electron injection spectrum ($E_{\rm b}$), $p1$, $p2$, minimum and maximum electron energies were used as free parameters while fitting the model to optical, X-ray, and γ-ray data. The angle between the jet axis and the line of sight in the observer frame was taken to be 2.6°.

4.3.5 Evolution of the SED during the high state

The *Fermi*-LAT collaboration [108] had reported the photon index of the energy spectrum of Mrk 421 to be 1.78 from the first 5.5 months of their observations. This refers to an average spectrum mostly during the quiescent state. However, during 'State 1' (see Figure 4.8 (a)), we find the energy spectrum to be flatter with a photon index of 1.65 at 0.1 – 300 GeV energies. Also, we see a plateau in the light curves during this state in the 2 – 300 GeV energy and 15 – 50 keV energy ranges (see Figure 4.3). The presence of a plateau in the light curve indicates that the injection time scales of energetic electrons are longer than the cooling time scales,

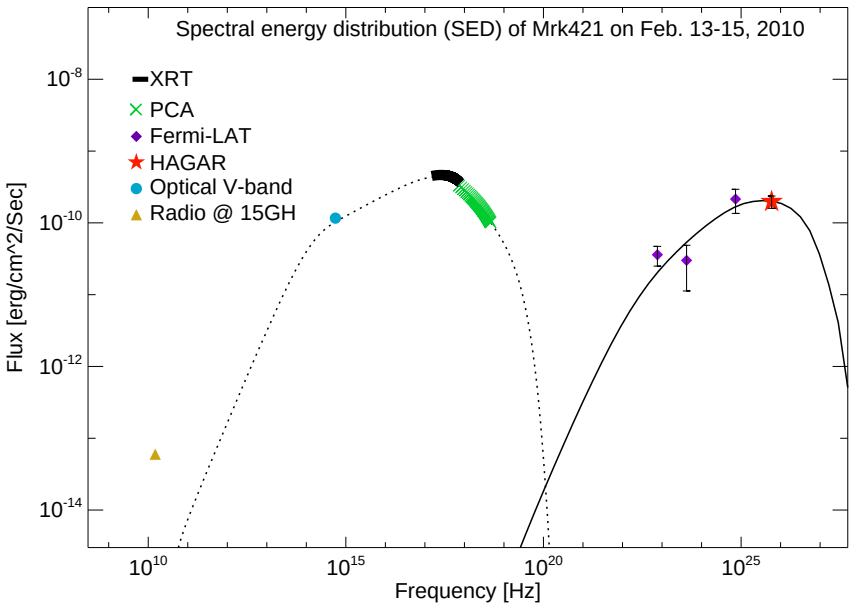

[a]

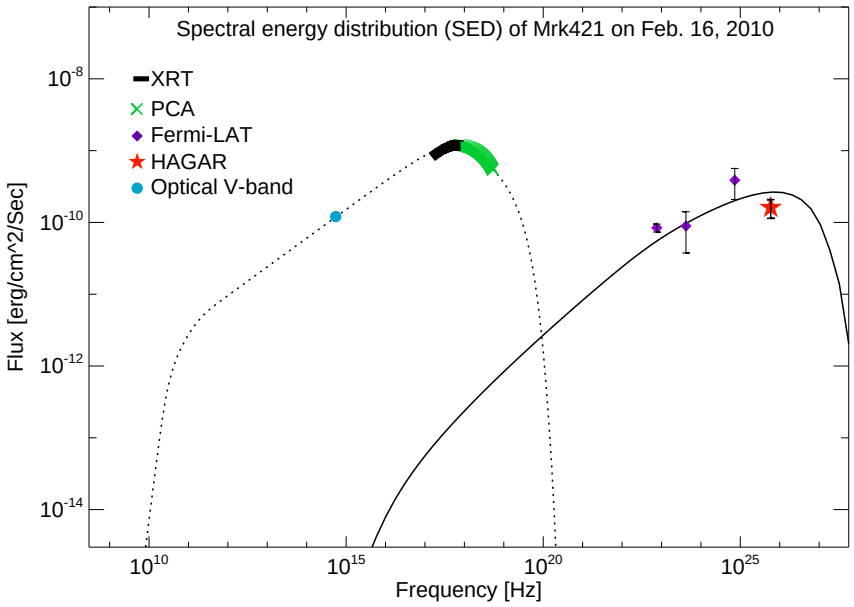

[b]

Figure 4.8: SEDs of Mrk 421 during February 2010, obtained from Figure [a] Pre-flare 13-15 February 2010, [b] low and HE γ-ray flares on 16 February 2010 [99]

.

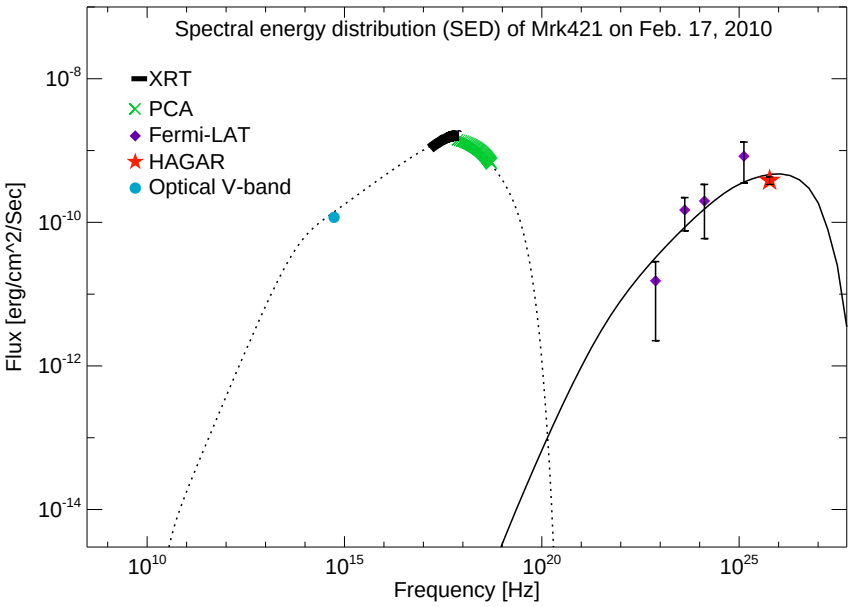

[a]

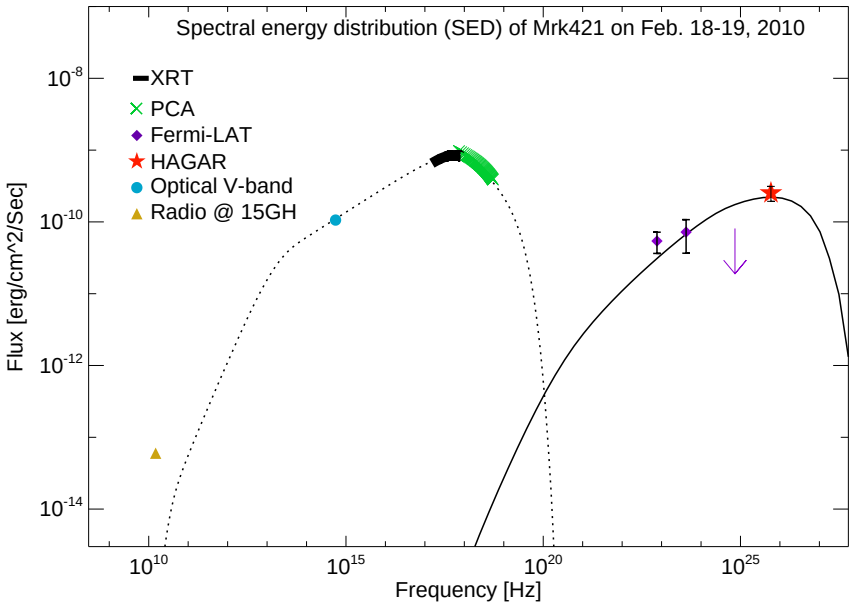

[b]

Figure 4.9: SEDs of Mrk 421 during February 2010, obtained from [c] TeV flare on 18 February 2010, [d] Post flare 18-19 February 2010 [99]

.

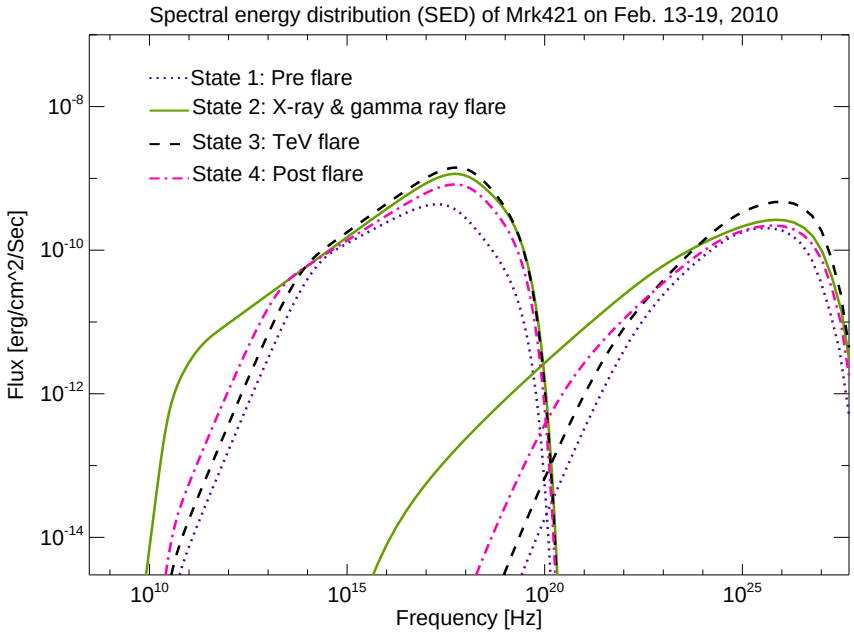

Figure 4.10: SEDs of Mrk 421 during February 2010, obtained from [99]

.

and the entire volume of emission zone is radiating. Plateaux are also observed in other γ-ray sources like 3C 454.3 [109].

Flares in optical, X-ray, low-energy (<2 GeV) γ-ray, and HE (2 – 300 GeV) γ-ray bands were seen in 'State 2'. The corresponding SED is shown in Figure 4.8 (b). These low and HE γ-ray flares could be caused by upscattering of X-ray photons by low-energy electrons that are produced by SSC cooling in 'State 1'. As an effect of the low-energy flare, the low-energy part of SED in 'State 2' is much flatter than that in 'State 1'.

The observed GeV/TeV flares above 250 GeV on 17 February could be produced by upscattering of X-ray photons in *Swift*–BAT energy range by higher energy electrons (see Figure 4.9 (a) for the SED). The presence of a passing shock might have accelerated the electrons to higher energies in the emission region.

The source is brighter at lower energy γ-ray in 'State 4', which could be due to

cooling of electrons after the high-energy flare. The corresponding SED is shown in the Figure 4.9 (b).

The derived SED parameters for each state are listed in Table 4.6, and in Figure 4.10 we illustrate the change that SED undergoes during the four different states of the source.

4.3.6 Discussion

We found satisfactory fits for all four states with the one-zone SSC model described in §4.3.4 . The observed pre-to post-flare evolution of the SED and light curve are explained by the model. Changes in the physical conditions such as Doppler factor and magnetic field during these observations are indicated by modeling of the multiwavelength data. It appears that changes in these parameters are related to the activity of the source. The change in jet flow from 'State 1' to 'State 2' may lead to a shock in the jet. We also found small changes in the particle energy density and the magnetic field strength from 'State 1' to 'State 2'. The best fits obtained by fitting multiwavelength data to the SSC model during the rising part of the flare ('State 2' and 'State 3') are found for a power law index of the electron injection spectrum before break of $p1 = 2.2$. Because $p1 = 2.2$ is a result of the Fermi first order mechanism, it strengthens the belief that a strong shock might have accelerated the electrons in the emission zone and caused the flare by SSC mechanism. Very recently, Abdo et al. [7] showed that electrons present in the emission zone of Mrk421 might be accelerated by a Fermi first-order mechanism at the shock front. The best-fit parameters from the modeling of the SED using multiwavelength data for 'State 1' indicate that an aged population of electrons with $p1 = 2.4$ was present in the emission zone. The light curve during the same period suggests that the entire volume of the emission zone was radiating. The observed change in the electron injection spectrum $p1 = 2.3$ during the decaying part of the flare might be considered to be a result of SSC cooling mechanism.

The observed break in the electron injection spectrum could also be explained

Table 4.6: SED parameters obtained by fitting to data using $t_{var} \sim 1$ day

State	Magnetic	Doppler	log E_{min}a	log E_{max}b	E_{break}c	p1	p2	Sy_{pk}d	IC_{pk}e	U_ef	ηg
-	field	factor	[eV]	[eV]	[eV]		-	[10^{17}]	[10^{25}]	[10^{-3}]	[$u_e^{'}/u_B^{'}$]
-	(G)	(δ)	-	-	-	-		(Hz)	(Hz)	(erg/cc)	-
State1	0.026	19.5	9.6	12.1	11.3	2.4	4.3	1.93	3.58	0.9	33.46
State2	0.029	22.0	8.0	12.1	11.40	2.2	3.9	5.74	7.02	1.4	41.83
State3	0.029	21.0	9.4	12.1	11.45	2.2	4.1	6.13	11.53	1.0	29.88
State4	0.028	21.0	9.1	12.1	11.45	2.3	4.1	5.53	6.76	0.85	27.24

(a)→E_{min}: Minimum value of energy of the electrons present in the emission zone
(b)→E_{max}:Maximum value of energy of the electron present in the emission zone
(c)→E_{break}: Break in the electron injection spectrum
(d)→Sy_{pk}:Peak value of synchrotron bump
(e)→IC_{pk}:Peak value of IC bump
(f)→U_e:Electron energy density
(g)→η:Equipartition coefficient

as a cooling break, where the escape time of an electron of Lorentz factor γ_c, equals the radiative cooling time. It is observed from our results that the cooling break changes with the state of the source. We have also found that both SED peaks move toward higher energy as the source flux increases, and return to lower energies as it decreases. Spectral hardening is also observed at X-rays and γ-rays at the time of the flare (high state) (see Figure 4.7, Table 4.4). A departure from equipartition is also observed during this high state. The emission process at the time of high activity is more complex than in the quiescent state. Energy-dependent variability observed from *Fermi*-LAT has shown that the source is much more complex than anticipated. The emission from Mrk 421 also showed an intra-day variability on 17 February 2010, in γ-ray bands above 0.2 GeV in *Fermi*-LAT data and >250 GeV from HAGAR data. We could not significantly detect this sub-hour-scale variability from *Fermi*-LAT owing to the large error bars. The detection of sub-hour variability from Fermi-LAT and HAGAR could constrain the size of the emission region. The present results of correlation studies between X-ray and γ-ray flux variability are not conclusive enough to distinguish between the one-zone SSC or EC model. However, the observed hardening of the emission spectra obtained from *Fermi*-LAT and *RXTE*−PCA data with a one-day lag (see Figure 4.7 and Table 4.4) is inconsistent with the SSC model and opens up the possibility of multizone-SSC or EC models.

4.4 Moderate activity state

HAGAR observations since 2009 have detected Mrk 421 in several moderate activity states. One such state was observed in March 2011, and a multiwaveband study was under taken to understand the physical properties of the source during this active phase.

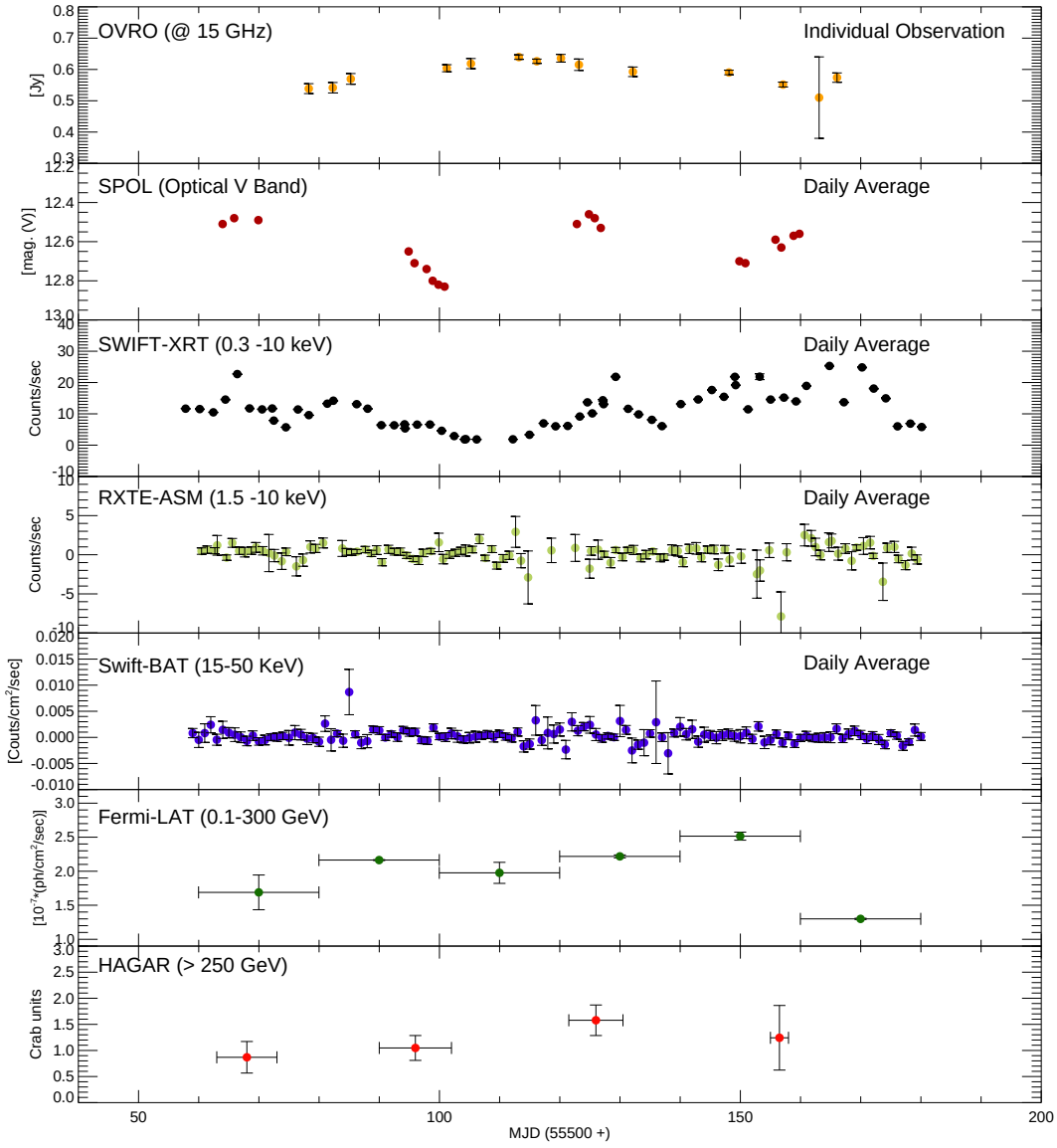

Figure 4.11: Multiwavelength light curve of Mrk 421 during January -April 2011. The top six panels correspond to data from OVRO, SPOL, *Swift*–XRT, *RXTE*–ASM, *RXTE*–PCA, *Swift*–BAT and *Fermi*-LAT (0.2 – 300 GeV) respectively. The bottom panel corresponds to HAGAR data above 250 GeV.

4.4.1 Flux variability during moderate activity state

We have studied Mrk 421 for four months (January-April) during the year 2011 using HAGAR and other space and ground based instruments. The multiwaveband light curve during this epoch is shown in Figure 4.11. The source was found in moderate activity state with the maximum flux in VHE γ-rays seen in the month of March 2011. The flux had reached close to 1.5 Crab units at energy >250 GeV (HAGAR observations). The peak flux in optical V-band by SPOL and X-ray band by XRT is also observed during this period. The peak flux in *Fermi*-LAT data was however observed about twenty days after the peak in VHE γ-rays. The radio flux as observed by OVRO at 15 GHz shows small variability during these four months and peak flux is observed during March. We were not able to detect any variability in X-ray flux from *RXTE*– ASM and *Swift*– BAT instruments due to their low sensitivity. The HE and VHE γ-ray flux observed by *Fermi*-LAT and HAGAR in this state can be ascribed to the SSC mechanism. These γ-rays can be produced by IC scattering of X-rays photons of energy 0.3 – 10 keV by an electron population which produces X-rays via synchrotron emission.

4.4.2 Spectrum and SED during moderate activity state

A cutoff powerlaw was used to fit the XRT and PCA spectrum in the energy band of 0.5-20 keV. The combined spectral fit of XRT and PCA indicates a spectral index of 2.37 with cutoff energy at 8.3 keV. A powerlaw function was fitted to the *Fermi*-LAT data during this moderate active state in the energy range of 0.1 – 300 GeV. Photon index during this period was found to be 1.76 $\pm$0.05, using the maximum likelihood analysis method. The emission mechanisms and physical parameters of Mrk 421 during this moderate activity state are modeled by broadband SED modeling using single zone SSC model, discussed in § 4.3.4. A satisfactory fit to optical, X-ray and γ-ray data is obtained, and shown in Figure 4.12.

The variability time scale is assumed to be t_{var} $\sim$1 day for modeling the data.

Table 4.7: SED parameters obtained by fitting to data using $t_{var}\sim$ 1 day moderate state March 2011

State	Magnetic	Doppler	log E_{min}a	log E_{max}b	E_{break}c	p1	p2	Sy_{pk}d	IC_{pk}e	U_ef	ηg
-	field	factor	[eV]	[eV]	[eV]		-	[10^{17}]	[10^{25}]	[10^{-3}]	[$u_e^{'}/u_B^{'}$]
-	(G)	(δ)	-	-	-	-		(Hz)	(Hz)	(erg/cc)	-
State1	0.035	22.9	9.45	11.6	10.5	2.3	3.9	0.11	0.8	0.7	14

(a)→E_{min}: Minimum value of energy of the electrons present in the emission zone
(b)→E_{max}:Maximum value of energy of the electron present in the emission zone
(c)→E_{break}: Break in the electron injection spectrum
(d)→Sy_{pk}:Peak value of synchrotron bump
(e)→IC_{pk}:Peak value of IC bump
(f)→U_e:Electron energy density
(g)→η:Equipartition coefficient

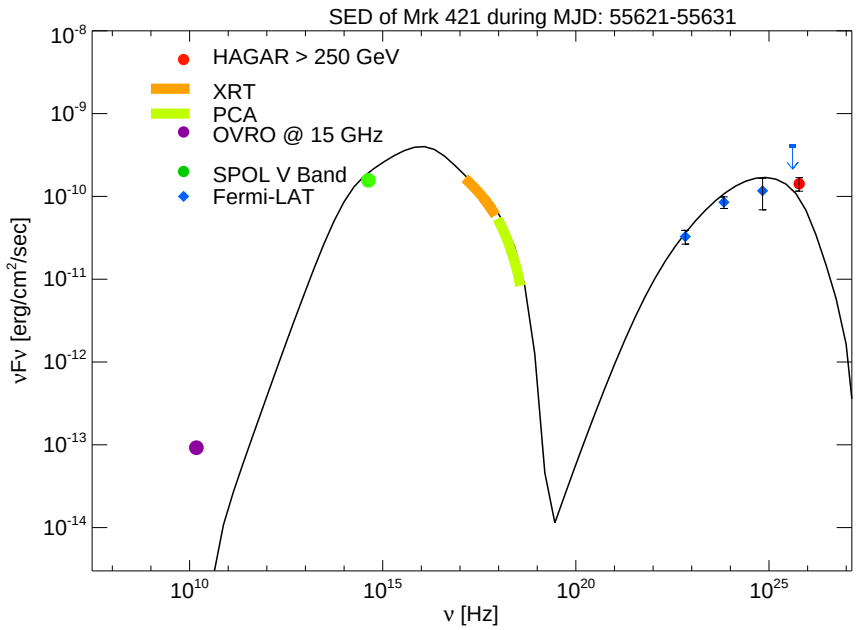

Figure 4.12: Multiwavelength SED of Mrk 421 during March 2011

All parameters deduced from the model are provided in Table 4.7.

A relatively high magnetic field is indicated during this state compared to the high state which was observed during February 2010. The obtained value of magnetic field of 0.035 G during this moderate state is in good agreement with the study made by Abdo et al. during a similar state, with an estimated value of 0.038 G [7]. No significant change is observed in Doppler factor values from high state to moderate state. The electron population gets accelerated to relatively low energies in moderate state compared to that in high state. It is clear from the results of moderate state that the cooling break is dependent on activity of the source. It is observed that the break in the electron spectrum appears at lower energies in the low flux states and at higher energies at high flux states. It is also found that both SED peaks move toward lower energies as the source flux decreases in moderate activity state compared to that in high state. Equipartition was not observed even in moderate activity state.

4.5 Summary

Mrk 421 is the one of best studied TeV blazars over the entire electromagnetic spectrum. Nonetheless, several issues such as origin of its short and long term variability, jet content, VHE γ-ray production mechanism, physical parameters of emission zone and energy dissipation zone are still highly debatable. One of the main reasons in our lack of understanding was the un-availability of high quality long term simultaneous multiwavelength data. Several multiwavelength campaigns have been organized by MAGIC, VERITAS and *Fermi* collaborations in the recent years, which provided very high quality data over the entire electromagnetic spectrum. The recent studies by MAGIC, *FERMI*, VERITAS and HAGAR collaboration have made the picture some what clear. The results from these MW studies suggest that the broadband SED of Mrk 421 is produced by SSC mechanism. These studies also suggest that the emission zone of Mrk 421 is filled with a uniform magnetic field of ~ 0.035 G and an electron population that is accelerated at the shock fronts in the jet. This emitting zone moves in the forward direction with a Doppler factor ~ 23 in the jet (this work, [7]). The broadband SED of Mrk 421 has also been modeled with low Doppler factor of $\sim$10 and high magnetic field of ~ 0.4G during a state of moderate activity [91].

Chapter 5

Multiwavelength Study of Mrk 501 & its rapid variability

5.1 Introduction

Mrk 501 (z=0.034) is the second extragalactic TeV source that was detected above 500 GeV by the Whipple observatory in 1996 [110]. Mrk 501 belongs to a sub-class of AGN that are known as high-energy peaked blazars (HBL). The broadband emission (radio to γ-rays) in these sources are produced in the jet that is oriented very close to the line of sight. The composition of these jets are not known, it is not very clear whether these are made of electron-positron plasma or electron-proton plasma. The spectral energy distribution (SED) of Mrk 501 characteristically shows a double-peaked profile. These peaks occur at keV and GeV/TeV energies when the SED is plotted in the νF_ν versus ν representation. It is believed that the first hump of the SED is caused by synchrotron radiation from the electron population gyrating in magnetic fields of the jet, but the origin of the GeV/TeV hump is unclear. This hump may be produced by interaction of electrons with photons in leptonic models [2, 3, 4] or protons with photon fields or magnetic fields in hadronic models [5, 6, 43].

Mrk 501 is also known for its major, long timescale and short timescale flares in X-rays and VHE γ-rays [111, 112, 113, 114]. One of its historical outburst was observed in 1997 when the flux at energies above 1 TeV reached upto 10 Crab [115, 116]. Following this outburst, the average flux of Mrk 501 dropped to 0.3 Crab during 1998-1999 [117]. Rapid, and intra-night variability have been displayed by Mrk 501 over the entire electromagnetic spectrum [118, 119, 114].

In this chapter, HAGAR observations of Mrk 501 are discussed. Following this, a detailed multiwavelength study of Mrk 501 during 2011 using ground and space based instruments from radio to γ-rays are presented. Fermi-LAT spectra of the Mrk 501 in different flux states during 2011 have been compared. Constraints on physical parameters of the Mrk 501 obtained by fitting one zone SSC model to multiwaveband data are also discussed.

Finally, a viable explanation for the observed very fast TeV variability in Mrk 501 as observed by the MAGIC telescope is presented.

5.2 Multiwavelength observations and analysis

VHE γ-rays and Optical observations were made using HAGAR and HCT telescopes, respectively, from Hanle. In addition, archival data from *Fermi*-LAT, *RXTE*-PCA, *SWIFT*-XRT, *SWIFT*-UVOT, *SWIFT*-BAT, SPOL and OVRO were analyzed using methods discussed in Chapter 3, to obtain light curves and SEDs.

5.2.1 HAGAR

Observations of Mrk 501 were made using HAGAR telescope during March-May 2010 and March-June 2011 on moon-less, clear nights. Details of observation are provided in Table 5.1. The data were analyzed according to the procedure discussed in [99] and § 2.7. Only events with signals in at least five telescopes ($\geq$ five-fold) were analyzed to reduce systematic errors, which corresponds to an energy threshold

Table 5.1: HAGAR observations of Mrk 501 in 2010 and 2011

Epoch	Total duration (Pairs) (min)	Excess number of on source events	Mean γ-ray rate (/min)	Significance σ
March-May 2010	400.15 (10)	1577.02 ± 511.95	3.94 ± 1.28	3.08
March-April 2011	279.50 (7)	989.21 ± 399.58	3.53 ± 1.43	2.47
April-May 2011	348.60 (9)	2308.07 ± 454.93	6.62 ± 1.30	5.07
May-June 2011	212.57 (6)	967.07 ± 369.16	4.55 ± 1.73	2.6

of 250 GeV.

5.2.2 *Fermi*-LAT

A circular region of 10° radius "region of interest (ROI)" was chosen around Mrk 501 for event reconstruction. We retained only those events having a zenith angle <100° to avoid background from Earth's albedo. The spectral analysis on the resulting data set was carried out by including galactic diffuse emission component model (gll_iem_v02.fit) and an isotropic background component model (iso_p7v6source) with post-launch instrumental response function P7SOURCE_V6, using unbinned maximum likelihood analysis [120, 121]. A power law spectrum was used to model the source spectrum above 200 MeV.

5.2.3 *RXTE* and *Swift*

The standard 2 PCU data from PCA onboard *RXTE* were analyzed using the method discussed in § 3.3. Windowed timing (WT) mode data from XRT onboard *Swift* were analyzed using the method discussed in § 3.4 to obtain the X-ray spectrum. The line-of-sight absorption was fixed to a neutral hydrogen column density at 1.56×10^{20} cm^{-2} [122]. A combined spectral fit was obtained for PCA and XRT data by normalizing XRT spectrum with PCA spectrum. The *Swift*-Ultra-Violet/Optical Telescope (UVOT) [123] data was used to obtain fluxes in UVW1, UVM2 and UVW2 filters at epochs corresponding with HAGAR observations. The

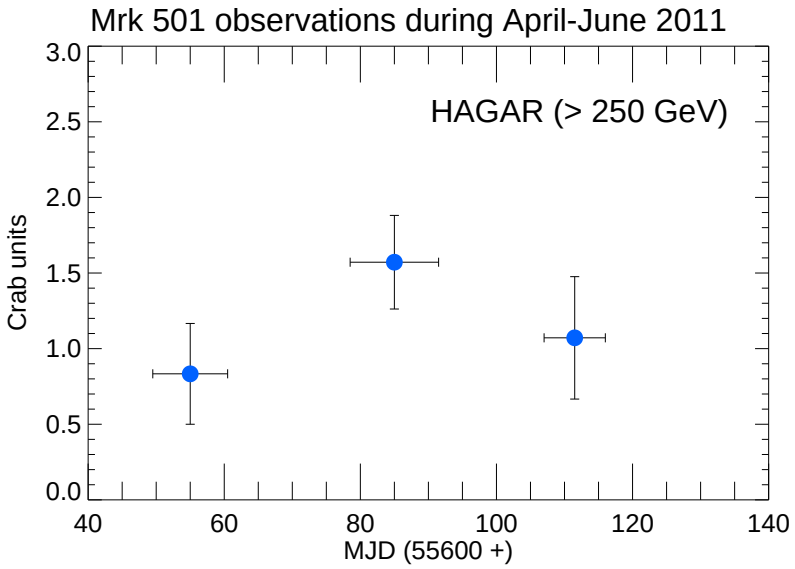

Figure 5.1: HAGAR light curve of Mrk 501 during 2011

snapshots of every individual observation was integrated with *uvotimsum* task and then analyzed with the *uvotsource* task. A source region of 10″ radius was selected around the source, while the background was extracted from a circular region 1′ which is centered in a source-free region. The flux obtained was corrected for Galactic extinction $E_{(B-V)}$=0.02 mag using [124] in each spectral band.

The "Dwell" data from *RXTE*-ASM was obtained from the ASM website[1] and was analyzed with the method discussed in [75]. A daily average flux between 15 – 50 keV from *Swift*-BAT was obtained from BAT website[2].

[1] http://xte.mit.edu/
[2] http://heasarc.nasa.gov/docs/swift/results/transients/

Table 5.2: Time periods for SEDs

Epoch	MJD	Dates	Days	SED obtained
H1	55651 - 55661	31 March - 10 April	11	YES
H2	55679 - 55691	28 April - 10 May	13	YES
H3	55707 - 55716	26 May - 03 June	10	YES
Nov 2011 [N]	55860 - 55890	26 Oct - 25 Nov	30	NO
Dec 2011 [D]	55919 - 55934	24 Dec - 08 jan 2012	15	NO
Avg 2011 [A]	55560 - 55960	30-Dec 2010 - 03 Feb 2012	400	NO

5.2.4 Optical and radio data

The optical and radio data made available in the *Fermi* multiwavelength support program websites[3] [4] are also used in this study. Details of this data set is discussed in §3.5.

5.3 Results

The HAGAR telescope has detected VHE γ-rays from Mrk 501 during 2010 and 2011, with the blazar being in a moderate state of activity. The emission reached a peak in May 2011, with a maximum flux of $\sim$1.5 Crab units, and was detected with a 5 σ significance. The integral flux in this observation period (mjd: 55679 - 55691) above 250 GeV is found to be 4.04×10^{-10} ph/cm^2/sec. The light curve based on HAGAR observations during March-June 2011 is shown in the Figure 5.1.

The source had brightened up moderately during 2011 over the entire electromagnetic spectrum, and multiwavelength light curves, from radio to γ-rays are used to understand the flux levels and variability. The multiwaveband quasi-simultaneous light curve of Mrk 501 during 2011 is plotted in Figure 5.2. Few moderate and high states are identified during this period to study the spectral variation with the activity in X-ray and γ-ray bands. SEDs were obtained for three such states by

[3] http://james.as.arizona.edu/p̃smith/Fermi/
[4] http://www.astro.caltech.edu/ovroblazars/index.php

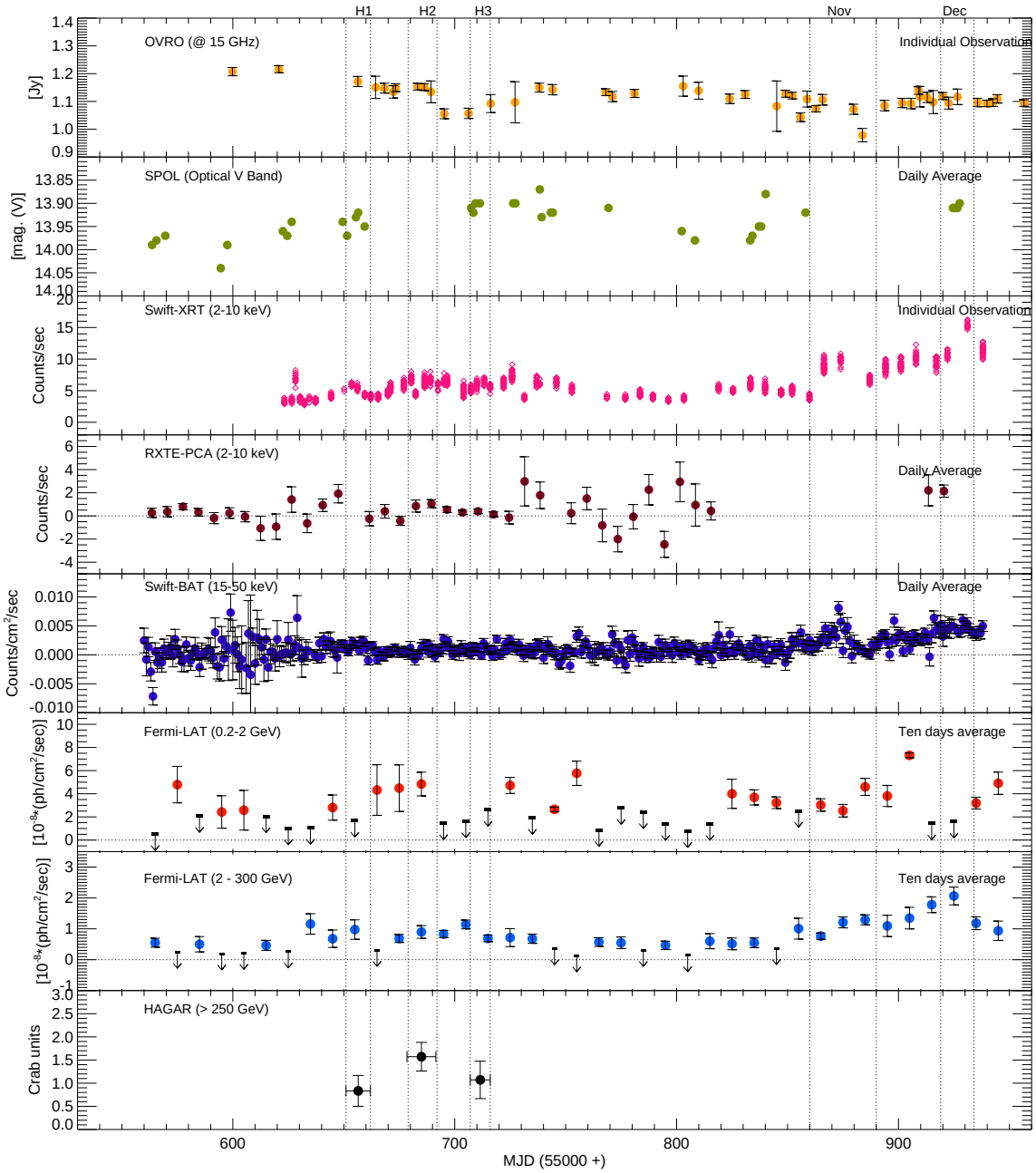

Figure 5.2: Multiwavelength light curve of Mrk 501 during 2011 and different flux states are marked

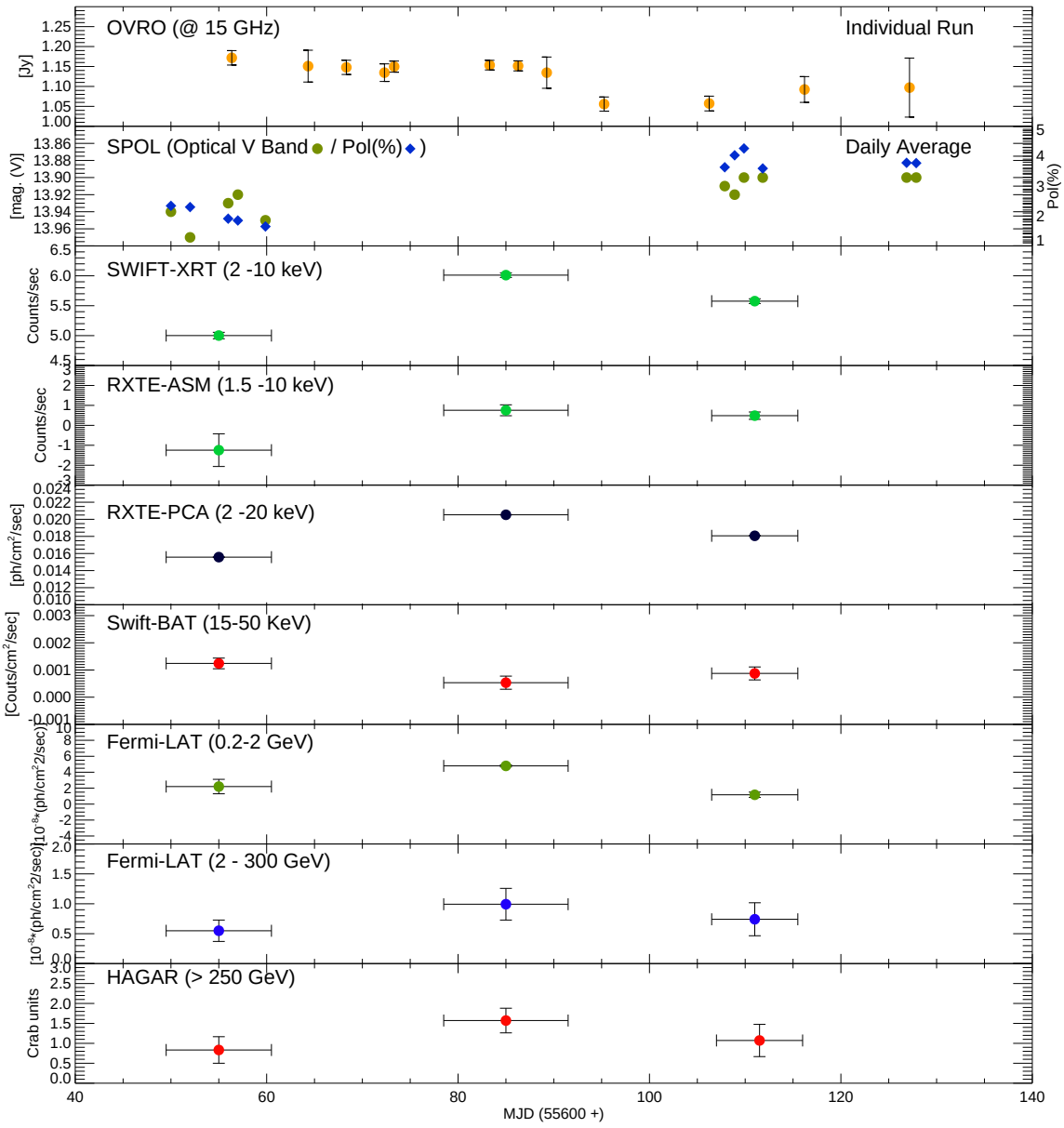

Figure 5.3: Multiwavelength light curve of Mrk 501 during during HAGAR observations

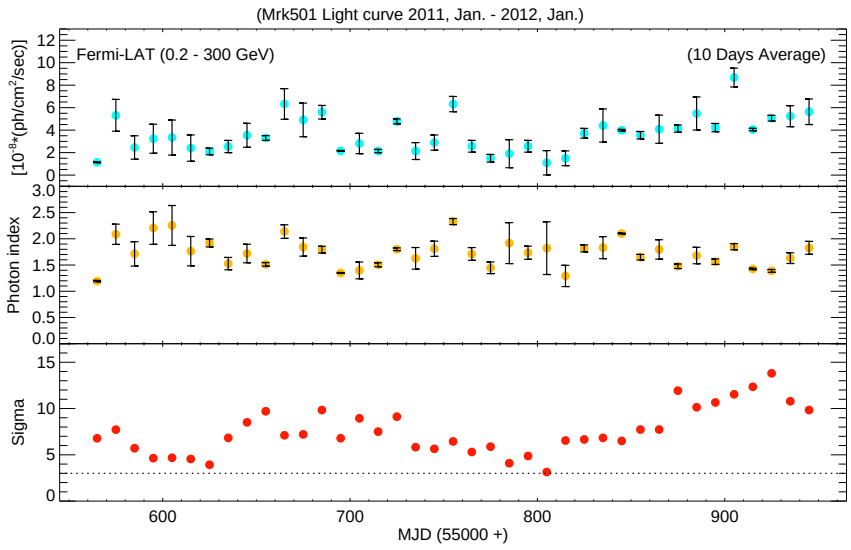

Figure 5.4: VHE γ-ray light curve of Mrk 501 in energy range 0.2-300 GeV

fitting multiwavelength data to the one zone SSC model. Details of these states are provided in Table 5.2.

5.3.1 Flux and spectral variation of Mrk 501 during 2011

Mrk 501 was found to be variable in all the wavebands during the time span of January 2011 to February 2012 with a few active states during this period. Mrk 501 was observed in moderate active state during the HAGAR observations, as seen in last panel of Figure 5.3. A positive correlation between low energy X-rays and γ-rays is seen during this period, with the peak flux being observed in May 2011 in the γ-rays and X-ray wavebands, except in hard X-rays (*Swift*-BAT).

The *Fermi*-LAT light curves of different energies during the period from 31 December 2010 to February 2012 are plotted with a bin size of 10 days in Figures 5.4, 5.5 and 5.6. The top two panels of these figures correspond to flux and photon index respectively, and the bottom panel corresponds to significance of the detection.

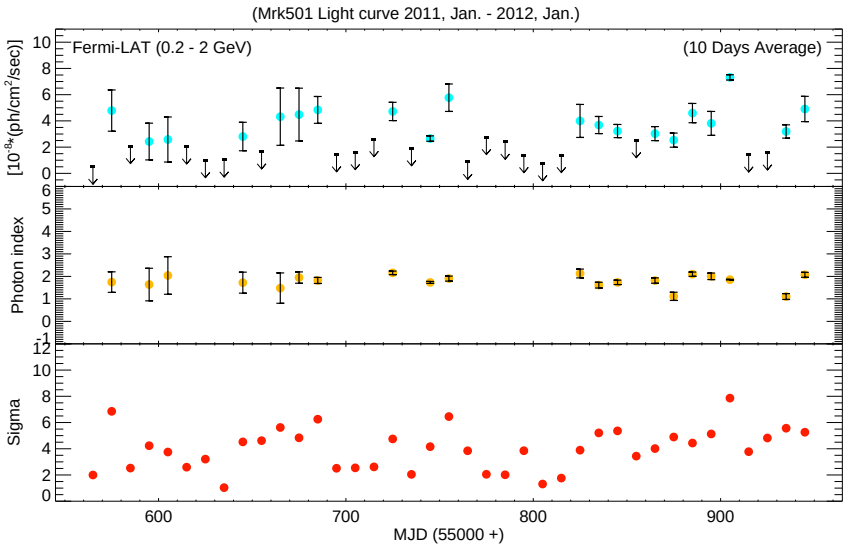

Figure 5.5: VHE γ-ray LC of Mrk501 in energy range 0.2-2 GeV

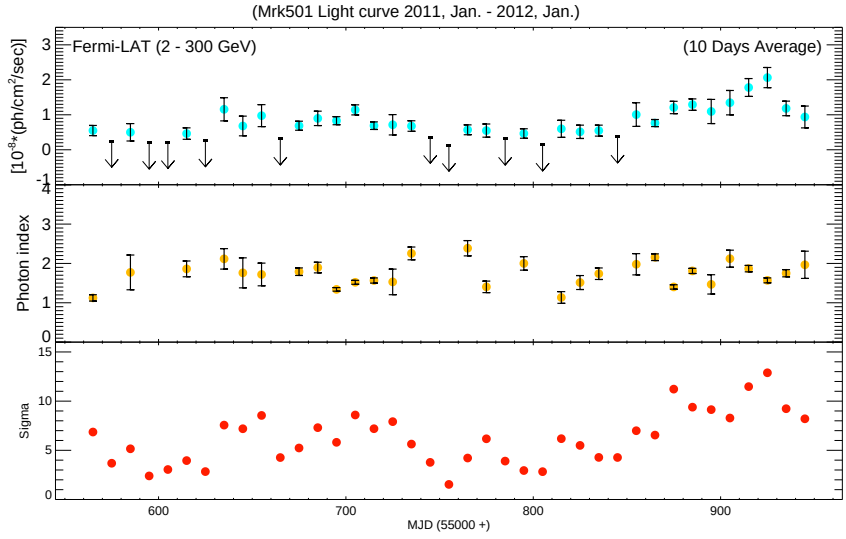

Figure 5.6: VHE γ-ray LC of Mrk 501 in energy range 2-300 GeV

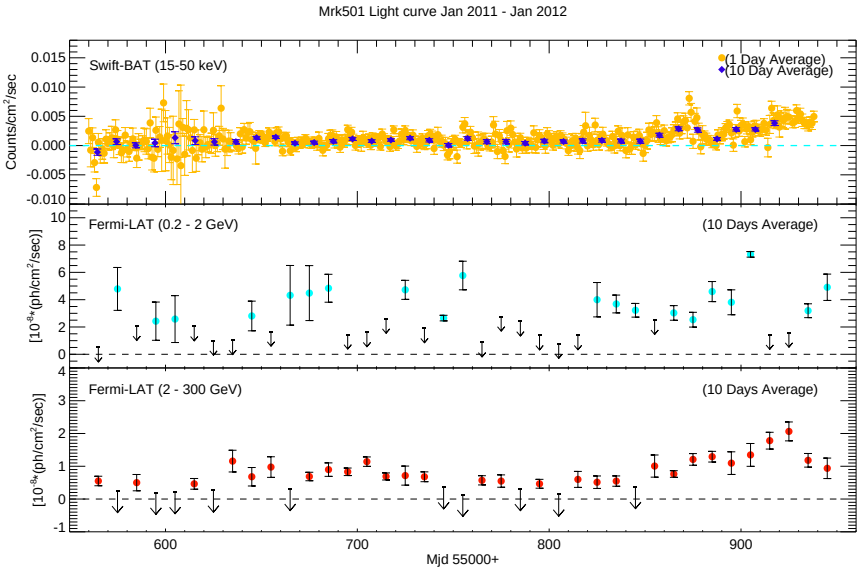

Figure 5.7: X-ray and γ-ray LC of Mrk 501 during 2011

Photon indices are only plotted for those bins that have more than 5 σ detection. An energy-dependent variation of flux in the HE γ-rays (0.2-300 GeV) has been observed. The observed flux variability by LAT in low energy γ-ray band (0.2-2 GeV) is found to be different compared to high energy band (2-300 GeV). The X-ray and γ-ray flux variations during 2011 are presented in Figure 5.7. The X-ray (*Swift*-BAT) LC show mild correlation with high energy γ-rays LC (2-300GeV). This correlation appears to be stronger at high state of the source. A similar trend was reported earlier too by [125]

The cross plots between flux and photon index, shown in Figure 5.8 clearly shows two populations, one for low energy energy bin 0.2-2 GeV and second for 2-300 GeV. The photon index increases with the increase in flux for low energies (plotted in red colour). The cross plot is scattered in the case of high energy γ-rays band and no significant trend is visible (plotted in yellow). This property indicates that low energy γ-rays are produced by an emission mechanism that is different from the mechanism producing the higher energy VHE γ-rays.

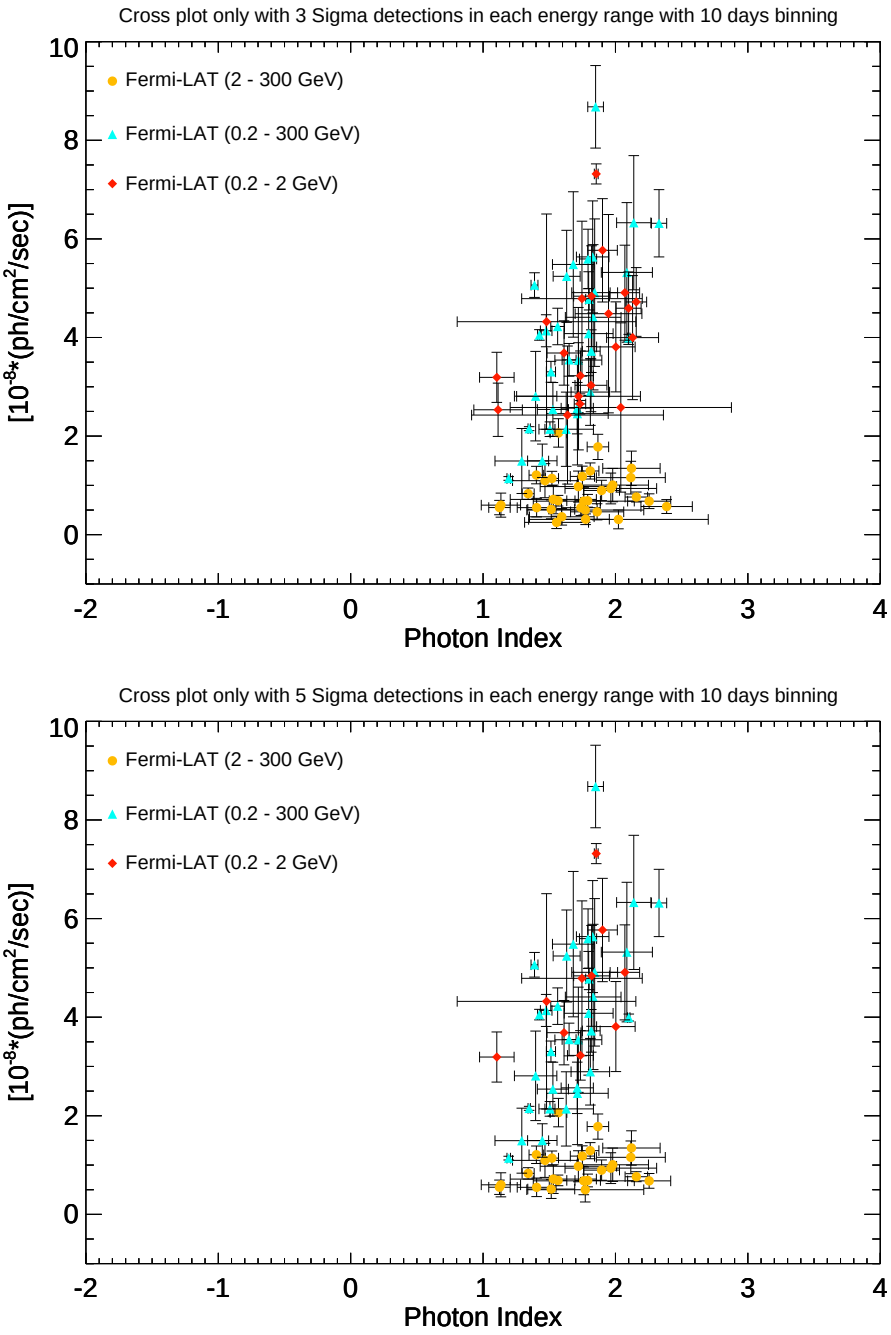

Figure 5.8: Cross plot: Flux vs Photon Index during the 2011 with 10 days bin

Studies of spectral properties of Mrk 501 in X-ray and γ-ray bands were also made. Significant spectral variability was found during the year 2011 in X-rays and γ-rays. Comparison of spectral variation with the activity of the source was studied for the period (mjd: 55651-55716) using PCA, XRT and *Fermi*-LAT instruments. X-ray and γ-ray spectral indices were obtained for several flux states, discussed in Table 5.3. Table 5.3 contains photon flux (F>0.2 GeV), photon index and time interval used for which spectra are made. The *Fermi*-LAT and PCA, XRT spectra can be fitted with a single powerlaw function.

The *Fermi*-LAT spectra during the different flux states are shown in Figures 5.9, 5.10 and 5.11. The observed LAT spectrum during May 2011 when the source was in moderate bright state, shows a very flat/hard spectrum at lower energies $\sim$(0.1-5 GeV), and the SED shows a break in the slope at 5 GeV (see Figure 5.9 bottom panel [H2]). Substantial spectral variability was also reported during the first 480 days of *Fermi*-LAT operation (2008-2009) in [126]. Mrk 501 had also shown a flare during this period, and the spectrum of this flare was found to be very hard/flat in the 10-200 GeV range. The SED in the 0.1-200 GeV range during this flare also shows a break in the slope, around 10 GeV [127].

Very hard spectrum is observed a few times during 2011 in low energy (0.2-2 GeV) as well as in high energy band (2-300 GeV), (see Figures 5.5 and 5.6). Origin of this very hard spectrum is still under debate. The flattening that was observed in the spectrum during May 2011 was not observed in other flux states during 2011. A dip is seen in the average spectrum of 2011 around 80 GeV, (Figure 5.11:bottom). A break was predicted at these energies by Abdo et. al. [126]. The observed VHE spectrum by [126] is found significantly harder than the one observed previously by HEGRA [117]. This implies that the spectrum of Mrk 501 must have a break around ($\sim$ 100 GeV) the highest *Fermi*-LAT energies.

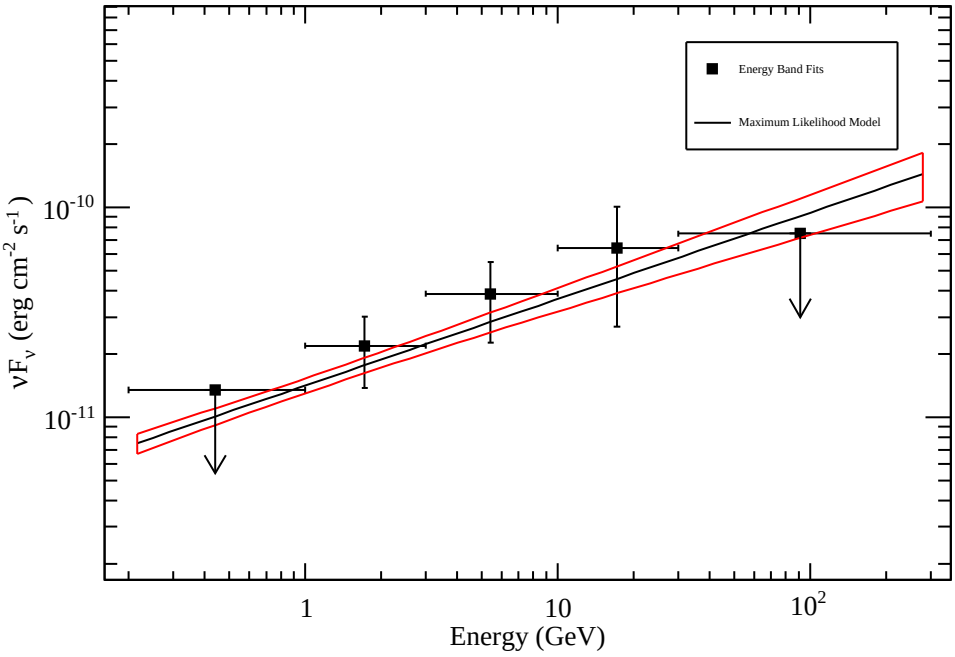

[H1]

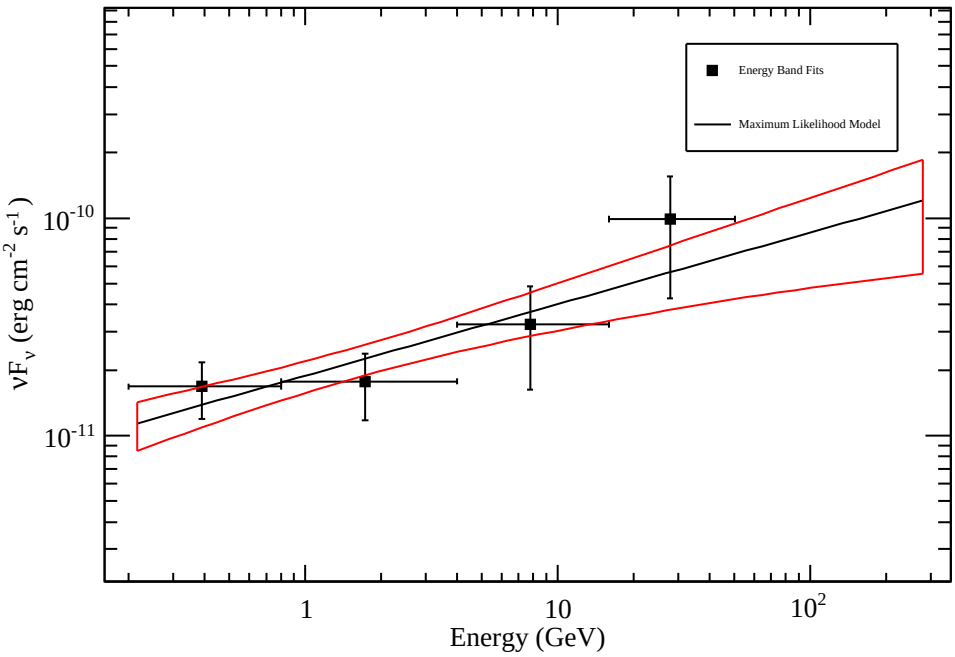

[H2]

Figure 5.9: Fermi-LAT spectra of Mrk 501 during the 2011.

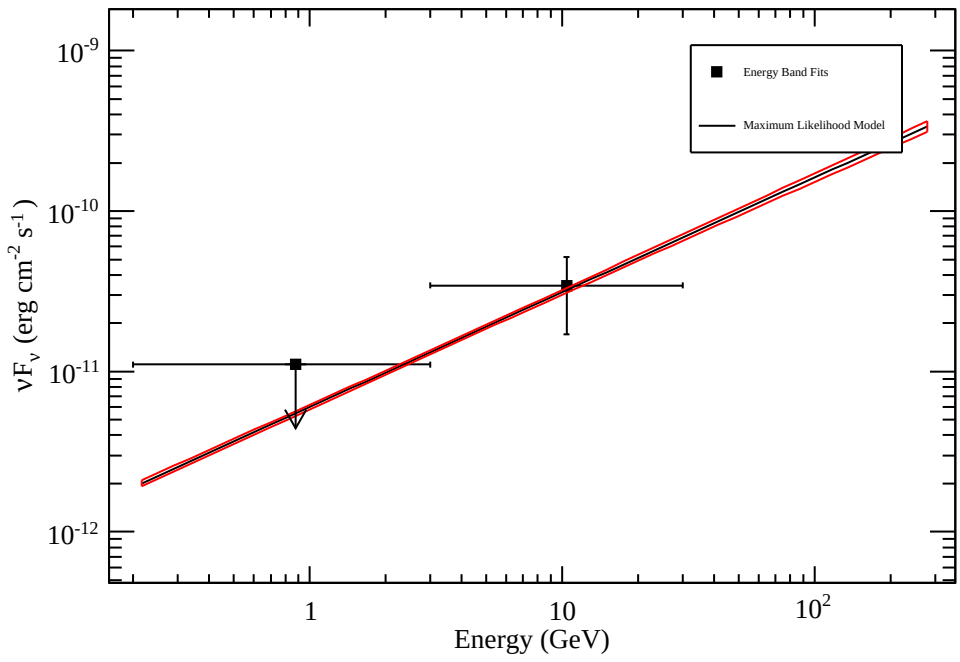

[H3]

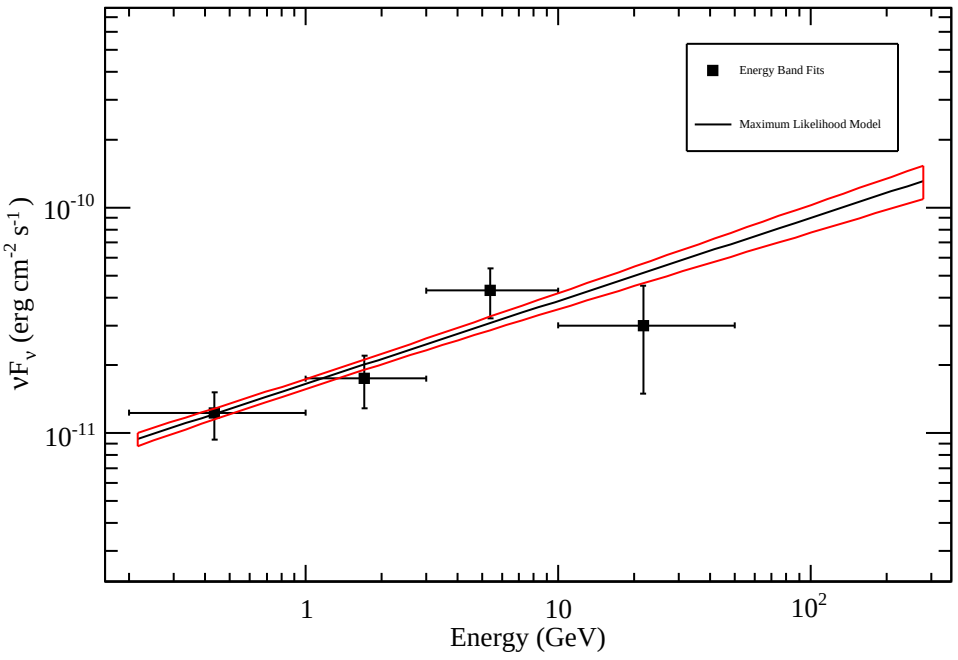

[N]

Figure 5.10: Fermi-LAT spectra of Mrk 501 during the 2011.

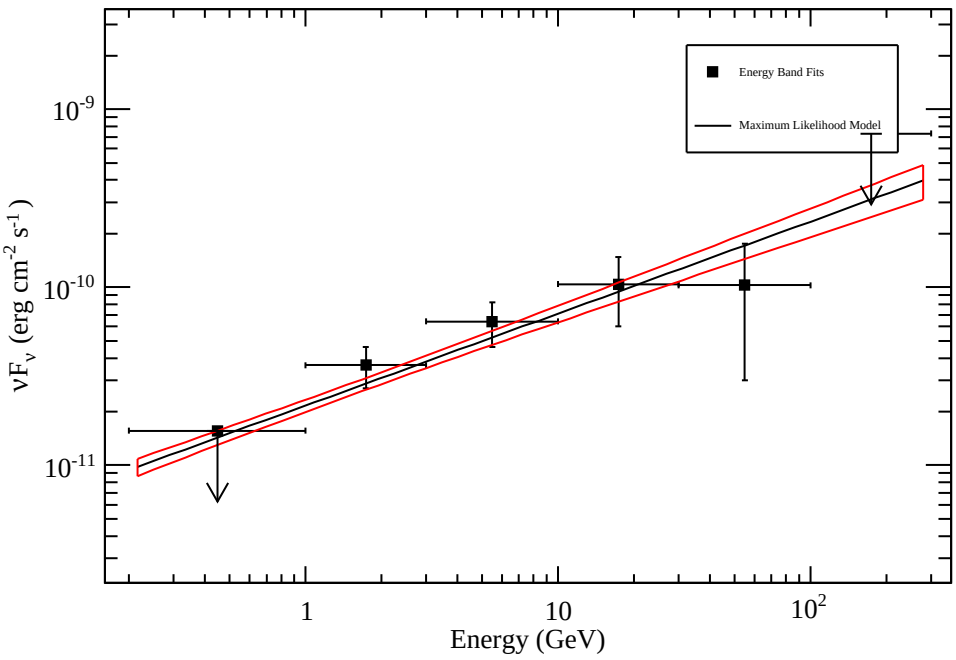

[D]

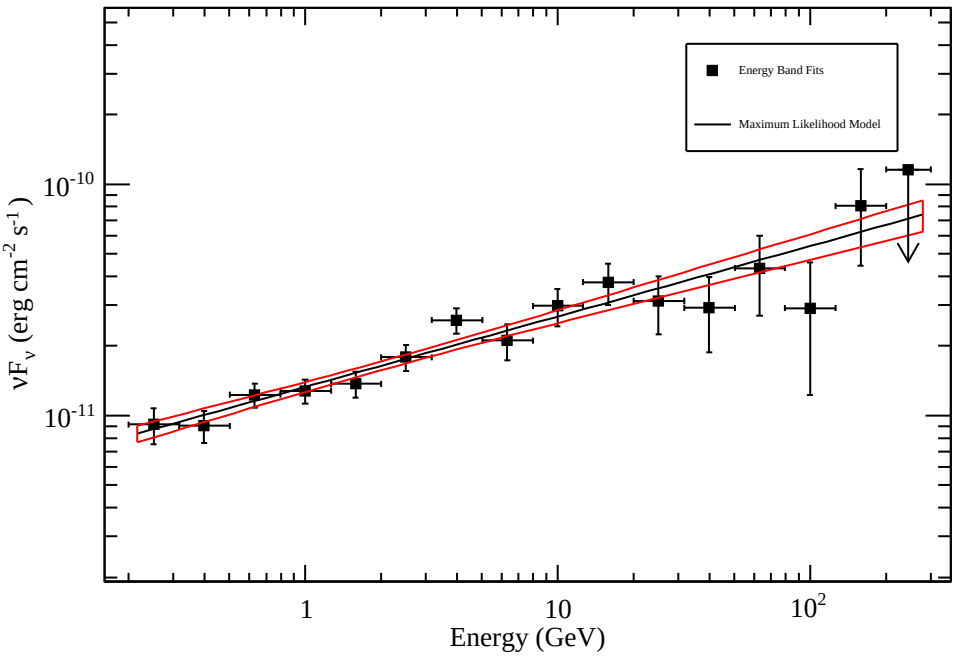

[A]

Figure 5.11: Fermi-LAT spectra of Mrk 501 during the 2011.

Table 5.3: Fermi-LAT spectrum

Epoch	Flux (0.2 - 300 GeV) $\times 10^{-8}$ ph/cm^2/sec	Photon Index	TS	XRT-PCA
H1	3.8±0.3	1.59 ± 0.04	102.8	1.95
H2	5.12±0.88	1.67 ± 0.10	128	1.87
H3	1.82±0.05	1.28 ± 0.014	68	2.11
Nov2011	4.5±0.23	1.63 ± 0.028	301	-
Dec2011	5.9±0.45	1.48 ± 0.04	279.5	-
Avg2011	3.6±0.2	1.69 ± 0.03	2417	-

5.4 Spectral Energy Distribution

We have modeled the average broadband spectrum of Mrk 501 (from radio to TeV) in the framework of the standard one-zone synchrotron self-Compton model [8], obtaining a satisfactory fit to the experimental data during three states H1, H2 and H3 (Figure 5.12, 5.13 and 5.14). This data set provides a high-quality sampling of the broadband SED of Mrk 501 in the moderate state. The obtained physical parameters are presented in Table 5.4. During all the three states we did not see any change in the observed Doppler factor δ or energy distribution of electrons. However, a variation in the magnetic field was indicated from the modeling. It appears from our SED modeling that the electron population in Mrk 501 is accelerated by shock that produces an electron spectrum of index ~ 2. A similar suggestion was made by Abdo et al. based on broadband SED modeling of the source during a quiescent state [126].

A flattening is observed in electron spectra after the break (p2) and a shift in synchrotron peak towards higher energies is also observed during bright states. Equipartition is not observed between magnetic field and electron energy density and it is correlated with the flux state.

The one-zone SSC model does not fit the SED at low energy γ-rays during the state 'H2', indicating that γ-rays may be produced via a different mechanism at these energies, or we may need a multizone SSC model.

Table 5.4: SED parameters obtained by fitting to data using $t_{var} \sim 2$ days

State	Magnetic	Doppler	log E_{min}(a)	log E_{max}(b)	E_{break}(c)	p1	p2	Sy_{pk}(d)	IC_{pk}(e)	U_e(f)	η(g)
-	field	factor	[eV]	[eV]	[eV]		-	[10^{17}]	[10^{25}]	[10^{-3}]	[$u_e^{'}/u_B^{'}$]
-	(G)	(δ)	-	-	-	-		(Hz)	(Hz)	(erg/cc)	-
H1	0.022	11.2	9.5	12.15	10.6	2.0	3.0	0.42	2.05	1.35	70.10
H2	0.016	11.2	10.1	12.30	10.6	2.0	2.9	9.78	3.56	1.6	157.07
H3	0.020	11.2	10.1	12.25	10.80	2.2	3.1	0.33	3.5	1.2	75.39

(a)→E_{min}: Minimum value of energy of the electrons present in the emission zone
(b)→E_{max}:Maximum value of energy of the electron present in the emission zone
(c)→E_{break}: Break in the electron injection spectrum
(d)→Sy_{pk}:Peak value of synchrotron bump
(e)→IC_{pk}:Peak value of IC bump
(f)→U_e:Electron energy density
(g)→η:Equipartition coefficient

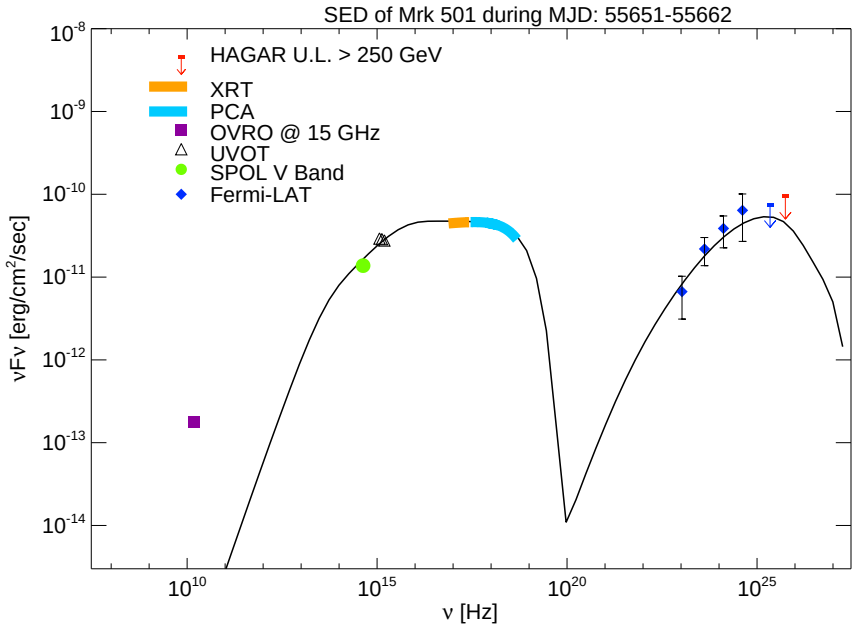

Figure 5.12: VHE γ-ray SED of Mrk 501 during April 2011 [H1]

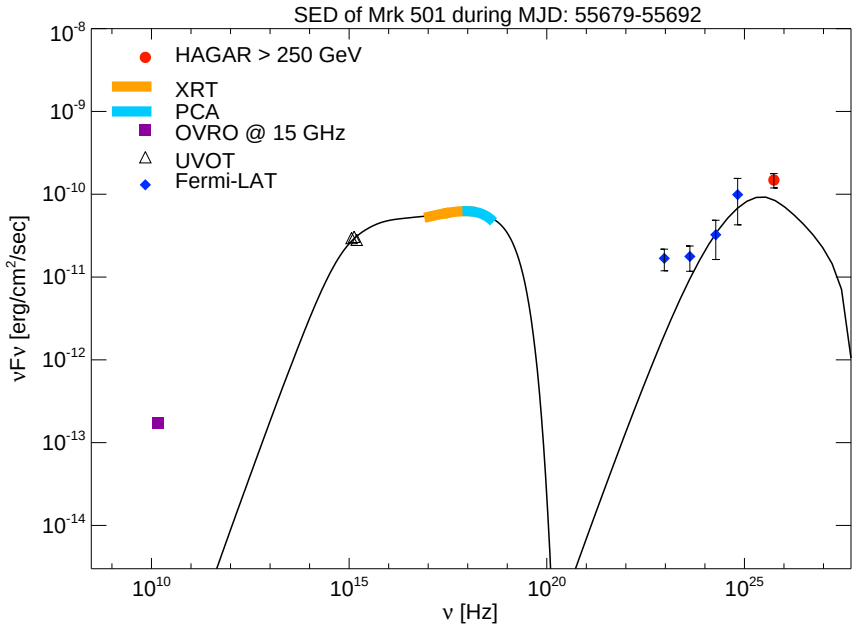

Figure 5.13: VHE γ-ray SED of Mrk 501 during May 2011 [H2]

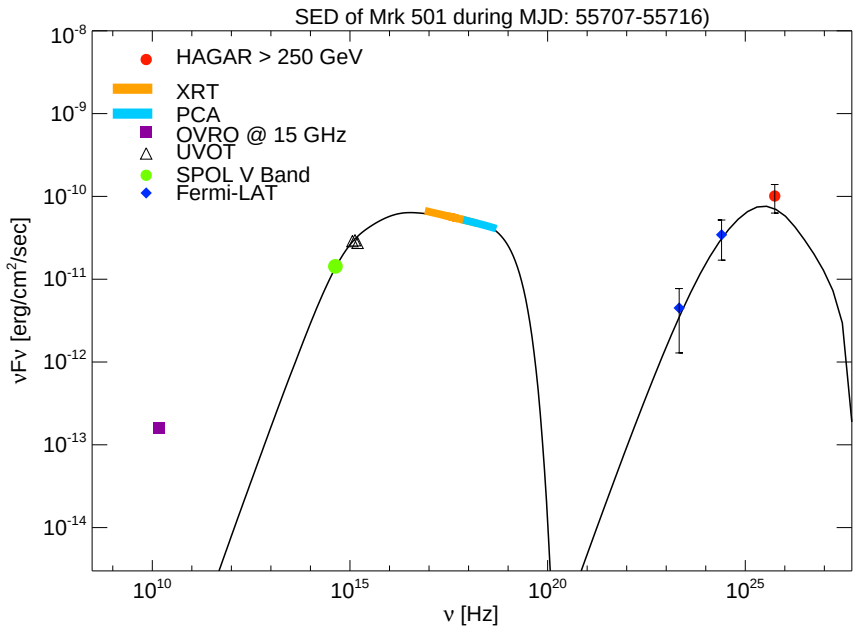

Figure 5.14: VHE γ-ray SED of Mrk 501 during June 2011 [H3]

5.5 Flux variability studies

An alternative way to constrain the physical parameters of the jet is to model the flux variability. The flux variability can also shed light on motions of the bulk outflows of the plasma in innermost region of jets which is well beyond the current imaging capabilities of telescopes in any part of the electromagnetic spectrum. Recently observed minute timescale variability of blazar emission in Mrk 501 [114] and PKS 2155-304 [128] at TeV energies can impose severe constraints on jet models and TeV emission mechanisms.

The variation in the flux is the one main defining characteristic of active galactic nuclei. It is a very powerful tool to study geometry of AGNs and their physical properties such as size and mass of black hole. The optical flux in blazars are dominated by the jets. Over the last two decades, the optical/NIR variability of blazars has been extensively studied on diverse timescales [129, 130, 131, 132, 118, 133, 134]. Search of intra-night optical variability (INOV) has been attempted by

Table 5.5: Average V band optical flux as measured from HCT

Date	Magnitude	error
11 June	10.264	0.002
13 June	10.15	0.005

several groups in past, for e.g. Gupta et.al detected a variation of 0.05 magnitude in the R-band over time scales of 15 min [118]. Several attempts were made to constrain the black hole size using INOV and short time scale optical variability [119]. Correlation studies between optical and γ-rays were also attempted during variability to differentiate between the leptonic and hadronic origin of VHE γ-rays [135, 114].

Mrk 501 was observed in V filter using HFOSC, mounted on HCT during 11 and 13 June 2011. A search for INOV during its moderate activity state in VHE γ-rays (as observed from HAGAR) was attempted using data of 13 June 2011, to constrain the size of emission zones. Pre-processing of Mrk 501 images and aperture photometry were carried out using the procedure discussed in chapter 3. A differential light curve of source was obtained relative to the field stars. Three comparison stars in field of Mrk 501 selected as reference stars are shown in Figure 5.15. The intra-night differential light curve shown in Figure 5.16. We could not detect any significant INOV during our observation. Average magnitudes for both days are provided in the table 5.5.

5.6 Modeling of rapid variability in Mrk 501 to constrain the emission mechanisms

Several blazars have recently displayed minute-timescale variability at TeV energies [114, 128]. This has resulted in a great deal of interest in the emission mechanisms responsible for these TeV flares. Suggestions range from a coherent instability in a compact emission region [136], misaligned minijets inside the main jet [137], jet deceleration [138, 139], to wiggles in an anisotropic electron beam directed along

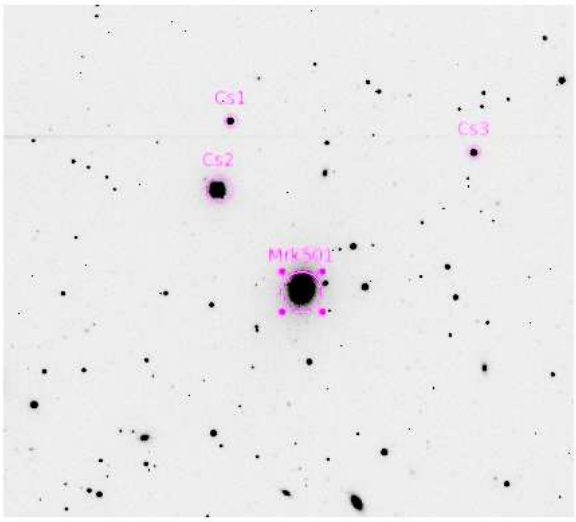

Figure 5.15: Image of Mrk 501 field taken from HCT, comparison stars are indicated in image.

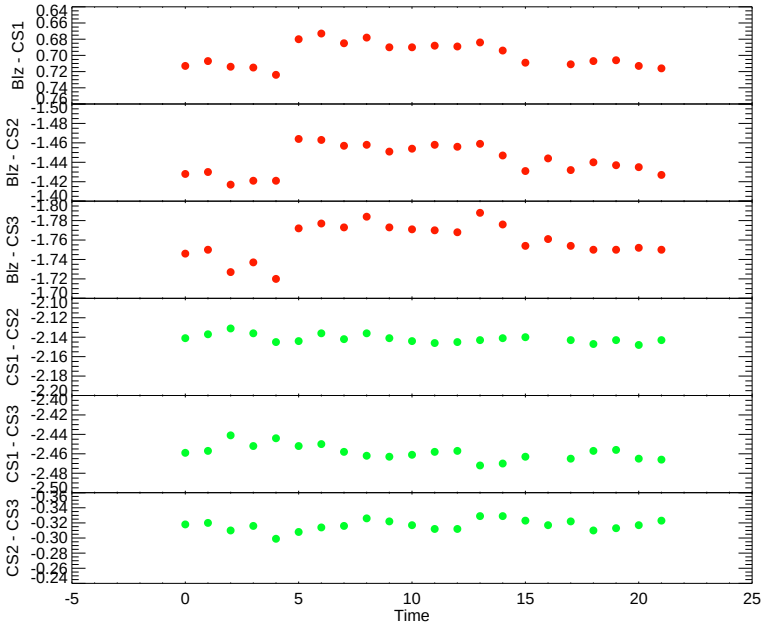

Figure 5.16: Result of INOV on 13 June 2011, as observed from HCT

the jet [140]. Considerable attention has also been paid to correlated variability at other wavelengths (such as optical wavelengths) exhibited by TeV blazars [133]. In general, there have been several mechanisms proposed for producing the observed variability in the jet emission, ranging from plasma mechanisms [141] to beamed radiation [142]. TeV variability is somewhat unique, in that explaining even steady-state TeV emission from blazars poses significant challenges. Electron emission (via the synchrotron self-Compton process or the external inverse Compton process) is frequently invoked. While electrons are certainly the prompt radiators, both these mechanisms require very highly relativistic electrons (random Lorentz factors $\gamma \approx 10^4 - 10^5$ or more). This in turn poses severe electron reacceleration problems.

We now pay attention to the role of bulk plasma outflow in a couple of popular models for TeV flares. In the first model we discuss, the bulk plasma outflow is necessary to alleviate the problem of copious pair production (and consequent degradation of TeV photons) in the TeV emission region. In the second one, the idea of a highly anisotropic, directed beam of TeV emitting electrons is central to explaining the observed variability. We point out later that the bulk Lorentz factor (Γ) of the plasma outflow is related to pressure anisotropy in the jet. The magnitude of Γ (and therefore that of the pressure anisotropy) is limited by the excitation of hydromagnetic waves. We will then examine the role of the pressure anisotropy in exciting the well studied firehose instability in the jet. Jet disruption due to this instability is found to be a viable explanation for the observed variability at TeV energies.

5.6.1 TeV variability due to a compact emission region: the pair production problem

The first scenario we examine is due to Begelman, Fabian & Rees [136]. In this scenario, the TeV photons are produced via inverse Compton upscattering of an existing soft photon population by energetic electrons. Using a peak frequency of 10^{16} Hz for the soft photons and a bulk Lorentz factor of $\Gamma \approx 50$, they estimate that

the random Lorentz factor of the energetic electrons $\gamma \approx 10^4$ in order to produce TeV emission. They relate the short variability timescales (of the order of a few minutes) to the size of the emission region via the light crossing time argument. This argument implies that the emission originates from a region whose size is a small fraction of the black hole's Schwarzschild radius [136]. For relativistic, Poynting flux dominated jets, it is possible that structures as small as the gravitational radius of the black hole are imprinted on the jet as it is launched, and modulate the emission far away from the central region (Kirk & Mochol [143]). Another possibility is that the TeV flares could originate in highly localized fluctuations in the outflowing jet plasma due to instabilities.

Importantly, Begelman, Fabian & Rees [136] show that the outflowing plasma must have a substantial bulk Lorentz factor $\Gamma \approx 50$ in order for the TeV photons to escape from the compact emission region without producing pairs. If this was not so, copious pair production due to the interaction between the TeV photons and locally produced synchrotron photons would substantially degrade the TeV photons produced. Furthermore, Begelman, Fabian & Rees [136] argue that the TeV emitting region needs to be located far away from the central black hole (at least 100 Schwarzschild radii) in order to avoid rapid degradation of the TeV photons due to pair production on the soft photon background of the accretion disk [144]. Assuming a reasonable jet opening angle, this implies that the size of the emission region is around two orders of magnitude smaller than the transverse dimension of the jet, at the distance where the variable TeV emission originates. This scenario thus envisages a very compact emission region comprising energetic electrons flowing out with a bulk Lorentz factor ≈ 50.

5.6.2 TeV variability due to beamed electron distribution?

Ghisellini et al. [140] outline an interesting scenario where the TeV emission is due to a highly anisotropic electron beam. The electrons are almost co-aligned in a narrow beam. Another way of stating this could be to say that the electrons are hot

along the beaming direction and cold in the perpendicular direction; the jet pressure (as observed by a distant 'lab" observer) is highly anisotropic. It would be possible to define a meaningful bulk Lorentz factor along the beaming direction, but the jet pressure would be anisotropic even in the bulk comoving frame. The electrons could be emitting TeV radiation via the inverse Compton scattering of soft photons. As an extreme case, they calculate the electron Lorentz factor in a situation where there is no bulk motion and the soft photons are isotropically distributed (although, as mentioned earlier, the highly anisotropic electron beam clearly implies ordered bulk motion). They find that the electron's random Lorentz factor γ needs to be $\approx 10^6$ in order to account for TeV photons produced via inverse Compton scattering off soft photons of energies ~ 1 eV. Ghisellini et al. [140] envisage large-scale wiggles in the beam, so that the radiation would be observed only for the fraction of time that the beam points toward the observer, leading to variability. The electron beam is assumed to retain its coherence, and the variability is only because of the fact that the large scale magnetic field points toward the observer for a limited time. Such a scenario avoids explicit reference to a compact emission region.

A central feature of Ghisellini et al.'s model [140] is the highly beamed, anisotropic electron distribution, which leads to the parallel pressure greatly exceeding the perpendicular one. We show below that the electron pressure anisotropy is unlikely to assume extreme values. We show, however, that even modest amounts of pressure anisotropy are enough to destabilize the large-scale structure of the jet via the firehose instability, and this could result in observed variability.

5.6.3 Our model

Our scenario is similar to Begelman et al. [136] in that the radiating electrons possess a random Lorentz factor γ ranging from 10^4 to 10^6 as well as a bulk Lorentz factor Γ. The issue of pressure anisotropy highlighted by Ghisellini et al. [140] is important in our scenario too.

In this work, we envisage a jet that comprises an electron-proton plasma which

streams along the forward jet direction. All the quantities referred to from here onwards are defined in the distant observer's frame of reference. Electrons would be bound to the protons, and stream along with them, but would also possess random Lorentz factors $\gamma \approx 10^4$–10^6. Since the electrons have such high random Lorentz factors, and the protons are most likely much colder, the electrons are the dominant contributors to the pressure. The velocity with which the plasma streams along the jet is typically restricted to the Alfvén speed $v_{\rm A}$ via a self-limiting process. This limit on the streaming speed is imposed by hydromagnetic waves emitted by the electrons [145, 146], which also scatter the electrons and limit the degree of anisotropy. Following Wentzel [145, 147] we envisage the equilibrium particle distribution function in momentum $\mathbf{p}$ of the jet plasma to be of the form

$$f(\mathbf{p}) = f_i(\mathbf{p})\left(1 + 3\,|\mu|\frac{v_A}{c}\right), \tag{5.1}$$

where $f_i(\mathbf{p})$ is the isotropic part of the distribution function and satisfies

$$\int f_i(\mathbf{p}) d^3\mathbf{p} = 1\,. \tag{5.2}$$

The quantity μ is the cosine of the particle pitch angle and represents the fraction of the particle momentum along the direction of the bulk motion of the jet. The quantity c is the speed of light. The second term in the brackets expresses the anisotropy of particle distribution. It may be noted that the anisotropy in this formulation is typically only a perturbation; in other words, we require that $v_{\rm A}/c \ll 1$. Wentzel's [145] formulation includes a higher order term $\propto \mu^2$ on the right hand side of Eq 5.1, but we don't consider such a term in the interest of simplicity. While we do not appeal to a specific mechanism to generate the electron anisotropy, such as the pitch angle dependence of synchrotron losses [146]; [147] or the intrinsic jet launching mechanism [148], we emphasize that this distribution (Eq 5.1) is only mildly anisotropic, and the degree of anisotropy in is restricted to $\approx v_{\rm A}/c \ll 1$. Furthermore, the bulk streaming speed of the jet is restricted to be approximately equal to the Alfvén speed $v_{\rm A}$. The ratio of the parallel pressure $P_{||}$ to the perpendic-

ular pressure $P_\perp$ in the jet arising from the distribution given by Eq 5.1 is (Wentzel [145])

$$\frac{P_{||}}{P_\perp} = \frac{1 + v_A/c}{1 - v_A/c} \tag{5.3}$$

Since the bulk streaming speed of the jet is $\approx v_A$, we can write the following expression for the jet bulk Lorentz factor Γ:

$$\Gamma = (1 - v_A^2/c^2)^{-1/2}\,, \tag{5.4}$$

keeping in mind the fact that Γ cannot greatly exceed unity, since $v_A/c \ll 1$.

Before we move on to analyzing the firehose instability arising out of the anisotropic pressure distribution in the jet, we note that electron reacceleration within the jet is essential, in view of the copious radiative losses they experience. The electrons could be energized by resonating with the very hydromagnetic waves they shed, much in the same manner as cosmic rays are thought to be accelerated [149], or by wave-particle interactions with a separate, pre-existing wave population [150]. It is also possible that electrons are reaccelerated by the turbulence initiated by a previous episode of the firehose instability; such a scenario is often invoked for electron acceleration in solar flares [151]. The protons, on the other hand, are likely to remain substantially colder.

5.6.4 The Firehose instability due to $P_{||} > P_\perp$

The well known firehose instability (also often referred to as the gardenhose instability) is typically operative when the parallel pressure $P_{||}$ in the forward jet direction exceeds the perpendicular pressure $P_\perp$ transverse to the jet [152]. This nonresonant, fluid instability will result in large-scale displacements in the beam, and possible disruption of the large-scale magnetic field in the jet [153], which could result in variability in the observed TeV emission. Resonant instabilities can also be

operative, but they typically only result in a redistribution of electron pitch angles, while nonresonant, fluid instabilities disrupt the large-scale magnetic field. The arguments of the previous section suggest that the jet pressure is unlikely to be highly anisotropic. We show hereafter that the growth timescales for the firehose instability in a typical TeV emitting jet are in agreement with observed variability timescales, even for moderate pressure anisotropies.

5.6.5 Growth timescale of the firehose instability

While there are several treatments of the firehose instability, we concentrate on one that offers a convenient analytical approximation to the maximum growth rate of the relativistic firehose instability from a solution of the dispersion equation. The maximum growth rate $\omega_{\rm gr}$ of this instability can be approximated to within $\approx 20\%$ by the following expression:[154]

$$\omega_{\rm gr} = 0.55\,\omega_{\rm LR}\,\frac{(1-H)}{8+\Lambda^{1/2}}\,. \tag{5.5}$$

The quantity $\omega_{\rm LR}$ is the mean relativistic gyrofrequency.

given by

$$\omega_{\rm LR} = \frac{e\,B}{\gamma\,m_e\,c} \quad {\rm s}^{-1}, \tag{5.6}$$

where e is the electron charge, B is the large-scale magnetic field in Gauss, γ is the random Lorentz factor of the TeV emitting electrons, m_e is the electron mass and c is the speed of light. The growth timescale given by Eq (5.5) is an approximation to the growth rate derived from solving the dispersion relation for the instability.

The quantity H is the magnetic pressure nondimensionalized by the particle anisotropy, and is defined as

$$H = \frac{B^2}{4\,\pi\,P_{||}(1-P_{\perp}/P_{||})}\,. \tag{5.7}$$

The quantity Λ is defined as

$$\Lambda = 1 + \frac{c^2}{v_{\rm A}^2}\,, \tag{5.8}$$

and can be related to the bulk Lorentz factor Γ via Eq (5.4). It may be noted that the gyrofrequency is used in Eq (5.5) only as a convenient parametrization for the growth timescale, and does not suggest any kind of resonance; the relativistic firehose instability is a nonresonant one.

Identifying the Alfvén speed as

$$v_{\rm A}^2 \equiv \frac{B^2}{4\,\pi\,m_p\,N}\,, \tag{5.9}$$

where m_p is the proton mass and N is the particle number density, we can express H (Eq 5.7) as

$$H = \frac{m_p}{m_e}\,\frac{v_A^2}{\gamma\,c^2\,(1 - P_\perp/P_{||})}\,, \tag{5.10}$$

where m_e denotes the electron mass. We have used the proton mass in computing the Alfvén velocity, since they are the heavier species, and are the primary contributors to the matter density. We have also used $P_{||} = \gamma\,N\,m_e\,c^2$ in deriving Eq (5.10), since we expect the energetic electrons (with $\gamma \approx 10^6$) to be the primary contributors to the jet pressure.

The maximum growth timescale of the relativistic firehose instability is

$$t_{\rm gr} = 2\pi/\omega_{\rm gr}\,. \tag{5.11}$$

As mentioned in § 5.9, the growth timescale is evaluated in the frame of the distant

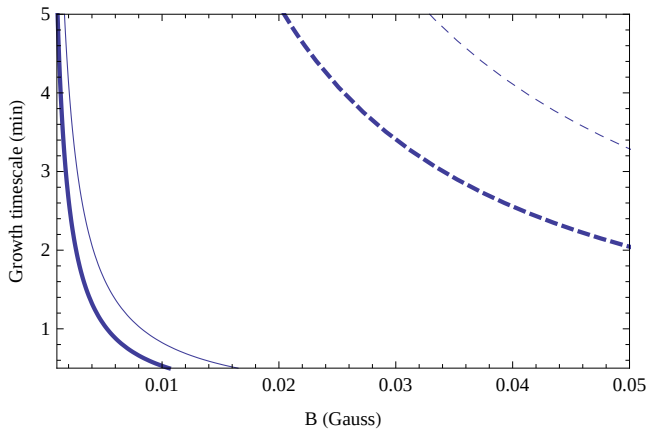

Figure 5.17: The predicted variability timescale $t_{\rm gr}$ in minutes as a function of the magnetic field B in Gauss. The thin solid line is for $\gamma = 5 \times 10^4$, $\Gamma = 1.01$ and the thick solid line is for $\gamma = 5 \times 10^4$, $\Gamma = 5$. The thin dashed line is for $\gamma = 10^6$, $\Gamma = 1.01$ and the thick dashed line is for $\gamma = 10^6$, $\Gamma = 5$.

observer. Using Eqs (5.10), (5.8), (5.6), (5.5), (5.4) and (5.3) in Eq (5.11), we get

$$t_{\rm gr} = 2\pi \, \frac{\gamma \, m_e \, c}{0.55 \, e \, B} \left[8 + \left(1 + (1 - \Gamma^{-2})^{-1} \right)^{1/2} \right] \times \left[1 - \frac{1}{\gamma} \, \frac{m_p}{m_e} (1 - \Gamma^{-2}) \, \frac{1 + (1 - \Gamma^{-2})^{1/2}}{2 \, (1 - \Gamma^{-2})^{1/2}} \right]^{-1} \tag{5.12}$$

We show the results for the maximum growth timescale evaluated using Eq (5.12) in Figure 5.17. We use the bulk Lorentz factor Γ, the random electron Lorentz factor γ and the value of the ambient large scale magnetic field B as our parameters. We now comment on the range of values we use for the parameters employed in the calculations.

5.6.6 Range used for γ

As mentioned earlier, we assume that the TeV radiation is produced due to energetic electrons upscattering soft photons via the inverse Compton mechanism. Values quoted in the literature for the random Lorentz factor γ used to generate TeV emission via the inverse Compton mechanism range from $\approx 10^4$ (e.g., Begelman et al. [136]) to $\approx 10^6$ (Ghisellini et al. [140]). We use two values for the random Lorentz factor of the electrons in our calculations: $\gamma = 5 \times 10^4$ and 10^6.

5.6.7 Range of magnetic field values

We consider magnetic field values in the range $0.001 < B < 0.05$ G. This is representative of the values derived for TeV blazars. Using a one-zone synchrotron self-Compton model, multi-wavelength data fitting requires that the magnetic field in the emission regions of TeV blazars MrK 421 and MrK 501 be ≈ 0.01 G [126, 7]. Similar considerations yield a value for the magnetic field of 0.03 G for the high state of Mrk 421 [99]. Giroletti et al. [155] obtain $B \approx 0.01$ G from equipartition considerations in relation to radio observations of the TeV blazar MrK 501.

5.6.8 Range used for Γ

We next discuss the values we adopt for the bulk Lorentz factor Γ. We use $\Gamma = 1.01$ (corresponding to $P_{||}/P_{\perp} = 1.32$) and $\Gamma = 5$ (corresponding to $P_{||}/P_{\perp} = 100$). Since the assumption regarding mild anisotropy (Eq 5.1) requires that the ratio of the Alfvén speed to the speed of light $v_{\rm A}/c \ll 1$, the bulk Lorentz factor Γ needs to be restricted to values that are not appreciably greater than unity (Eq 5.4). These values for Γ imply relatively modest constraints on the jet production mechanism. Although rather high values for Γ are often discussed in the literature, it is worth mentioning that multi-epoch radio mapping of parsec-scale jets in TeV emitting blazars suggest that $\Gamma \approx 1$–3 [156, 155]. Similar values for Γ are also implied by

blazar unification schemes [157]. Theoretical considerations regarding launching electron-proton jets imply that asymptotic bulk Lorentz factors are likely to be limited to values well below 10 [158].

The broad conclusion from Figure 5.17 is that a wide range of realistic parameters ($5 \times 10^4 < \gamma < 10^6$, $1.01 < \Gamma < 5$, $0.001 < B < 0.05$ G) yield growth timescales of the order of a few minutes for the firehose instability.

5.6.9 Discussion on minute scale TeV variability

We have considered the problem of minute timescale variability in TeV blazars. We assume that the TeV radiation is produced by highly relativistic electrons ($\gamma \approx 10^4 - 10^6$) scattering off soft photons via the inverse Compton mechanism. The jet is beamed towards the observer with a bulk Lorentz factor Γ. These aspects are similar to those considered in previous treatments [136, 140]. However, we point out here that bulk streaming of the jet plasma results in the parallel pressure $P_{||}$ being $\gtrsim$ the perpendicular pressure $P_{\perp}$. We furthermore show that even such a mild pressure anisotropy can give rise to a nonresonant, fluid instability called the firehose instability, which can result in a disruption of the large-scale jet over timescales of a few minutes. In other words, we have shown that the firehose instability is essentially unavoidable in the type of situations considered by Begelman et al. [136] and Ghisellini et al. [140].

For γ ranging from 5×10^4 to 10^6, $\Gamma \gtrsim 1$ and $0.001 < B < 0.05$ G, we find that the firehose instability growth timescale is of the order of a few minutes (Figure 5.17), which is in agreement with the observed TeV variability timescales for Mrk 501 (Albert et al. [114]) and PKS 2155-304 (Aharonian et al. [128]). Hence the disruption of the large-scale jet features due to the firehose instability provides a natural explanation for the observed variability at TeV energies.

5.7 Summary

We have presented here a multiwavelength study of the activity of Mrk 501 as measured by HAGAR and other ground and space based instruments. Mrk 501 is the second closest TeV blazars after Mrk 421 which was identified as a VHE γ emitter. The multifrequency correlations and spectral energy distribution of Mrk 501 were studied intensively in the past by [159, 112, 160, 161, 162, 163] , but the nature of this object is still far from understood. The main reasons for this is lack of simultaneous multifrequency data during long periods, and the moderate sensitivities of the γ-ray instruments. Since the detection of this source from Whipple observatory, it has shown several high states over the entire electromagnetic spectrum and a few orphan TeV flares [127].

Fast variability over time scales of minutes detected during such orphan flares which makes this object very interesting to study [114]. The broadband spectral energy distribution of Mrk 501 can be explained by either the leptonic models [47, 164, 162] or the hadronic models [43, 49, 6]. In this work we modeled the observed SED with in the leptonic framework using a one zone SSC model.

Recent extensive studies of the source including this work suggest the blazar zone is filled with a uniform magnetic field of 0.02 G and the plasma is moving with Doppler factor of $\sim$12 [165, 126, 166]. These works also suggest that the electrons in the jet are accelerated at shock fronts. These studies also provide constraints on the particle population, and it is suggested that protons are also present in the jet, but they might be cold.

Chapter 6

Summary and Future

6.1 Summary

6.1.1 Study of TeV blazars

The understanding of the global nature of the emission from blazars is a highly challenging problem. These blazars are excellent laboratories to study the environment within the jets, as a dominant part of the observed nonthermal emission from AGN originates within the jets. A unique explanation of the observed broadband emission has so far not been successfully obtained due to a lack of multiwavelength data. The observed broadband data can be explained by either leptonic or hadronic models. Strong effort is being made in the recent years on simultaneous multiwavelength campaigns in order to differentiate between these two competing models. The multiwavelength flux and spectral studies have provided substantial progress, and considerable attention has also been paid to correlated variability at all wavelengths. In general, there have been several mechanisms proposed for producing the observed variability in the jet emission, ranging from plasma mechanisms to beamed radiation.

In this work, the multiwavelength studies were performed on the brightest TeV blazars, namely, Mrk 421 and Mrk 501, in order to understand the cause of flux and spectral variations observed in the entire electromagnetic spectrum over a wide range of time scales. We have attempted to provide meaningful constraints on the emission models and physical parameters during different flux states. We have studied and compared the change in emission mechanisms and physical parameters during the high and moderate states.

Mrk 421 and Mrk 501 were detected by HAGAR in a moderate activity state ($\sim$ 1 Crab unit) in the TeV energies on several occasions. In addition to these moderate states, Mrk 421 had also underwent one of its brightest flux states during February 2010, reaching its maximum flux of $\sim$ 7 Crab units on 17 February 2010, as observed by HAGAR, VERITAS and HESS. It is suggested that the multiwavelength flare may be caused by a passing shock in the jet via synchrotron self Compton mechanism. This shock can be caused by the change in the bulk motion of the plasma. The broadband emission from Mrk 421 in moderate ([7], this work) as well as in high state can be explained by a one zone SSC model [91, 84, 99]. The general understanding about Mrk 421 has improved in the recent years owing to these campaigns. Recent studies suggests that the emission zone of Mrk 421 is filled with a uniform magnetic field of $\sim$ 0.035 G and electrons which have a broken powerlaw distribution. This emitting zone moves in the forward direction with a Doppler factor $\sim$ 23 in the jet (this work) and [7]. Horan et al., modeled Mrk 421 with higher magnetic field $\sim$ 0.12 G and higher Doppler factor $\sim$ 90 using SSC+EC models [95].

In the case of Mrk 501, the SED at the low state of activity could be modeled well with a one zone SSC framework. However, in the high state the one zone SSC model could not reproduce the SED at all energy ranges. While the fit was good in the X-rays, the low energy γ-rays were not reproduced well. The energy dependent flux and spectral variation also suggested that it may be possible that low energy γ-rays are produced by a different mechanism in the source. The physical parameters obtained from SED modeling during the moderately active state as observed by

HAGAR indicate a magnetic field (B) of $\sim$ 0.02G and Doppler factor of (δ) $\sim$ 12. These values are consistent with the estimates made by [126]. However, at quiescence, the magnetic field and Doppler factor are higher and estimated to be B $\sim$ 0.313 and $\delta \sim 20$ as indicated in Anderhub et al. [135].

It is clear from the SED modeling of a large number of observations of Mrk 421 and Mrk 501 that they do not obey equipartition between electron energy density and magnetic field, and the equipartition parameter $\eta = u_e^{'}/u_B^{'}$ is directly proportional to the flux state. The observed SED peaks also shift with activity, both the peaks move towards lower energies when source is in a low state and move to higher energies when source is in a high state. Spectral hardening is also commonly indicated in TeV blazars at the time of high state or a flare. This may be due to particle acceleration at the shock. The SSC modeling discussed in this work indicate that the energy spectrum of freshly accelerated electrons within the blazar emission zone of Mrk 421 and Mrk 501 can give rise to electron energy distribution of index $\sim$2.2. The acceleration of the electrons are possible at the shock fronts in the jets.

Mrk 501 is the first source which displayed minute scale time variability at TeV energies. These variability time-scales are much shorter than inferred light-crossing times at the black hole horizon and challenge the present understanding of the variability explained by light crossing argument. Several explanations were suggested such as misaligned minijets inside the main jet [137], jet deceleration [138, 139] to wiggles in an anisotropic electron beam directed along the jet [140] or high Lorentz factor [136].

We have suggested that a mild pressure anisotropy in electron distribution can give rise to a nonresonant, fluid instability called the firehose instability, which can result in a disruption of the large-scale jet over timescales of a few minutes. The disruption of the large-scale jet features due to the firehose instability provides a natural explanation for the observed variability at TeV energies [166].

6.1.2 HAGAR telescope

Details of HAGAR facility at IAO, Hanle at an altitude of 4300 m are also presented in this thesis. A detailed description of the telescope, it's design, back-end electronics and detector electronics are also presented. In addition to the telescope system, data analysis technique to detect point sources and the basics of atmospheric Cherenkov technique are described here.

One of the primary goals of HAGAR was to achieve lower energy threshold by setting up a moderate size telescope array at a higher altitude. A reduction in the energy threshold and improved sensitivity over PACT located at Pachmarhi at an altitude of 1100 m has been achieved by exploiting the higher Cherenkov photon density available at Hanle's altitude. The energy threshold for HAGAR is 200 GeV compared to PACT, for which it is 800 GeV. HAGAR can detect Crab like source with a 5 σ significance in $\sim$ 17 hours, while PACT takes $\sim$ 48 hours for similar detection.

6.2 Future plans

6.2.1 TeV blazars studies

Substantial progress in our understanding of TeV blazars has been made in the recent years. However, we are still very far from a complete understanding of these sources. The dominant emission mechanism, content of the jets, role of external photon field in γ-ray production in jets are still not clear. The basic question about the role of magnetic fields in the origin, confinement and propagation of relativistic jets is also open.

The study of temporal correlations between VHE γ-rays and other wavelengths will enable us to distinguish between the leptonic and hadronic models. High quality, simultaneous X-ray-TeV observations are needed on both short and long timescales

to establish firmly the nature of this correlation and the presence (or absence) of orphan flares (i.e., individual flares). The energy dependent variability carries the signature of the mechanism by which it is produced. The presence of a positive X-ray-TeV correlation is a prediction of SSC models. The study of time lags between X-ray and γ-ray emissions might impose constraints on emission region and it could also distinguish between SSC and External Compton (EC) models. The hardening or softening of the multiwaveband spectra along with flux variability will provide hints on the mechanism by which variability is caused and is a potential area for further investigation. It will be important for future studies to obtain larger quantities of simultaneous/nearly simultaneous multiwavelength data over varying timescales that will enable us to gain more insight into the nature of any correlations that may be present, and also the physical location, size and mechanism of the various emission zones causing the observed range in variability.

The flux variability can also shed light on motions of the bulk outflows of the plasma in the innermost region of jets which is well beyond the current imaging capabilities of telescopes in any part of the electromagnetic spectrum. Several blazars have recently displayed minute-timescale variability at TeV energies detected by MAGIC telescopes. This has resulted in a great deal of interest in the emission mechanisms responsible for these TeV flares. Suggestions range from a coherent instability in a compact emission region, misaligned minijets inside the main jet, jet deceleration, or the relativistic firehose instability as viable candidates for explaining this fast variability. The detection of such fast variability in future by MAGIC, VERITAS, and HESS telescopes will help us to discriminate between several proposed theoretical explanations. The detection of fast (minute scale) variability will also impose very tight constraints on the size of emission zone, magnetic field and Doppler factor of the jets.

The multiwaveband observations of blazars from radio to γ-rays from several ground based instruments such as OVRO, GMRT, VLA, SPOL, HCT, and space-borne instruments Swift-XRT, Astrosat (upcoming Indian X-ray and UV satellite) and Fermi-LAT along with HAGAR and MACE telescopes will lead us to investi-

gate the above stated properties of the blazar jets. The simultaneous broadband data sets resulting from the multiwavelength campaigns will offer an unprecedented opportunity to model the emission of TeV blazars in a more robust way than in the past and will place tighter constraints on the emission models and other physical parameters.

The injected particle spectrum can also be studied by modeling the synchrotron hump. The modeling of electron energy distribution will help to differentiate between the diffusive acceleration of the radiating electrons at relativistic shocks from the radiatively re-processed electron distribution of the initial (injected) Maxwellian distribution.

Several TeV blazars will be observed and monitored in the future using HAGAR telescope at TeV energies. Improved HAGAR sensitivity will allow us to explore much fainter sources, typically with flux less than 10% of that of Crab Nebula. One of the benchmark sources will be 1ES 2344 + 514, which is an established TeV blazar ($z = 0.044$), first detected by Whipple observatory in 1998 [167]. This source is found to be variable over long timescales [168, 169, 170].

1ES 2344+514 has been observed with the HAGAR telescope since 2008 and found to in a very low state. Due to the limited sensitivity of HAGAR, a statistically significant signal could not be detected. We computed a 3 σ upper limit on its flux above 250 GeV to be 47% of Crab. 1ES 2344+514 is one of the potential blazars which can be studied in detail using HAGAR in the near future, with an improved sensitivity.

TeV blazars Mrk 421 and Mrk 501 can be observed everynight to obtain a very dense light curve, which could be used for variability and correlation studies with multiwavelength data. Another possibility will be the detection of intra-hour scale variability during a flare using HAGAR with improved sensitivity.

The multi messenger astronomy along with high quality long term simultaneous multiwaveband data will be required to constrain the emission model of blazars. The detection of neutrinos from blazars or correlated variability of X-rays with γ-rays at

short as well as long term may provide much stronger constraints on the jet models.

6.2.2 Improvement of HAGAR sensitivity

The HAGAR telescope performance and sensitivity can be improved by up-gradation of hardware and improving the data analysis technique. The up-gradation of CAMAC-based DAQ system to VME based DAQ system, which can handle more number of channels, would improve HAGAR performance. The other improvement that can be made is by changing the PMT detectors to Geiger-mode avalanche photodiodes (GAPDs). The HAGAR telescope array's threshold can also be lowered by adding together the analog *Royal Sum* pulses of the individual telescopes to generate a *Grand Royal Sum* pulse.

The HAGAR sensitivity can be further enhanced by improving the analysis method by rejecting isotropic cosmic ray background. The γ-ray induced shower can be discriminated from cosmic ray induced showers by using a pulse shape profile which can be obtained from commercial waveform digitizers such as ACQIRIS. The other possible improvement is in reconstruction of arrival angle of each event, by fitting a spherical front to Cherenkov wavefront. This will improve estimation of the arrival angle of γ-rays showers so that we can reject off-axis events which are caused by isotropic background CRs events. Nearly 90% of the cosmic ray induced showers can be identified and rejected using both these methods, while only a few percent of γ-ray induced shower would be rejected. A rejection of 90% of the cosmic ray events and retention of 70% of γ-ray events will improve the HAGAR sensitivity by $\sim$5 times. If retention of 99% of γ-rays is achieved, then HAGAR sensitivity will reach close to 10 times the present sensitivity.

We can also apply a software padding technique to balance the night sky brightness of the On and Off regions. A spherical front fitting to Cherenkov wavefront will allow us to determine the core location of the shower and hence energy resolution of HAGAR will also be improved. A large area (21 m) imaging Cherenkov telescope MACE (Major Atmospheric Cherenkov Experiment) is being setup at Hanle,

in 2014. The use of MACE telescope to improve HAGAR sensitivity is another possibility. The common events between MACE and HAGAR can be identified above 200 GeV and background cosmic rays shall be rejected using MACE telescope by Hillas parameters.

HAGAR telescope will also be used to minimize the muon background for MACE telescope. At the lower energies meon events mimic γ-ray events and make their identification very difficult. As a muon event is a local phenomena, it will not trigger more than one telescope at a time and can not be detected by MACE and any of the HAGAR array telescopes simultaneously. Thus a non-detection in a HAGAR telescope neighboring the MACE telescope can be used to identify muon events.

The proposed Cherenkov Telescope Array (CTA) will be an array of many different size ACTs. CTA will be the next generation experiment which will provide much better angular resolution and sensitivity compared to that of present day ACTs. The realization of CTA will be a giant leap in the field of VHE γ-ray astronomy.

Bibliography

[1] M. Punch *et al.*, *Nature,* **358**, 477 (1992).

[2] H. Krawczynski, *New Astronomy,* **48**, 367 (2004).

[3] C. D. Dermer and R. Schlickeiser, *ApJ,* **416**, 458 (1993).

[4] G. Ghisellini and P. Madau, *Mon. Not. Roy. Astron. Soc.,* **280**, 67 (1996).

[5] F. A. Aharonian, *New Astronomy,* **5**, 377 (2000).

[6] A. Mücke, R. J. Protheroe, R. Engel, J. P. Rachen, and T. Stanev, Astroparticle Physics **18**, 593 (2003).

[7] A. A. Abdo *et al.*, *ApJ,* **736**, 131 (2011).

[8] H. Krawczynski *et al.*, *ApJ,* **601**, 151 (2004).

[9] S. M. Derdeyn, C. H. Ehrmann, C. E. Fichtel, D. A. Kniffen, and R. W. Ross, Nuclear Instruments and Methods **98**, 557 (1972).

[10] G. F. Bignami *et al.*, Space Science Instrumentation **1**, 245 (1975).

[11] C. E. Fichtel *et al.*, *ApJ,* **198**, 163 (1975).

[12] W. Hermsen, Royal Society of London Philosophical Transactions Series A **301**, 519 (1981).

[13] N. Gehrels, C. E. Fichtel, G. J. Fishman, J. D. Kurfess, and V. Schonfelder, Scientific American **269**, 68 (1993).

[14] R. C. Hartman *et al.*, VizieR Online Data Catalog **212**, 30079 (1999).

[15] http://fermi.gsfc.nasa.gov/ssc/.

[16] W. B. Atwood *et al.*, *ApJ,* **697**, 1071 (2009).

[17] M. Su, T. R. Slatyer, and D. P. Finkbeiner, *ApJ,* **724**, 1044 (2010).

[18] A. A. Abdo *et al.*, Science **325**, 840 (2009).

[19] P. L. Nolan *et al.*, *ApJ, Suppl.,* **199**, 31 (2012).

[20] T. C. Weekes *et al.*, *ApJ,* **342**, 379 (1989).

[21] www.tevcat.uchicago.edu/.

[22] http://www.physics.utah.edu/ whanlon/spectrum.html.

[23] F. A. Aharonian *et al.*, *Nature,* **432**, 75 (2004).

[24] E. Fermi, Physical Review **75**, 1169 (1949).

[25] Pierre Auger Collaboration *et al.*, Science **318**, 938 (2007).

[26] K. Greisen, Physical Review Letters **16**, 748 (1966).

[27] G. T. Zatsepin and V. A. Kuz'min, Soviet Journal of Experimental and Theoretical Physics Letters **4**, 78 (1966).

[28] http://apod.nasa.gov/apod/ap080217.html.

[29] F. A. Aharonian and S. V. Bogovalov, *New Astronomy,* **8**, 85 (2003).

[30] F. Aharonian *et al.*, *Astron. Astrophys.,* **370**, 112 (2001).

[31] C. M. Urry and P. Padovani, *Pub. Astron. Soc. Pac.,* **107**, 803 (1995).

[32] N. I. Shakura and R. A. Sunyaev, *Astron. Astrophys.,* **24**, 337 (1973).

[33] K. I. Kellermann, R. Sramek, M. Schmidt, D. B. Shaffer, and R. Green, *Astronom. J.,* **98**, 1195 (1989).

[34] U. B. de Almeida, Department of Physics, University of Durham, England October (2010).

[35] R. D. Blandford and R. L. Znajek, *Mon. Not. Roy. Astron. Soc.,* **179**, 433 (1977).

[36] R. D. Blandford and D. G. Payne, *Mon. Not. Roy. Astron. Soc.,* **199**, 883 (1982).

[37] L. Maraschi, G. Ghisellini, and A. Celotti, *Astrophys. J. Lett.,* **397**, L5 (1992).

[38] S. D. Bloom and A. P. Marscher, *ApJ,* **461**, 657 (1996).

[39] F. Tavecchio, L. Maraschi, and G. Ghisellini, *ApJ,* **509**, 608 (1998).

[40] P. B. Graff, M. Georganopoulos, E. S. Perlman, and D. Kazanas, *ApJ,* **689**, 68 (2008).

[41] C. D. Dermer, R. Schlickeiser, and A. Mastichiadis, *Astron. Astrophys.,* **256**, L27 (1992).

[42] M. Sikora, M. C. Begelman, and M. J. Rees, *ApJ,* **421**, 153 (1994).

[43] K. Mannheim, Science **279**, 684 (1998).

[44] M. Böttcher, A. Reimer, and A. P. Marscher, *ApJ,* **703**, 1168 (2009).

[45] K. Mannheim, *Astron. Astrophys.,* **269**, 67 (1993).

[46] R. J. Protheroe, High Energy Neutrinos from Blazars, in *IAU Colloq. 163: Accretion Phenomena and Related Outflows*, edited by D. T. Wickramasinghe, G. V. Bicknell, and L. Ferrario, volume 121 of *Astronomical Society of the Pacific Conference Series*, p. 585, 1997.

[47] W. Bednarek and R. J. Protheroe, *Mon. Not. Roy. Astron. Soc.,* **310**, 577 (1999).

[48] A. Atoyan and C. D. Dermer, Physical Review Letters **87**, 221102 (2001).

[49] A. Mücke and R. J. Protheroe, Astroparticle Physics **15**, 121 (2001).

[50] F. Boley, *Rev. Mod. Phys.,* (1964).

[51] W. Galbraith and J. V. Jelley, *Nature,* **171**, 349 (1953).

[52] H. W., Dover press, (1954).

[53] J. J. V, York : Pergamon (1958).

[54] J. J. D., John Wiley Sons, New York, (1975).

[55] http://www.gae.ucm.es/ emma/docs/tesina/node4.html.

[56] A. M. Hillas, *Space Sci. Rev.,* **75**, 17 (1996).

[57] D. J. Fegan, Journal of Physics G Nuclear Physics **23**, 1013 (1997).

[58] M. V. S. Rao and S. Sinha, Journal of Physics G Nuclear Physics **14**, 811 (1988).

[59] D. Bose, Department of High Energy Physics Tata Institute of Fundamental Research, Mumbai, (2006).

[60] O. S., University of Chicago, Unpublished (2000).

[61] V. R. Chitnis and P. N. Bhat, Astroparticle Physics **12**, 45 (1999).

[62] V. R. Chitnis and P. N. Bhat, Astroparticle Physics **15**, 29 (2001).

[63] V. R. Chitnis and P. N. Bhat, Bulletin of the Astronomical Society of India **30**, 345 (2002).

[64] R. A. Ong *et al.*, Astroparticle Physics **5**, 353 (1996).

[65] R. Cowsik, P. N. Bhat, V. R. Chitnis, B. S. Acharya, and P. R. Vishwanath, A possible High Altitude High Energy Gamma Ray Observatory in India, in *International Cosmic Ray Conference*, volume 7 of *International Cosmic Ray Conference*, p. 2769, 2001.

[66] K. S. Gothe *et al.*, Experimental Astronomy , 44 (2012).

[67] D. Heck, J. Knapp, J. N. Capdevielle, G. Schatz, and T. Thouw, *CORSIKA: a Monte Carlo code to simulate extensive air showers.* (, 1998).

[68] R. A. Ong, *Physics Reports,* **305**, 93 (1998).

[69] L. Saha *et al.*, Monte Carlo simulation for High Altitude Gamma Ray Telescope System at Ladakh in India, in *International Cosmic Ray Conference.*, pp. paper id:OG2.5,1129, 2011.

[70] L. Saha *et al.*, Astroparticle Physics , (2012).

[71] D. Bose *et al.*, *Astrophys. Spa. Sci.,* **309**, 111 (2007).

[72] B. B. Singh *et al.*, Astroparticle Physics **32**, 120 (2009).

[73] http://imagine.gsfc.nasa.gov/Images/glast/glast_lat_cutaway2.jpg.

[74] H. V. Bradt, R. E. Rothschild, and J. H. Swank, *Astron. Astrophys. Suppl.,* **97**, 355 (1993).

[75] V. R. Chitnis *et al.*, *ApJ,* **698**, 1207 (2009).

[76] http://swift.sonoma.edu/resources/multimedia/images/.

[77] D. N. Burrows *et al.*, *Space Sci. Rev.,* **120**, 165 (2005).

[78] P. S. Smith *et al.*, ArXiv e-prints (2009).

[79] J. L. Richards *et al.*, *ApJ, Suppl.,* **194**, 29 (2011).

[80] D. Petry *et al.*, *Astron. Astrophys.,* **311**, L13 (1996).

[81] J. A. Zweerink *et al.*, *Astrophys. J. Lett.,* **490**, L141 (1997).

[82] F. A. Aharonian *et al.*, *Astron. Astrophys.,* **350**, 757 (1999).

[83] K. K. Yadav *et al.*, Astroparticle Physics **27**, 447 (2007).

[84] J. Aleksić *et al.*, *Astron. Astrophys.,* **519**, A32 (2010).

[85] G. Di Sciascio and ARGO-YBJ Collaboration, **81**, 326 (2010).

[86] J. H. Buckley *et al.*, *Astrophys. J. Lett.,* **472**, L9 (1996).

[87] J. A. Gaidos *et al.*, *Nature,* **383**, 319 (1996).

[88] F. Krennrich *et al.*, *ApJ,* **511**, 149 (1999).

[89] T. Takahashi *et al.*, *Astrophys. J. Lett.,* **542**, L105 (2000).

[90] N. Bhatt *et al.*, Bulletin of the Astronomical Society of India **30**, 385 (2002).

[91] M. Błażejowski *et al.*, *ApJ,* **630**, 130 (2005).

[92] B. Giebels, G. Dubus, and B. Khélifi, *Astron. Astrophys.,* **462**, 29 (2007).

[93] J. Albert *et al.*, *ApJ,* **663**, 125 (2007).

[94] G. Fossati *et al.*, *ApJ,* **677**, 906 (2008).

[95] D. Horan *et al.*, *ApJ,* **695**, 596 (2009).

[96] S. Vernetto and Argo-Ybj Collaboration, Astrophysics and Space Sciences Transactions **7**, 65 (2011).

[97] J. Binks, APS Four Corners Section Meeting Abstracts , L1004 (2010).

[98] M. Tluczykont *et al.*, *Astron. Astrophys.,* **524**, A48 (2010).

[99] A. Shukla *et al.*, *Astron. Astrophys.,* **541**, A140 (2012).

[100] J. M. Dickey and F. J. Lockman, *Ann.Rev. Astron. Astrophys.,* **28**, 215 (1990).

[101] N. Isobe *et al.*, *Pub. Astron. Soc. Japan,* **62**, L55 (2010).

[102] R. A. Ong, The Astronomer's Telegram **2443**, 1 (2010).

[103] M. Tluczykont, ArXiv e-prints No.:1106.1035 (2011).

[104] G. Ghisellini *et al.*, *Astron. Astrophys.,* **327**, 61 (1997).

[105] C. Tanihata, J. Kataoka, T. Takahashi, and G. M. Madejski, *ApJ,* **601**, 759 (2004).

[106] T. Alexander, Is AGN Variability Correlated with Other AGN Properties? ZDCF Analysis of Small Samples of Sparse Light Curves, in *Astronomical Time Series*, edited by D. Maoz, A. Sternberg, & E. M. Leibowitz, volume 218 of *Astrophysics and Space Science Library*, p. 163, 1997.

[107] A. Franceschini, G. Rodighiero, and M. Vaccari, *Astron. Astrophys.,* **487**, 837 (2008).

[108] A. A. Abdo *et al.*, *ApJ,* **707**, 1310 (2009).

[109] A. A. Abdo *et al.*, *Astrophys. J. Lett.,* **733**, L26 (2011).

[110] J. Quinn *et al.*, *Astrophys. J. Lett.,* **456**, L83 (1996).

[111] M. Catanese *et al.*, *Astrophys. J. Lett.,* **487**, L143 (1997).

[112] E. Pian *et al.*, *Astrophys. J. Lett.,* **492**, L17 (1998).

[113] Y. Xue and W. Cui, *ApJ,* **622**, 160 (2005).

[114] J. Albert *et al.*, *ApJ,* **669**, 862 (2007).

[115] F. A. Aharonian *et al.*, *Astron. Astrophys.,* **342**, 69 (1999).

[116] F. Aharonian *et al.*, *Astron. Astrophys.,* **349**, 29 (1999).

[117] F. Aharonian *et al.*, *ApJ,* **546**, 898 (2001).

[118] A. C. Gupta, W. G. Deng, U. C. Joshi, J. M. Bai, and M. G. Lee, *New Astronomy,* **13**, 375 (2008).

[119] S. P. Gupta *et al.*, *New Astronomy,* **17**, 8 (2012).

[120] W. Cash, *ApJ,* **228**, 939 (1979).

[121] J. R. Mattox *et al.*, *ApJ,* **461**, 396 (1996).

[122] P. M. W. Kalberla *et al.*, *Astron. Astrophys.,* **440**, 775 (2005).

[123] P. W. A. Roming *et al.*, *Space Sci. Rev.,* **120**, 95 (2005).

[124] D. J. Schlegel, D. P. Finkbeiner, and M. Davis, *ApJ,* **500**, 525 (1998).

[125] M. Gliozzi *et al.*, *ApJ,* **646**, 61 (2006).

[126] A. A. Abdo *et al.*, *ApJ,* **727**, 129 (2011).

[127] A. Neronov, D. Semikoz, and A. M. Taylor, *Astron. Astrophys.,* **541**, A31 (2012).

[128] F. Aharonian *et al.*, *Astrophys. J. Lett.,* **664**, L71 (2007).

[129] M. T. Carini and H. R. Miller, *ApJ,* **385**, 146 (1992).

[130] C. S. Stalin *et al.*, *Mon. Not. Roy. Astron. Soc.,* **366**, 1337 (2006).

[131] A. C. Gupta, J. H. Fan, J. M. Bai, and S. J. Wagner, *Astronom. J.,* **135**, 1384 (2008).

[132] A. C. Gupta, D. P. K. Banerjee, N. M. Ashok, and U. C. Joshi, *Astron. Astrophys.,* **422**, 505 (2004).

[133] Gopal-Krishna *et al.*, *Mon. Not. Roy. Astron. Soc.,* **416**, 101 (2011).

[134] A. Goyal *et al.*, *Astron. Astrophys.,* **544**, A37 (2012).

[135] H. Anderhub *et al.*, *ApJ,* **705**, 1624 (2009).

[136] M. C. Begelman, A. C. Fabian, and M. J. Rees, *Mon. Not. Roy. Astron. Soc.,* **384**, L19 (2008).

[137] D. Giannios, D. A. Uzdensky, and M. C. Begelman, *Mon. Not. Roy. Astron. Soc.,* **402**, 1649 (2010).

[138] M. Georganopoulos and D. Kazanas, *Astrophys. J. Lett.,* **594**, L27 (2003).

[139] A. Levinson, *Astrophys. J. Lett.,* **671**, L29 (2007).

[140] G. Ghisellini, F. Tavecchio, G. Bodo, and A. Celotti, *Mon. Not. Roy. Astron. Soc.,* **393**, L16 (2009).

[141] V. Krishan and P. J. Wiita, *ApJ,* **423**, 172 (1994).

[142] A. R. Crusius-Waetzel and H. Lesch, *Astron. Astrophys.,* **338**, 399 (1998).

[143] J. G. Kirk and I. Mochol, *ApJ,* **729**, 104 (2011).

[144] P. A. Becker and M. Kafatos, *ApJ,* **453**, 83 (1995).

[145] D. G. Wentzel, *ApJ,* **152**, 987 (1968).

[146] D. B. Melrose, *Astrophys. Spa. Sci.,* **6**, 321 (1970).

[147] D. G. Wentzel, *ApJ,* **157**, 545 (1969).

[148] F. A. Aharonian, A. N. Timokhin, and A. V. Plyasheshnikov, *Astron. Astrophys.,* **384**, 834 (2002).

[149] S. G. Lucek and A. R. Bell, *Mon. Not. Roy. Astron. Soc.,* **314**, 65 (2000).

[150] J. A. Eilek, *ApJ,* **230**, 373 (1979).

[151] G. Paesold and A. O. Benz, *Astron. Astrophys.,* **351**, 741 (1999).

[152] N. A. Krall and A. W. Trivelpiece, *Principles of plasma physics* (, 1973).

[153] D. N. Baker, J. E. Borovsky, G. Benford, and J. A. Eilek, *ApJ,* **326**, 110 (1988).

[154] P. D. Noerdlinger and A. K.-M. Yui, *ApJ,* **157**, 1147 (1969).

[155] M. Giroletti *et al.*, *ApJ,* **600**, 127 (2004).

[156] B. G. Piner, N. Pant, and P. G. Edwards, *ApJ,* **678**, 64 (2008).

[157] C. M. Urry and P. Padovani, *ApJ,* **371**, 60 (1991).

[158] P. Subramanian, P. A. Becker, and D. Kazanas, *ApJ,* **523**, 203 (1999).

[159] R. M. Sambruna *et al.*, *ApJ,* **538**, 127 (2000).

[160] M. Villata and C. M. Raiteri, *Astron. Astrophys.,* **347**, 30 (1999).

[161] H. Krawczynski, P. S. Coppi, T. Maccarone, and F. A. Aharonian, *Astron. Astrophys.,* **353**, 97 (2000).

[162] F. Tavecchio *et al.*, *ApJ,* **554**, 725 (2001).

[163] G. Ghisellini, A. Celotti, and L. Costamante, *Astron. Astrophys.,* **386**, 833 (2002).

[164] K. Katarzyński, H. Sol, and A. Kus, *Astron. Astrophys.,* **367**, 809 (2001).

[165] V. A. Acciari *et al.*, *ApJ,* **729**, 2 (2011).

[166] P. Subramanian, A. Shukla, and P. A. Becker, *Mon. Not. Roy. Astron. Soc.,* **423**, 1707 (2012).

[167] M. Catanese *et al.*, *ApJ,* **501**, 616 (1998).

[168] J. Albert *et al.*, *ApJ,* **662**, 892 (2007).

[169] V. A. Acciari *et al.*, *ApJ,* **738**, 169 (2011).

[170] MAGIC Collaboration *et al.*, ArXiv e-prints (2012).